Heteronuclear Feshbach Resonances in Ultracold Mixtures of Ytterbium and Lithium

Alaina Green

A dissertation
submitted in partial fulfillment of the
requirements for the degree of

Doctor of Philosophy

University of Washington

2019

Reading Committee:

Subhadeep Gupta, Chair

Kai-Mei Fu

Boris Blinov

Program Authorized to Offer Degree:
Physics

University of Washington

Abstract

Heteronuclear Feshbach Resonances in Ultracold Mixtures of Ytterbium and Lithium

Alaina Green

Chair of the Supervisory Committee:
Professor Subhadeep Gupta
Physics

This thesis reports on experimental observation of heteronuclear Feshbach resonances between ultracold alkaline-earth-like Yb and alkali Li atoms, revealing methods for experimental control of heteronuclear scattering properties and strategies for coherent production of YbLi molecules. Optical Feshbach resonances are observed between ^{174}Yb and ^{6}Li through photoassociation (PA) spectroscopy. Two-photon PA spectroscopy of a series of the least-bound vibrational states in the YbLi electronic ground state provides an accurate description of the long-range interatomic potential and an accurate value of the s-wave scattering lengths between Yb and Li. A dark atom-molecule superposition state is created by optically dressing pairs of colliding atoms within an optically trapped bulk mixture and the feasibility of using such a state for coherent molecule production through stimulated Raman adiabatic passage is discussed. Magnetic Feshbach resonances (MFRs) between ^{173}Yb and ^{6}Li are observed. In the combination of closed-shell Yb and open-shell Li, MFRs are shown to stem from short-ranged hyperfine coupling between the unpaired Li electron spin and the ^{173}Yb nuclear spin, as demonstrated by analysis of Feshbach spectroscopy on ultracold mixtures in which both species are fully spin polarized. This work identifies two pathways for the coherent production of paramagnetic, polar molecules from a mixture of trapped Yb and Li: manipulation of either an optical or magnetic Feshbach resonance.

TABLE OF CONTENTS

LIST OF FIGURES

LIST OF TABLES

Table Number Page

ACKNOWLEDGMENTS

Six years is a long time to get used to the idea that you work in a *real* research lab. Yet somehow I never did. I never lost sight of how lucky I was to work in the Gupta Lab. For this amazing experience I will always be grateful to my advisor Deep. In innumerable ways, Deep's unflagging support has helped me make the best of the opportunity, always finding the time to provide insightful feedback and to dispense advice and encouragement. He sets an example not only of perspicacity but also of dedication, kindness and good humor.

I would also like to thank the other members of my supervisory committee for supporting my work: Anton Andreev, Boris Blinov, Kai-Mei Fu, Bob Holzworth and Arka Majumdar. I thank Boris in particular for serving on my reading committee and for his insightful career advice and friendly encouragement. Kai-Mei also took great pains to help improve my thesis while serving on my reading committee for which I am grateful. From Kai-Mei's example I have worked to develop a fundamental and important skill which I had not fully appreciated: doing what is important! It sounds easy but it is not and after graduation I will continue to ask myself how I would use my time if I were Kai-Mei.

I am also grateful for the opportunity to have worked with Svetlana Kotochigova, Eite Tiesinga, Ming Li and Hui Li, all of whom worked patiently to bring together our rather different perspectives.

Over the years I have come to think of my basement lab - with its half-dead panels of garish fluorescent lights, concrete floor and cacophonous orchestra of instruments - as a cozily appointed fortress from which I rule the world. Like any space so transformed from it's fundamentals, this feeling of being at home is built on memories: small triumphs and acute devastation; hard-fought campaigns and wild goose chases; good jokes and also puns.

Good or bad, all were made better by the people I shared them with.

Ricky Roy was a patient and insightful teacher who taught me everything about the lab and served as an inspiring role model. In later years I worked closely with Jun Hui See Toh who became an integral part of the lab through his ability to quickly synthesize information, dedication to getting things right and willingness to work hard. As unflappable as he is competent, I could not have imagined a better labmate. Xinxin Tang has brought an unprecedented cheerfulness to the lab and I am inspired by his curiosity about wide-ranging subjects. I have also benefited greatly from the eclectic insights of Yifei Bai.

I am grateful for two postdocs who I have had the privilege to work with in the lab: Ryan Bowler and Katie McCormick. From Ryan I learned several valuable technical skills and received much needed encouragement when I felt like I was flailing. In the short time I have known Katie McC I have marveled at her extreme competence and acumen.

Although the time I actually worked with them was very short, I am grateful to Anders Hansen, Alex Khramov, Alan Jamison, and Will Dowd, who as the first graduate students in the lab set a congenial tone and a high bar.

Working next door in the interferometry lab, Ben Plotkin-Swing, Katie McAlpine, and Dan Gochnauer were a reliable resource of information and advice. With the recent addition of Tahiyat Rahman and Anna Wirth, the combined Gupta group has become a more vibrant community. Combined with the Blinovians working even farther down the hall, I have found joy putting our heads together to decipher the more inscrutable bits of the interesting articles we read for journal club.

I want to thank all the members of PIE who attended socials, book clubs and lunch meetings. For me these interludes were a powerful antidote against self-reproach that can haunt us all in stressed isolation.

I would like to thank many dear friends without whom I would never have made it to the point of writing a thesis. My life in graduate school was made immeasurably better by a group of awesome housemates who were also among my closest friends: Rachel Osofsky, Tong Wan and Sarah Carter. I am so grateful to Alex Ditter for chill times with culinary experiments and jigsaw puzzles that I will even forgive him for consistently losing critical edge pieces. I thank Katie Brennan and Ali Ashtari Esfahani for enlightening lunch engagements that always brightened my day. On Stephen French and Tyson Price I could always rely for wide-ranging and many-stranded conversations that could end only when we had broken out the Mathematica model or lit something on fire. I thank Gary and Laurie Ness for helping a recent college graduate start a new life in a new city. It has been my honor to call Katie McAlpine a labmate, a gym partner and a friend. Being the most insightful person I know, I have benefited greatly from having her in many parts of my life.

Getting my PhD was an exciting adventure I never would have started without support from the faculty at Lewis & Clark College. First among them is the late Shannon O'Leary, unicorn warrior physicist. Under Shannon's guidance I found both the fun in physics research and the belief that I could do it. In the years that I was so lucky to have known her, she taught me the value of taking every opportunity to succeed while making every opportunity to help others do the same. In this same tradition I have found invaluable support and mentorship from Anne Bentley. I would also like to thank Aojie Zheng for being an unwavering partner to my many infamous lab crimes.

Lastly I thank my family. First, I want to express my gratitude to both my parents and grandparents for humanely raising me as a 100% free-range child. I consider my pursuit of physics to be a mere extension of my childhood whiled away in exploration and discovery, full of love and care but light on structure and rigidity. The well-beyond-perturbative forces of my three brothers have made me scrappier and more determined. I thank them all for making me the person I am today.

Chapter 1

INTRODUCTION

Quantum gases are deceptively simple systems. Absent the confusing tumult of temperature, particles in quantum gases dramatically manifest their indistinguishability and are governed by quantum statistics. In ultracold quantum gases, we can “see” the inherent quantumness of the particles using well-developed tools of atomic physics, not only to access observables, but also to change the particles’ energy landscape. Indeed it was clever manipulation of atomic properties with lasers that enabled the first creation of a gaseous Bose-Einstein condensate (BEC) in 1995, followed a few years later by the first degenerate Fermi gas of atoms.

Since first leveraging the precise control afforded by lasers to engineer an entirely new phase of matter in the form of BEC, ultracold-atoms researchers have continued to expand the range of this control by cooling and trapping an increasingly diverse set of atoms and molecules, each with unique properties such as electronic transitions or different interactions. In turn, these properties can make certain species of ultracold atoms or molecules a powerful tool for studies of specific aspects of quantum simulation, precision measurement or quantum information processing.

That the cooling and trapping of a large set of atomic and molecular species would be integral to the rapidly expanding field of quantum gases was recognized at its foundation. In 1998, when the population of quantum degenerate atomic species numbered only three, the creators of the first BEC boldly proclaimed that “the number of different atomic and molecular species that could eventually be cooled to the BEC transition may be in the hundreds” [1]. Two decades later, we are still trying to prove them right. While the number of ultracold species at or near degeneracy has indeed increased, the interest in further diversity has persisted. This thesis aims particularly at the frontier of ultracold paramagnetic, polar molecules by investigating the possibility of synthesizing YbLi from an ultracold atomic mixture by manipulating scattering resonances.

This thesis contains four principal chapters. Chapter 2 describes the broader scientific benefit of studying neutral ultracold molecules, discussing both proposed impacts and active research projects. This chapter also discusses the particular properties of Yb and Li which are important not only to understand the peculiar challenges to making YbLi molecules, but also to outline its particularly interesting qualities. In Chapter 3, we present experimental results on spectroscopy of the YbLi molecule in one of the lowest excited electronic states and the sole electronic ground state. These results constitute the first study of Feshbach resonances in YbLi - the optical Feshbach resonance (OFR). More practically, these spectroscopies made possible the work in subsequent chapters that investigate in more detail coherent control of these scattering resonances for the purposes of molecule formation. In Chapter 4, we discuss the molecular states probed in the previous chapter in the context of coherent addressing of a three-level system. Such addressing may allow for efficient transfer of the atomic mixture into a molecular state even under the condition that the coupling between states is not the fastest timescale in the system. As our first efforts to create molecules in this way failed, we present our experimental analysis of the timescales involved, and through numerical modeling confirm that we are limited by two different oft-ignored mechanisms of decoherence, noting the ways in which the relevant timescales would change if these attempts are repeated with the atomic mixture in a deep optical lattice. Chapter 5 reports on a different and more widely studied type of Feshbach resonance - magnetic Feshbach resonances which rely on control of the spin degree(s) of freedom rather than the orbital degree of freedom. Because magnetic Feshbach resonances were long thought not to exist between YbLi, this chapter begins with an explanation of the origin of MFRs both in a more typical system and in a system such as YbLi. The latter parts of this chapter concern the experimental techniques used and first observation of such resonances in the mixture of ground state Yb and Li. The thesis closes with a discussion of the required steps to synthesize molecules in Chapter 6.

Here we discuss the feasibility of using our experimental control of the external magnetic field to convert atomic mixtures into molecules, exploiting the existence of the MFR and sketch the technical upgrades necessary to do so. Finally, we outline an exciting experiment to immediately pursue upon the successful creation of YbLi molecules.

Chapter 2

ULTRACOLD MOLECULES: WHY YOU WANT THEM AND HOW TO MAKE THEM

This chapter discusses the motivation behind this thesis. A general description of the broader scientific goals of the study of ultracold molecules is presented first. Then we discuss the current capabilities of researchers studying ultracold molecules which follow two distinct and complementary strategies. Before introducing the properties of the YbLi molecule that make it uniquely interesting among the cast of ultracold molecules, we briefly describe the properties of the Yb and Li atoms. This serves not only to explain the properties of the YbLi molecule but also to provide relevant background information to experimental techniques presented later in the thesis. Finally, a brief and somewhat generalized description of the experimental apparatus used in this work is presented for the uninitiated.

2.1 Motivation: Cool Science with Ultracold Molecules

The study of ultracold molecules is largely motivated by the same scientific promise as ultracold atoms which constitute a well-isolated, easily probed quantum system to which various interesting complications can be added such as tailored potentials and controlled interactions. The defining difference between atoms and molecules is the diversity of quantum states in which they can be prepared. While ultracold molecules are also characterized by electronic and nuclear spin states, they are further distinguished by the quantized motion of the nuclei relative to each other in the form of vibration and rotation. The additional degrees of freedom available in molecules makes their study an interdisciplinary field requiring collaboration, not only between different subfields of physics, but also between physicists and chemists. In what follows, we sketch four categories of research enabled by the study of ultracold molecules: quantum chemistry, quantum simulation, quantum information and precision measurement.

2.1.1 Quantum Chemistry

Trapped ultracold molecules allow for a bottom-up approach to quantum chemistry in which the participating reactants can be prepared in a single quantum state with their spins and dipole moments well-defined by the confinement of the trap [2]. By preparing samples of ultracold molecules and/or atoms in a single quantum state, the number of possible product states is limited, confining the reaction to a few or even just one pathway [3, 4]. This extraordinary simplification teases the possibility of fully understanding the transformation from reactants to products in a level of detail that cannot be accomplished even in cold molecular beams.

Fully-state controlled chemical reactants were first studied in samples of optically trapped KRb molecules at around 100 nK when unexpected losses from the ultracold sample were attributed to the bimolecular reaction $\mathrm{KRb}+\mathrm{KRb}\to\mathrm{K_2}+\mathrm{Rb_2}$ [5]. In this work, researchers used control over the molecule's hyperfine state to "turn down" the rate of chemical reactions by preparing a spin-polarized fermionic sample in which intermolecular collisions are suppressed by the necessity of tunneling through the angular momentum barrier.

While the ability to precisely prepare the state of an ultracold molecular sample gives a degree of control to the experimenters, a complete understanding of the chemical reaction would require the ability to probe and/or control also the product states as well as the intermediate complexes made up of all the involved atoms that form during the reaction. More recently, researchers have developed methods to probe the products and the four-body intermediate complex in the same $\mathrm{KRb}+\mathrm{KRb}\to\mathrm{K_2}+\mathrm{Rb_2}$ reaction [6]. The technique which relies on ionization of the particles participating in the reaction is itself dependent on the ability to precisely prepare the reactants in their lowest energy ro-vibrational state for which the reaction proceeds slowly enough to be probed.

Other proposals for studying the products of a chemical reaction involve trapping them.

This situation doesn't arise "naturally" as the energy released in most exothermic chemical reactions greatly exceeds the depths of the traps that are designed to capture laser-cooled atoms. However, in [7, 8] the authors proposed to observe reactions involving ultracold dimers that release a smaller than typical amount of energy in their reaction: 'isotope exchange reactions' in which two dimers containing different isotopes of the same element react to form two dimers each containing only one isotope. Further, the authors of [7, 8] have proposed that the amount of energy released could be tuned over a wide range using laser fields. Still others prospose to study the process of chemical reaction, not by capturing the products, but through probes of the short-lived intermediate states with external field control being used to detect resonant behavior, and therefore learn about the complex's spin structure [9, 10].

As of this writing, studies of fully-state controlled chemistry have been limited to a small number of ultracold heteronuclear dimers. Despite their small number, the study of these ultracold heteronuclear dimers continue to produce surprising results such as the rapid collisional loss of *chemically stable* ultracold molecules [11, 4, 12]. The cause of this rapid loss is currently the focus of much debate [13, 14, 15] and calls for further study of ultracold molecules with a variety of different properties. While the collisions of ultracold molecules is of integral importance to the study of quantum chemistry, it is also imperative that they be understood and perhaps prevented, as the production of a stable molecular sample is a precondition for a wide variety of proposed studies, discussed in the following subsections.

2.1.2 Quantum Simulation

Ultracold molecules are sought not only for their internal properties but also for their distinct interactions. Owing to the uneven distribution of the electron density around the various nuclei, most molecules have a permanent electric dipole moment in the ground state. The dipole-dipole interactions between two particles with dipole moments $\vec{p_1}$ and $\vec{p_2}$ take the following form.

$$V_{d-d} = \frac{1}{4\pi\epsilon}\frac{\vec{p_1}\cdot\vec{p_2} - 3\left(\vec{p_1}\cdot\hat{r}\right)\left(\vec{p_2}\cdot\hat{r}\right)}{r^3}$$

where ϵ is the permittivity, $\hat{r}$ is the interparticle separation unit vector and r is the interparticle separation magnitude. This interaction, which is characteristic not only of polar molecules but also of highly magnetic atoms [16, 17] and Rydberg atoms [18], are distinguished from more typical atom-atom interactions in two distinct ways.

First, since $V_{d-d} \propto r^{-3}$, it is longer range than van der Waals interactions which are typically the longest range interaction between neutral ground state particles and are given by $V_{\text{vdw}} \propto r^{-6}$. Intuitively, this means that each particle will"see" more of the other particles in the sample. More specifically, the r^{-3} dependence of the dipole-dipole interaction potential makes the scattering properties between two such particles distinctly different from that of the r^{-6} potential by overcoming the effects of the angular momentum barrier as will be briefly discussed in Chapter 5 [19].

Second, the dipole-dipole interaction is distinguished from van der Waals interactions in that it is anisotropic, with an angular dependence from the relative orientation of $\vec{p_1}$ and $\vec{p_2}$. This further complicates the rules of inter-particle scattering by allowing for coupling between different scattering partial waves as will also be briefly mentioned in Chapter 5 [19].

Combined with the ability to precisely probe and control the quantum state of ultracold atoms/molecules, the above properties are proposed as the basis for quantum simulation of quantum magnetism [20], novel types of superfluidity [21, 22] or the observation of topological phases [23]. As we shall see in the next section, these properties also provide the foundation for proposed quantum information processing with ultracold molecules.

2.1.3 Quantum Information

Ultracold molecules feature multiple properties that are crucial for a quantum information platform: seconds-long coherence times and strong long-range interactions for fast gates [24, 25, 26]. In contrast to ions, the interactions native to such molecules can be generally "turned off" by transferring the molecule to the ground rotational state where the expectation value of the dipole moment is zero [27, 28]. The ability to turn these interactions off at will can decouple them from environmental noise. This feature, combined with their seconds long trap and radiative lifetimes make ultracold molecules a particularly promising candidate to serve as storage qubits in a hybrid quantum information platform [29, 30].

Ultracold molecules also offer a high degree of scalability; with current capabilities one can easily imagine trapping and preparing in a target quantum state $\sim 10^4$ or more ultracold dimers in an optical lattice, with individual addressing available, either through field gradients or precisely aligned, narrow-focus laser beams [24, 27]. In such endeavors, ultracold-molecule trappers could greatly reduce motional decoherence effects by duplicating strategies for complete motional control in optical tweezers developed in atoms [31, 32, 33].

Since the first proposal for using polar molecules for quantum information [24], several proposals have considered in more detail the energy structure of particular molecules and the experimental simplifications they enable [25, 34, 35]. In light of these proposals, the seemingly infinite diversity of molecular species, combined with rapid expansion of our ability to cool and trap them, motivates further investigation of specific ultracold molecule candidates for quantum information.

2.1.4 Precision Measurement

Ultracold molecules are well-suited to extend our understanding of fundamental physics through tabletop spectroscopy experiments, much like spectroscopic measurements of atoms and molecules have done in the past [36]. Already, cold molecules (~ 1 K) have been used to put increasingly tight limits on CP violation, significantly constraining certain theories beyond the standard model through measurements of the electron electric dipole moment in paramagnetic ThO [37].

While the low temperatures and state preparation control are a general advantage of precision measurement with ultracold particles, a particular advantage of molecules lies in their myriad internal states which are not only greater in number but are also of different "types."

The interleaving of rotational and hyperfine spectra, for example, sets up the possibility that two states of different character (e.g. opposite parity) happen to be nearly degenerate [38]. Probes of such energy separations have been proposed for sensitive tests of temporal variations of unitless physical constants such as the electron-to-proton mass ratio [39, 40, 41]. With implications for proposed theories for unification of the four fundamental forces [38], these measurements are being actively pursued in the KRb molecule, and although the results are not yet competitive with previous measurements made using atomic clocks, rapid improvement seems likely [42].

Additional proposals for probes of fundamental physics through precision spectroscopy of molecules include time variation of the fine structure constant α [43], detection of non-Newtonian gravity [44], and measurements of nuclear-spin-dependent parity violation to better constrain electroweak coupling parameters [45, 46].

2.2 Two Methods for Producing Ultracold Molecules

The creation of ultracold molecules is typically accomplished using two different strategies, both of which are pursued with seemingly equal intensity as each has its own advantages. Below, we describe the general methods used and progress made with both strategies.

2.2.1 Direct Cooling

The direct cooling method is most analogous to the means of preparing ultracold atoms but has some key differences. The generation of ultracold *atomic* gases almost always begins with a hot atomic vapor that is slowed and cooled through precisely controlled spontaneous emission of photons [47]. Because the momentum imparted by a photon onto an atom is small compared to the momentum associated with its temperature, the atom must scatter photons repeatedly, meaning that the atom must spontaneously decay to the same state from which it was originally excited. The existence of such 'closed cooling cycles' is what generally limits the diversity in the population of ultracold atomic gases. In contrast to atoms however, the much larger number of internal states characterizing molecules typically precludes their having a closed cooling cycle. Nevertheless, there exist a subset of molecules for which these closed cycles can be approximately realized through the use of just a few repumping laser beams that plug the leaks in the cycle [48, 49].

Through judicious choice of molecular species, several groups have adapted the technique of laser cooling to form magneto-optic traps (MOT) of ultracold molecules and subsequently loaded the cooled samples into conservative traps including quadrupole magnetic traps and optical tweezers [50, 51, 32] and as of this writing, there are multiple other molecular species being experimentally investigated for application of these strategies [52, 53, 54, 55, 56, 57, 58, 59]. By combining the traditional method of MOT cooling and trapping with pre-cooling and slowing stages [60, 61, 62, 49], these groups have rapidly demonstrated the ability to recreate temperatures similar to a typical first stage cooling process for atoms, reaching $\sim 10\,\mu$K with sub-Doppler laser cooling techniques. However, the relatively low particle density of these molecular samples means that the maximum phase space densities achieved $\sim 10^{-8}$ [63] remain a few orders of magnitude lower than a typical laser cooling stage for atoms, posing a significant challenge to the creation of quantum degenerate samples.

Having made huge strides in the development of laser cooling techniques, the next challenge for direct cooling of molecules will be to develop or adapt existing techniques for cooling in conservative potentials as is necessary to approach quantum degeneracy. Following a laser cooling stage, atomic coolers will perform a variety of different techniques to further increase the phase-space density of their gases including: evaporative cooling [64, 65], sympathetic cooling [66] and degenerate Raman sideband cooling (dRSC) [67]. While evaporative cooling of molecules has been demonstrated in one case [58] it is thought to be hampered both by the high rate of inelastic collisions expected for molecules and also the relatively low starting phase space densities. Sympathetic cooling is also expected to suffer from the high rate of inelastic collisions although it has been demonstrated in ro-vibrational ground state molecules [68] and theoretical work hints at its feasibility in cases where spin-changing collisions can be suppressed [69, 70]. However, the recently accomplished feat of capturing laser-cooled molecules in optical traps holds promise for application of dRSC to molecular samples [63, 32].

2.2.2 Indirect Cooling

An alternate method to producing large samples of ultracold molecules is to form them from ultracold atoms which are already trapped, a method sometimes referred to as the “indirect approach”. If the process of converting atoms to molecules is coherent, the sample will have nearly the same phase-space density as the atomic mixture from which it was created [71]. Although this strategy has only been used to create a limited selection of dimers, it remains the best strategy for attaining very high phase space densities and has even been used to create the first quantum degenerate gas of molecules [72].

This process is usually accomplished through a process known as magneto-association: an adiabatic sweep across an avoided crossing between an atomic scattering state and a bound molecular state [71]. While this process results in molecules that remain translationally ultracold and in a single ro-vibrational state, they are usually prepared by necessity in the highest energy vibrational state of the molecule. In this state they are not only less scientifically interesting than molecules in the ro-vibrational ground state, but are also difficult to hold onto as they are collisionally unstable. For this reason, the magneto-association will typically be followed by one or more coherent processes that transfers the molecules to the ro-vibrational ground state, such as Stimulated Raman Adiabatic Passage (StiRAP) in which a two-photon laser field is used to dynamically manipulate a coherent superposition of the initial and final molecular states via a third electronically excited state [73].

Many research groups have used the coherent association+StiRAP technique to form ultracold molecules in their ro-vibrational ground state [74, 75, 76, 11, 77, 78, 79]. At the time of this writing there were several additional groups actively working to develop coherent association techniques in novel systems [80, 81, 82, 83, 84, 85]. As will be explained in Chapter 5, the roster of ultracold dimers made via this indirect approach is made up almost entirely of molecules containing two alkali atoms, owing to two general facts: there are widespread, easily implemented methods for cooling alkali atoms and pairs of alkali atoms often exhibit broad magnetic Feshbach resonances which are necessary for the magneto-association process. The notable exception is Sr_2 which is a bi-alkaline earth molecule [80]. In this case, molecules are formed from pairs of atoms using only laser fields in a StiRAP process that addresses not a superposition of two molecular states but rather a superposition of one free atom scattering state and one molecular state. As we shall see in Chapter 4, the replication of this technique in our group is of great experimental interest.

2.3 Properties of Yb

Before discussing the properties of the YbLi molecule which motivate our effort to make these ultracold molecules, it is instructive to consider the properties of its constituent atoms. This discussion will also include details important to the experimental methods throughout this thesis.

Yb (element 70) is a lanthanide atom with electronic structure similar to the alkaline-earth (group II) elements. In the context of ultracold atoms, Yb is generally attractive for several reasons.

- Yb has a $^1S_0$ (singlet) ground state which distinguishes it from the more typical $^2S_{1/2}$ (doublet) ground state characteristic of alkali atoms.
- Yb has multiple electronic transitions in the visible range with varying linewidths spanning several order of magnitude.
- Yb has several abundant isotopes, both bosonic and fermionic.

In one way or another, the work in this thesis is made possible because of these properties. We have used samples of ^{173}Yb and ^{174}Yb. Both isotopes have rather high natural abundance as seen in Table 2.1 [86]. The choice of these isotopes had several motivations. Critical to our experiments presented in Chapter 5, the fermionic isotope ^{173}Yb has a nonzero nuclear spin with a nuclear g-factor of -0.6776 [87]. Other experiments used in this thesis utilized

Mass	Nuclear Spin (I)	Nuclear g-Factor	Relative Abundance	Scattering Length
a.m.u.		μ_N		a_0
168	0 (boson)		0.0013	251.9
170	0 (boson)		0.0302	63.87
171	$1/2$ (fermion)	+0.4919	0.142	-2.83
172	0 (boson)		0.218	-599.0
173	$5/2$ (fermion)	-0.6776	0.161	199.4
174	0 (boson)		0.319	104.9
176	0 (boson)		0.129	-24.19

Table 2.1: Properties of Yb that vary by isotope: the mass, nuclear spin, nuclear g-factor, relative abundance and the intraspecies s-scattering length in units of the Bohr radius.

^{174}Yb for which integral processes, such as absorption imaging and evaporation, are slightly less complicated by the nuclear spin degree of freedom and fermionic statistics of ^{173}Yb. The choice of these two isotopes was also motivated by their collisional properties which were studied prior to this work in [88]. The s-wave scattering length is an important parameter for determining the efficiency of evaporative cooling and is presented in Table 2.1 for reference. The large, positive value of the scattering length for both ^{173}Yb and ^{174}Yb make them amenable to efficient evaporative cooling.

Figure 2.1 shows the low-lying energy levels of Yb along with the two electronic transitions used in this work [89, 90]. This structure is relevant not only to the preparation of ultracold Yb atoms, but also to several experiments in this thesis and will be referred to frequently in subsequent chapters and sections. Finally, because they are relevant to our work preparing the Yb nuclear spin state (Section 5.7) we present the g-factors for the relevant electronically excited states of ^{173}Yb in Table 2.2 [91].

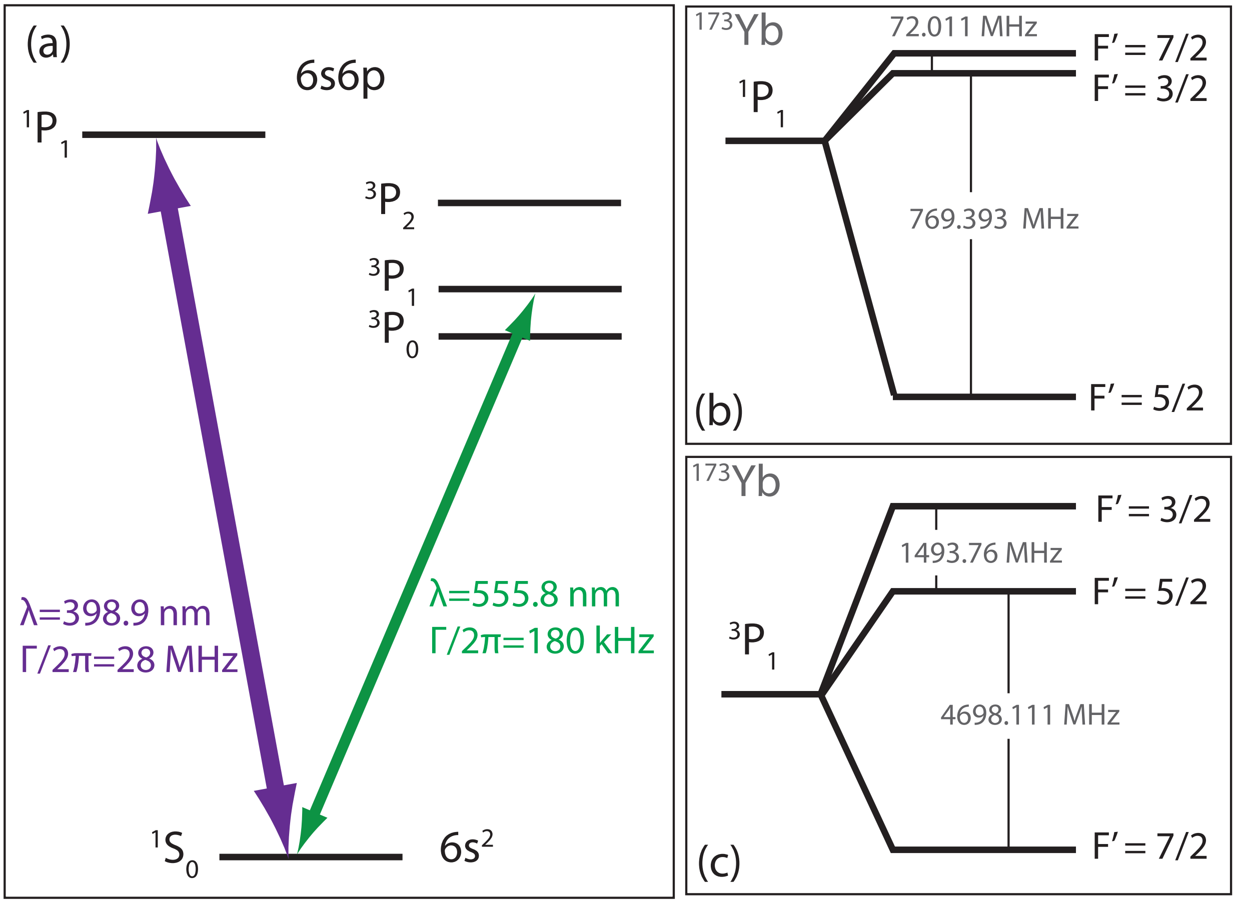

Figure 2.1: The relevant low-lying energy levels of Yb. (a) depicts the two electronic transitions used in this work. Note that the energy level separations are not to scale and hyperfine splitting is not shown. Isotope shifts are also irrelevant on this scale. ^{174}Yb has no hyperfine structure but for ^{173}Yb the hyperfine splitting is shown for two relevant energy levels in (b) and (c). Note that there is no hyperfine structure for ^{173}Yb in the $^1S_0$ ground state for which $F = {}^5\!/_2$.

F'	$^1\mathrm{P}_1$	$^3\mathrm{P}_1$
$3/2$	-0.400	-0.600
$5/2$	0.114	0.171
$7/2$	0.286	0.429

Table 2.2: The values of g_F for two excited electronic states of ^{173}Yb.

2.4 Properties of Li

Li is an alkali metal atom with a doublet $^2\mathrm{S}_{1/2}$ ground state. We exclusively trap ^{6}Li which is a popular choice in the ultracold atoms community as it is one of only two fermionic alkali isotopes. The low-lying energy levels of ^{6}Li are shown in Figure 2.2 along with the one strong electronic transition used in this work.

Li has hyperfine structure in all relevant electronic states owing to a nuclear spin of $I = 1$. For the purposes of this thesis, the hyperfine structure of the electronically excited $^2\mathrm{P}_{3/2}$ state is unimportant as the structure is not resolved by the $^2\mathrm{S}_{1/2} \rightarrow {}^2\mathrm{P}_{3/2}$ transition. However the hyperfine structure of the $^2\mathrm{S}_{1/2}$ ground state is important to much of the work in this thesis and warrants discussion if only to clarify the way these hyperfine states are labelled throughout the thesis.

2.4.1 Two Bases for the Li Electronic State

The nuclear spin of Li is coupled to the electronic spin through hyperfine coupling such that m_I is not generally a good quantum number. A consequence of this is that there are differing conventions used as shorthand for labelling the quantum state of Li.

Low Field Basis: In low field, the hyperfine coupling causes the angular momentum to be quantized according to the total angular momentum $F = I + J$. Since $I = 1$ for ^{6}Li and we are considering only the $^2S_{1/2}$ ground state, $F = 1/2, 3/2$. These states will split into their projections m_F as long as the hyperfine coupling remains strong compared to the coupling

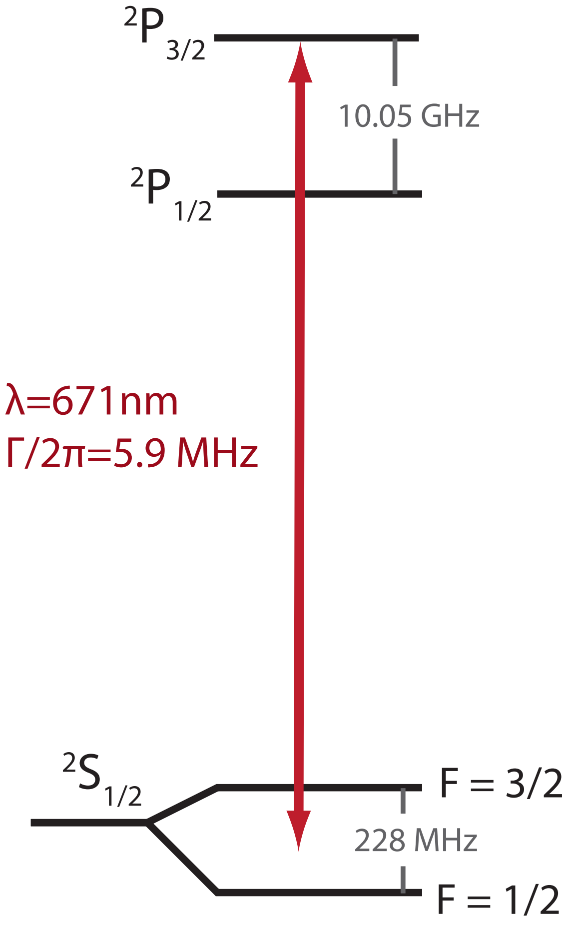

Figure 2.2: The low-lying energy levels of ^{6}Li with the strong electronic transition used in this work shown as a red arrow. Owing to the resolved fine structure splitting of the ^2P excited state, this electronic transition is historically referred to as the D-line, with D standing for doublet. The hyperfine structure in the ^2P states is unimportant for this work and is not shown.

of the individual spins to the external field, evolving as $E_{Zeeman} = g_F \mu_B m_F B$ where g_F is the hyperfine g-factor, μ_B is the Bohr magneton and B is the external field. As shown in Figure 2.3 the relatively small hyperfine coupling of Li and the strong coupling of the electronic spin to the external field means that the shift from the magnetic field deviates from this prescription even at ≈ 20 G.

High Field Basis: When the Zeeman coupling to the external field exceeds the hyperfine coupling between the electron and nuclear spins, the projections m_I and m_J become good quantum numbers, making the state $|IJm_Im_J\rangle$ a good approximation of the true eigenstate of the system.

The Common Convention: The connection between states $|IJFm_F\rangle$ in low field and $|IJm_Im_J\rangle$ in high field is generally well understood by researchers working with ground state Li atoms. For this reason, it is common to label the six hyperfine ground states simply as $|1\rangle$ through $|6\rangle$ in order of ascending energy at finite field (see Figure 2.3). In this thesis we will usually use the common convention. However, we will sometimes use $|IJFm_F\rangle$ even to refer to eigenstates at high field, assuming the correspondence between high and low field states is understood.

2.5 Motivation: Properties of YbLi

The primary interest in making ultracold YbLi molecules from Yb and Li stems from the atoms' different electronic properties. The combination of the $^2\mathrm{S}_{1/2}$ ground state of Li with the $^1\mathrm{S}_0$ ground state of Yb means that the molecule itself has an unpaired electron. In an analogy to the typical atomic term symbol, molecules of this type are given the label $^2\Sigma$. This doublet electronic structure distinguishes the YbLi molecule from the bi-alkali molecular species that make up the majority of the molecules created through direct cooling. With the sole exception of NaLi which is prepared in a triplet state ($^3\Sigma$), all the molecules formed near quantum degeneracy using the indirect method are in a spin-singlet state ($^1\Sigma$).

The ground state magnetic moment of YbLi affords an additional means with which to control them. In the most general sense, the YbLi molecule (and those like it such as CsYb

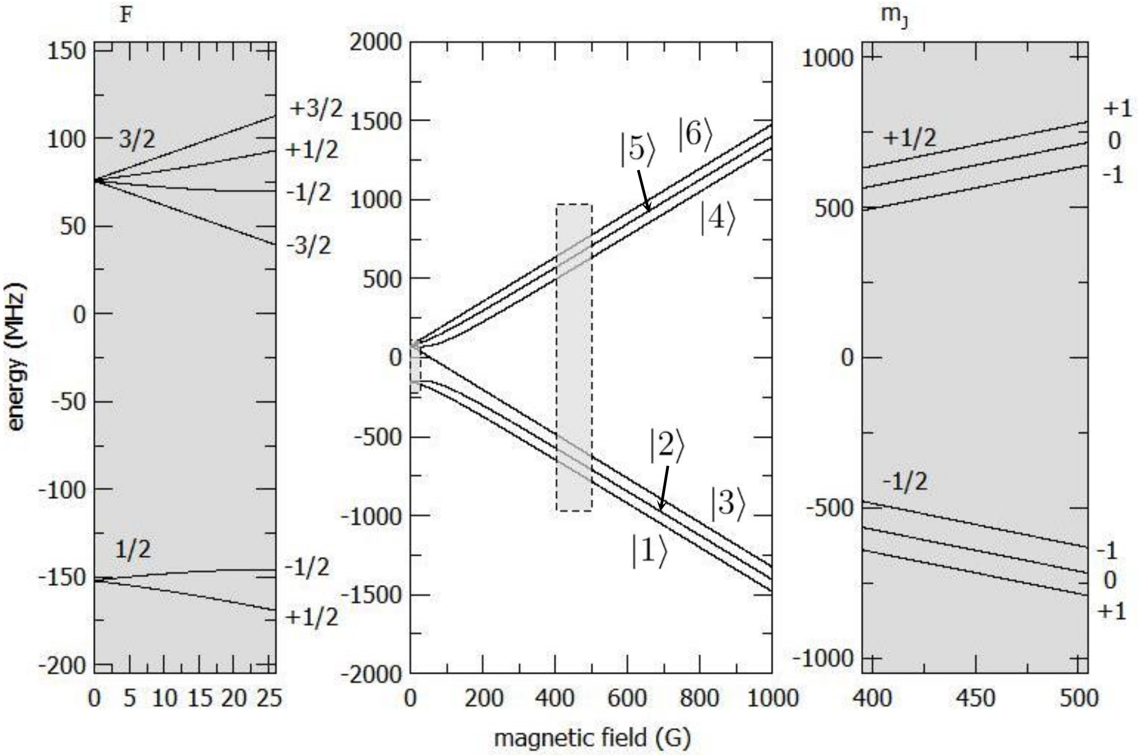

Figure 2.3: The magnetic field dependence of the 6 hyperfine ground states of ^{6}Li. Insets on the left and right correspond to the shaded regions in the middle plot. The states are labeled in three ways: with the low field quantum number F, m_F (left), the common shorthand (middle), and the high field quantum numbers m_J, m_I (right).

and RbSr) is the alkali atom of the molecule world and therefore ripe for examination by the same methods which have been developed and refined over multiple decades of research into ultracold alkalis. Most fundamentally, the YbLi molecule can be magnetically trapped. This could be of critical importance for the study of ultracold molecules as trapping molecules in optical traps may be associated with higher loss rates than for atoms [15]. As we shall see in Chapter 5, the ability to magnetically control interactions in ultracold atoms has been pivotal to studying them in the more general and highly diverse contexts of few- and many-body physics. Unlike the spin-singlet molecules, it's possible that magnetically tunable interactions exist between spin-doublet molecules.

The YbLi molecule, being a heteronuclear dimer also has a permanent electric dipole moment arising from the uneven distribution of the electrons around the two different nuclei. Ground state molecules with both an electric and magnetic dipole moment are the subject of wide-ranging theoretical discourse. Much of this interest hinges on coupling between the electron spin and the molecular rotation. With control over the rotational degree of freedom being the "switch" used to access long-range interactions between dipolar molecules, this spin-rotation coupling allows for controllable effective spin-spin interactions which are the essential ingredient for a variety of lattice spin models, central to condensed matter studies [92]. This coupling also allows for unique implementation of quantum information processing with ultracold molecules which is distinguished from other proposed schemes that typically require fine control over external electric fields in order to achieve individual qubit addressability [93]. Additionally, this coupling allows for the implementation of field-controlled chemical reactions [94].

Unfortunately, the magnitude of the YbLi ground state electric dipole moment is predicted to be too small for dipole-dipole interactions to be productively wielded in experiments as they are designed today [95], though it's possible that larger dipole moments could be coherently accessed by mixing the ground state with an excited state via a narrow electronic transition within the molecule [96].

2.6 An Overview of the Experimental Apparatus

The purpose of this section is to briefly explain the common elements and methods of ultracold atom experiments to a reader unfamiliar with these techniques, as an understanding of these will be assumed throughout. For specific details on our apparatus, the reader is referred to the theses of Anders Hansen [97] and Alex Khramov [98].

Vacuum System In the course of our experiments, ultracold atoms are held for several seconds in traps with a depth corresonding to a temperature $\sim 1\,\mu$K. Consequently, a collision between a trapped atom and an air molecule will necessarily cause loss from the trap and the lifetime of atoms in the trap will ultimately be limited by the pressure they are exposed to. For this reason, our experiments take place in a chamber under ultra-high vacuum. A typical pressure inside our main vacuum chamber where the atoms are trapped is $\sim 10^{-11}$ Torr. We measure typical trap lifetimes of about 4 seconds for Yb and longer than 20 seconds for Li.

Atomic Source Both Yb and Li are metallic solids at room temperature (even under vacuum) and must be heated to produce a vapor that can be laser cooled. Our apparatus includes two separate ovens - one for each element - which are heated to about 400 degrees Celsius. Each oven is connected to the main vacuum chamber by a long tube through which a beam of atomic vapor travels to the main chamber after being roughly collimated by a nozzle at the output of the oven. The RMS speed of the vapor is ~ 100 m/s, too fast to be captured in our traps. The vapor is slowed using the Zeeman slower approach which utilizes the radiation pressure from a resonant laser beam propagating in the opposite direction of the vapor [99]. As the atoms are slowed, the change in the Doppler shift significantly detunes the slowing laser beam from resonance. This shift is counteracted by a spatially varying magnetic field that cancels the Doppler shift using a Zeeman shift. In our apparatus the magnetic field is generated by electromagnets wound in a tapered solenoid configuration along the whole length of the slowing tube. By the time the vapor reaches the main vacuum chamber, the RMS speed is reduced to ~ 10 m/s.

Magneto-optic Trap The magneto-optic trap (MOT) performs the first stage of cooling in all dimensions and also traps the atoms [47]. Cooling in the magneto-optic trap is based on laser cooling through which the momentum of many photons is used to reduce the momentum of an atom. This process relies on repeated spontaneous emission of photons after electronic excitation. In order for the momentum of the atoms to be reduced, the laser beams must be near but at a slightly lower energy than the electronic transition within the atom such that an atom moving antiparallel to the laser beam propagation will scatter more strongly than one moving parallel to it owing to different Doppler shifts. These red-detuned beams are oriented along three orthogonal directions in counterpropagating pairs in order to cool in all directions. Under these conditions - known as optical molasses - cold atoms can still randomly walk out of the molasses because the restoring force in each direction is uncoupled to that of the other directions. To avoid loss from the molasses, a magnetic field gradient is used to impose a spatial dependence on the scattering rate of photons and each pair of counterpropagating beams is given opposite circular polarization beams such that selection rules effect an overall restoring force to the center of the trap. After the MOT has captured and cooled a large sample of atoms, we compress the MOT such that the sample can be more readily trapped by the optical dipole trap where they will undergo further cooling. This compression is done by simultaneously increasing the magnetic field gradient and reducing both the detuning and intensity of the MOT beams which has the total effect of reducing the temperature and increasing the density of the sample. By the end of the compressed MOT stage, the atoms are at $\sim 10-100\,\mu$K, cold enough to be trapped in our optical dipole trap and number $\sim 10^8$ and density $\sim 10^{11}\,\mathrm{cm}^{-3}$. For Li, the MOT beams are formed of light detuned from the ${}^2S_{1/2} \to {}^2P_{3/2}$ transition. Because hyperfine structure of ${}^2P_{3/2}$ is not resolved, atoms fall into both hyperfine ground states of ${}^2S_{1/2}$, which are resolved. For this reason, the Li MOT beams contains two frequencies known as the “MOT beam” (tuned to the $3/2$ ground state) and the “repumping beam” (tuned to the $1/2$ ground state). For Yb the ${}^1S_0 \to {}^3P_1$ transition is used.

Optical Dipole Trap Unlike the MOT, the optical dipole trap (ODT) is a conservative potential utilizing laser light that is far detuned from any strong electronic transitions of either Yb or Li: 1064 nm. As a collection of charges, atoms can be polarized in an AC electric field and depending on the sign of the polarizability can be attracted or repelled from areas of higher field. The use of light that is red detuned from strong electronic transitions will ensure that this force is attractive. Hence, a trap can be formed at the focus of such a red-detuned laser beam [91]. Important experimental detail on the use of such traps for cold atoms can be found in [100]. In practice, we are typically able to transfer from the MOTs $\sim 10^7$ Yb atoms and $\sim 10^5$ Li atoms into our ODT at densities $\sim 10^{14}\,\mathrm{cm}^{-3}$ and $\sim 10^{13}\,\mathrm{cm}^{-3}$ respectively. The second stage of cooling for Yb and Li occurs in the ODT through forced evaporative cooling [65]. By reducing the power of the trapping laser the trapping potential is lowered, releasing the hottest atoms from the trap. Subsequent rethermalization through elastic collisions means the final temperature is lower. By continuously dropping the depth of the trap, the temperature is reduced at the expense of the number of atoms trapped but with a net effect of increasing the phase-space density. In our case, this process preferentially spills out Yb owing to it's lower polarizability at 1064 nm. However, the process of reducing the trap depth also cools the Li atoms through interspecies elastic collisions, a method referred to as sympathetic cooling [66, 101]. Our group has used this method to achieve simultaneous quantum degeneracy of Yb and Li [102], although this is not a requirement for the work in this thesis. In addition to controlling the intensity of the ODT light, we also change the effective size of the ODT beam through rapid modulation of the beam's position. This process is termed 'painting' and details can be found in [103].

Absorption Imaging Atoms in the ODT scatter very few photons and thus cannot be seen. We utilize the most typical technique to probe the trapped atoms: absorption imaging. A resonant laser beam is collimated and impinges on the atoms. The preferential absorption of the imaging beam in areas of higher atomic density imprints a "shadow" on the laser beam. This shadow is collected and focused onto a CCD camera for processing which gives an average spatial distribution of the atoms in the trap. More commonly, we perform absorption imaging after the ODT light has been shut off and the atoms have expanded in the vacuum. By imaging atoms after this time-of-flight, we gain information on their momentum distribution in the trap.

Chapter 3

MOLECULAR POTENTIALS OF YBLI

This chapter concerns spectroscopic studies of YbLi. A description of the general properties of two-atom molecules - dimers - is presented first. Following this is a discussion of the theoretical and experimental methods for understanding the energy spectra of dimers. Then we discuss the experimental methods used and results obtained in our study of an electronically excited state and the electronic ground state of the YbLi molecules. Finally we revise the ^{174}Yb^{6}Li scattering length based on these measurements.

3.1 Anatomy of a Dimer

A large portion of the scientific interest in ultracold molecules is due to the fact that they have a richer internal structure than atoms. However, all the ultracold molecules formed through the indirect method are dimers: merely two atoms. Is a bound state of two atoms really all that different from one atom? In this first subsection, we will discuss the surprisingly complex landscape of dimer quantum states and the approximations required to understand them even on a rudimentary level.

We start by considering the Hamiltonian for a heteronuclear dimer with N electrons.

$$H = -\frac{\hbar^2}{2m}\sum_{i=1}^{N}\vec{\nabla}_i^{\,2} - \frac{\hbar^2}{2M_1}\vec{\nabla}_1^{\,2} - \frac{\hbar^2}{2M_2}\vec{\nabla}_2^{\,2} + V\left(\vec{r_i},\vec{R_1},\vec{R_2}\right) \tag{3.1}$$

$$V\left(\vec{r_i},\vec{R_1},\vec{R_2}\right) = \frac{e^2}{4\pi\epsilon_0}\left[\frac{Z_1Z_2}{\left|\vec{R_1}-\vec{R_2}\right|} - \sum_{i=1}^{N}\frac{Z_1}{\left|\vec{r_i}-\vec{R_1}\right|} - \sum_{i=1}^{N}\frac{Z_2}{\left|\vec{r_i}-\vec{R_2}\right|} + \sum_{i=1}^{N}\sum_{j=1}^{i}\frac{1}{\left|\vec{r_i}-\vec{r_j}\right|}\right] \tag{3.2}$$

where $\vec{r_i}$, $\vec{R_1}$ and $\vec{R_2}$ are the coordinates of the ith electron, the first nucleus and the second nucleus respectively and m, M_1, and M_2 are their respective masses. In the above, only electrostatic interactions have been considered as spin-spin interactions will only constitute perturbative corrections. Assuming relativistic effects are also small, we could utilize this Hamiltonian to attempt to solve the Schrödinger equation. However, even for the simplest case of one electron, it cannot be solved analytically. Nevertheless, it is possible to arrive at approximate solutions based on a physically justified assumption. To get a sense of these approximate solutions, we will consider the case with just one electron.

The pivotal assumption is that owing to their much lighter mass, the electrons can adjust to any motion of the nuclei instantaneously. In other words, the nuclear motion is adiabatic according to the electrons and so at any point in time there is a well defined electronic wavefunction that depends on the coordinates $\vec{R_1}$ and $\vec{R_2}$ but only as parameters. This wave function obeys the partial equation shown below, assuming the electronic energy is much larger than the kinetic energy of the nuclei [104].

$$\left[-\frac{\hbar^2}{2m}\vec{\nabla}^2 + V\left(\vec{r}, \vec{R_1}, \vec{R_2}\right)\right]\phi_n = E_n^0\phi_n \tag{3.3}$$

In the above, n is used to label the electronic state which as we will see in Section 3.5 can itself be challenging to define. We have designated the energy as E_n^0 to indicate that this is the zeroth order energy and we will add the effect of the kinetic energy of the nuclei perturbatively. The assumption that the electrons adiabatically follow the motion of the nuclei is known as the adiabatic approximation or Born-Oppenheimer equation and justifies the separation of the total wave function into the product below [104].

$$\Psi = \sum_m \chi_m\phi_m \tag{3.4}$$

where $\phi = \phi\left(\vec{r}, \vec{R_1}, \vec{R_2}\right)$ but $\chi\left(\vec{R_1}, \vec{R_2}\right)$ is only a function of $\vec{R_1}$ and $\vec{R_2}$ and can be considered the nuclear part of the total wavefunction. Note that we have chosen to consider only the simplest case of having one electron. Putting this form for Ψ into the Schrödinger equation using the full Hamiltonian that includes the kinetic term for the nuclei, we obtain the following [104].

$$\left(E_n^0 - \frac{\hbar^2}{2M_1}\vec{\nabla}_1^{\,2} - \frac{\hbar^2}{2M_2}\vec{\nabla}_2^{\,2}\right)\chi_n = E\chi_n \tag{3.5}$$

where E is the total energy of the molecule. It is important to stress that E_n^0 is *not* the total energy of the molecule but rather the contribution of the potential energy $V\left(\vec{r}, \vec{R}_1, \vec{R}_2\right)$ and the electronic kinetic energy both averaged over the rapid motion of the electrons. As we will see in the next section, this potential is not itself easy to understand but we have succeeded in decoupling the nuclear and electronic wavefunctions themselves, effectively reducing the problem of quantum mechanically understanding a dimer to the problem of understanding this potential. For this reason E_n^0 will throughout the remainder of this thesis be referred to as the Born-Oppenheimer potential or the interatomic potential and assigned the symbol $V(R)$. Despite this relabeling, the fact that there may be multiple different potentials indexed by n should not be overlooked.

The study of this potential will be discussed in the following section. For now we take this as a fact: the heteronuclear dimer's nuclei are approximately an anharmonic oscillator. As such the wavefunctions can be labeled according to the number of vibrational quanta. In a standard harmonic oscillator, states are labeled in order of increasing energy from the ground state. Because the spectroscopy of heteronuclear dimers in ultracold atoms is typically focused on high-lying states, we choose to count in negative quanta with the absolute value increasing as the binding energy increases. Thus, the highest-lying or least-bound vibrational state is called $v = -1$, as shown in Figure 3.1. In this way the vibrational number doesn't indicate the number of vibrational quanta unless the number of bound states supported by the potential is known, in which case it can be inferred through subtraction.

Thus far we have concerned ourselves with solving the radial Schrödinger equation for the nuclear part of the molecular wavefunction and have determined the basis for the molecule's vibrational states. However, the molecule can also rotate. Additionally, we have neglected the two nuclear spins. The existence of these degrees of freedom is noted here only for

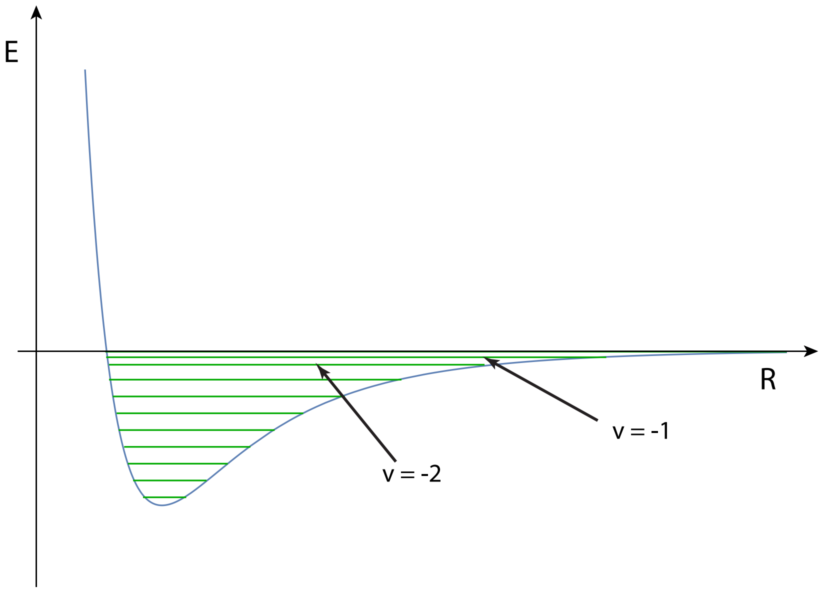

Figure 3.1: A schematic representation of the interatomic potential for a dimer plotted against the relative nuclear coordinate $R = \left|\vec{R}\right|$. The zero point for $V(R)$ is the energy of the free atom pair. The states are labelled counting downward from the level of dissociation using negative numbers.

completeness as the experimental work in this thesis is confined to the study of vibrational spectra in the YbLi molecule.

3.2 *Ab-initio* Analysis of Dimers

As mentioned in the previous section, the principal problem of understanding a dimer's quantum states lies in determining the interatomic potential. For dimers in particular, this problem is easier to visualize as the potential depends explicitly on only two nuclear coordinates $\vec{R_1}$ and $\vec{R_2}$. Therefore, what would ordinarily be a potential surface, is reduced to a function of one variable $R = \left|\vec{R_1} - \vec{R_2}\right|$. However, the potential still includes the interaction of many electrons with each other as well as with the nuclei making this an extremely complex problem under the purview of quantum chemistry.

Even as the field of quantum chemistry moves towards more refined methods to fully construct the molecular wavefunction from first principles, other approximation methods remain useful in the collaborations between quantum chemists and cold atom physicists. In particular, it has been fruitful to model the interatomic potential with the effective potential below.

$$V = V_{SR} + V_D \tag{3.6}$$

In the above, V_{SR} is the potential at short range that is dominated by Coulomb repulsion between the nuclei. At long range the potential is dominated by V_D, the dispersion potential arising from interactions between instantaneous dipoles (or other multipoles) formed within each constituent atom. V_D has the following form.

$$V_D = \sum_n \frac{C_n}{R^n} \tag{3.7}$$

As we shall see in later sections, understanding the C_n coefficients provides a powerful advantage for experimental probes in ultracold gases, where the least-bound molecules are most easily observed experimentally. For this purpose, *ab-initio* calculations on the YbLi system in particular have been used to determine the relevant values of C_n with impressive accuracy. This was made possible by advances in quantum chemical calculations that begin with the Hartree approximation of molecular orbitals whereby electron-electron interactions are considered on average to affect a shielding of the Coulombic potential of the nuclei but the electrons are otherwise independent. To this average shielding potential, electron correlations are incorporated nonperturbatively in "clusters" of 1 to N electron interactions. Calculations may then be performed up to some truncation of the series of clusters (usually 1 or 2). Sometimes, an additional term beyond the truncation is added perturbatively [105, 106].

Using these methods, quantum chemical calculations have been used to predict not only the relevant C_n values but various properties of the dimers that could be formed in various ultracold atoms laboratories working on molecule formation in atomic mixtures such as the permanent electric dipole moment for heteronuclear dimers. Multiple theoretical research groups have shown interest in the YbLi molecule in particular [107, 95, 108, 109].

While the collaboration between theoretical quantum chemists and experimental cold atom physicists has provided both high resolution spectroscopic data for benchmarking theoretical models for the chemists and some powerful predictive elements for the physicists, there are other important molecular properties that can only be determined with the required accuracy through spectroscopy. In particular, the difficulty of constructing the form of V_{SR} makes accurate *ab-initio* predictions of the vibrational spectra impossible. For this reason, experimental efforts to create ultracold molecules by forming a coherent connection between free atoms and a known molecular bound state will begin with some form of spectroscopy into the foreseeable future.

3.3 Methods of Probing Molecular Potentials

With their electronic, vibrational and rotational states, molecules have a daunting number of internal states, separated by energies that combinatorially span huge swathes of the electromagnetic spectrum. For this reason, comprehensive studies of molecular spectroscopy in thermal sources cannot be used to positively identify certain spectral features as belonging to a particular pair of quantum states, as is possible with ultracold atoms. Luckily, in the context of ultracold molecules, it isn't necessary to understand the spectrum in its entirety. The scattering properties of the ultracold atoms depend strongly only on the character of the interatomic potential at large internuclear separation, so probing the highest lying states is of particular importance. Additionally, in the context of searching for magnetic Feshbach resonances in YbLi, only the very least-bound state supported by the potential is of practical importance.

Photoassociation (PA) spectroscopy allows us to use optical photons to probe near-threshold bound states of an electronically excited potential. In the PA process, two atoms absorb a photon to create an electronically excited molecule, and this formation can be detected through heating in the trap from subsequent dissociation or through photoionization of the molecules [110]. In the limit of zero kinetic energy, this association occurs with some finite probability as long as the photon energy plus the binding energy of the molecule is equal to that of the the electronic excitation in the single atom. However, as we will explain in a later section, the probability of association is typically significant only for the near-threshold states.

While the description above might give the impression that only excited-state molecules can be formed through a PA process, a two-photon PA process can be used to connect the scattering atoms to a molecular state in the electronic ground state, allowing us to use PA to probe the ground electronic potential as well (see Figure 3.2). For this reason, our experimental study of photoassociation in the Yb+Li mixture begins with a study of photoassociation in the electronically excited YbLi* before proceeding to probe YbLi.

To the author's knowledge, no spectroscopic investigation of YbLi had been done prior to our work. Before discussing the method of spectroscopy used in this thesis, we will briefly discuss the scale of the spectroscopic mystery. The gross electronic structure of the YbLi molecule at long range is not difficult to understand: it is merely the energy of the Yb and Li atoms. As such we know that PA transitions will be on the order of 100s of THz overall. To understand the order of magnitude of the vibrational energy spacing, we model the molecule

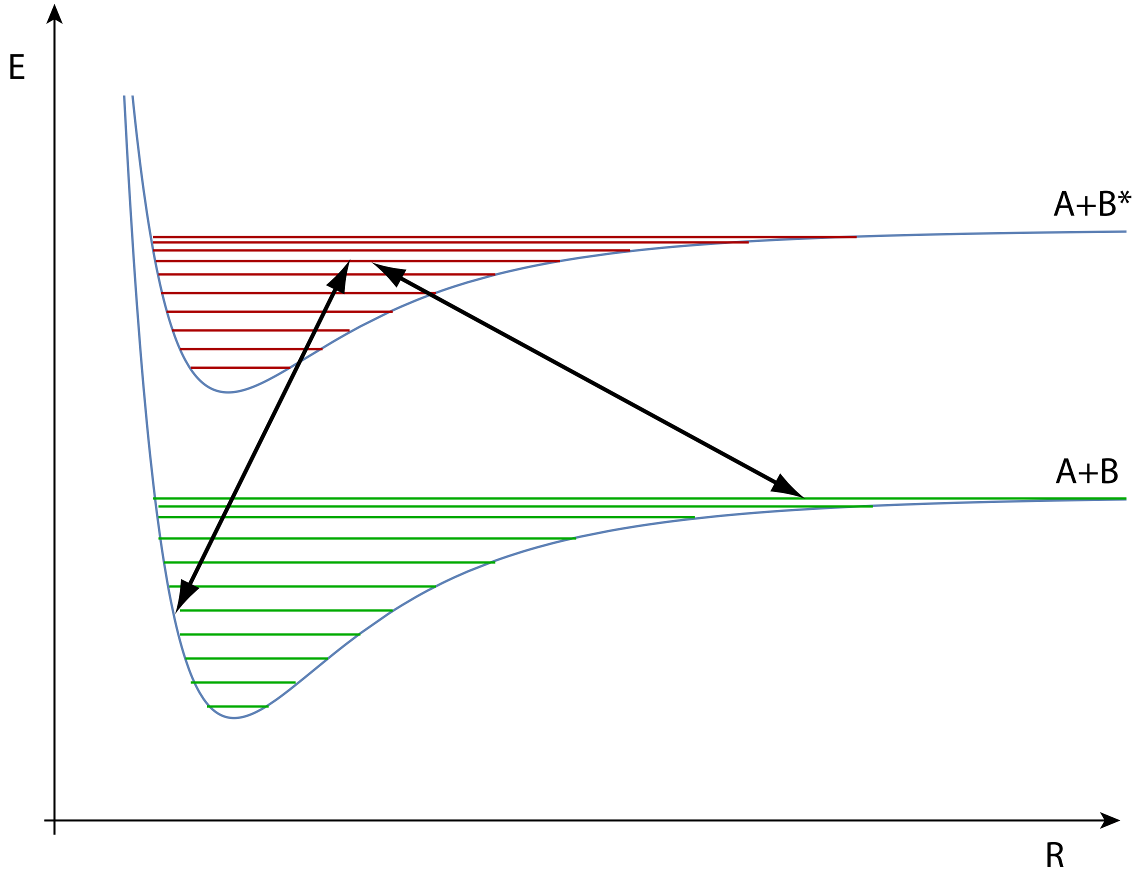

Figure 3.2: A schematic diagram for a two-photon photoassociation process. Two ground-state atoms A and B interact through the lower potential labeled AB, dependent on the internuclear separation R. A ground-state atom A and excited state atom B interact through the upper potentials labeled AB*. Green lines in the AB potential indicate vibrational modes of the ground-state molecule while red lines in the AB* potential indicate vibrational modes of the excited-state molecule. An arbitrary offset energy has been added to the potentials for clarity and the energy separation between different vibrational state is not to scale with that of the electronic states.

as a harmonic oscillator: two nuclei of mass $M \sim m_p$ with m_p being the mass of the proton.

In order for the molecule to be stable, the restoring force of the oscillator must balance the Coulomb repulsion at the equilibrium distance R_0 [111].

$$V(R) \sim k(R - R_0)^2$$

Near $R = 0$, the valence electrons overlap significantly, resulting in a potential energy on the same order as typical electronic energies such that

$$kR_0^2 \sim \frac{e^2}{R_0}$$

Here e is the elementary charge. Since the nuclei will be separated by $R_0 \sim a_0$, we make the following approximation of k.

$$k \sim \frac{e^2}{R^3} \sim \frac{m^3 e^8}{\hbar^6}$$

where m is mass of the electron. Hence, we can calculate the energy of the harmonic oscillator.

$$E_{\text{vib}} = \hbar\sqrt{\frac{k}{m_p}} \sim \sqrt{\frac{m}{m_p}}\sqrt{\frac{m^2 e^8}{\hbar^4}} = \sqrt{\frac{m}{m_p}}E_{\text{Rydberg}}$$

Thus the approximate ratio of the vibrational and electronic energies of a diatomic molecule are

$$E_{\text{vib}} \sim \sqrt{\frac{m_e}{m_p}}E_{\text{electronic}}$$

From this approximation, we believe that the vibrational state separation of the molecules should be about 2 orders of magnitude smaller than electronic states. Namely, $\sim$ 1 THz. Though owing to the anharmonicity near-threshold, the spacing will be narrower than this estimate for the most weakly bound states.

With these approximations in hand, we know approximately what a complete vibrational spectrum would look like but not the energy of each vibrational state. As mentioned in the previous section, it is not currently possible to precisely predict the vibrational spectrum of a molecule from first principles. However, for a long-range potential of the form in Equation 3.7, the spectrum of the near-threshold bound states can be approximately determined by the Leroy-Bernstein Formula, given below [112].

$$E - D = -\left[(v_d - v)\left(\sqrt{\frac{\pi}{2\mu}}\frac{\Gamma(1+1/n)}{\Gamma(1/2+1/n)}\frac{\hbar(n-2)}{(-C_n)^{1/n}}\right)\right]^{\frac{2n}{n-2}} \tag{3.8}$$

where E is the energy of a particular state of interest, D is the dissociation energy (set to zero in Figure 3.1), μ is the reduced mass of the molecule, v is vibrational number of the state of interest, n is the leading order power in the potential given by Equation 3.7, Γ is the gamma function, C_n is the appropriate dispersion coefficient and v_d is a partial vibrational quantum number that corresponds to the dissociation energy. v_d ranges from 0, in which case the least-bound state is barely below dissociation, and 1, in which case the least-bound state is maximally bound. In other words, when $v_d = 1$ an additional bound state lies at an energy just barely above threshold.

In the case of YbLi the strongest interactions between these two neutral atoms is the induced dipole-dipole interaction corresponding to $n = 6$ in Equation 3.7. By substituting this into Equation 3.8, we obtain a predictive formula for our expected vibrational spectrum near-threshold.

$$E - D \propto -\frac{(v_d - v)^3}{\sqrt{C_6}} \tag{3.9}$$

This equation has only two unknown parameters: C_6 and v_d. Thus, after experimentally determining the binding energy of two bound states, the formula is fully constrained and will be a powerful predictive tool for observation of subsequent bound states until the approximations on which the LeRoy-Bernstein Formula are based are no longer valid. Indeed, as C_6 had been theoretically calculated prior to our experimental work, it would be sufficient to find just one bound state in order to use the LeRoy Bernstein Formula to our advantage.

3.4 One-photon PA Experimental Setup

We used photoassociation to probe the near-threshold molecular states of the electronic potential manifold asymptoting at a large internuclear distance to the energy of the bare ^{6}Li ^2P + ^{174}Yb $^1S_0$ states, as seen in Figure 3.3. Addressing this manifold rather than, for example, those asymptoting ^{6}Li ^{1}S + ^{174}Yb $^{3}P_{1}$ states, has a few advantages, enumerated below.

- The fundamental limit on the PA linewidth is the same as the atomic electronic transition it is associated with and the fairly large linewidth for the Li $^{2}S_{1/2} \rightarrow {}^{2}P_{1/2,3/2}$ transition ($\Gamma = 2\pi \times 5.9$MHz) would relax the requirements on the step size in our search for the first resonances.
- The ≈ 671 nm laser light required was relatively easy to obtain even at high powers and arbitrary detunings
- Spectroscopy of this manifold, being the lowest excited state manifold in the system, will not be complicated by predissociation effects

We observed PA resonances through trap-loss spectroscopy, in which a collection of trapped atoms is exposed to PA light of various frequencies until a particular frequency is seen to deplete the number of atoms in the trap. This is an indication of molecule formation because the molecules rapidly dissociate back to atoms, releasing the binding energy as kinetic energy which is orders of magnitude higher than our trap depth. Even if PA processes happen to populate radiatively stable molecular states, they are usually not collisionally stable and thus will also be lost from the trap. Most often these trap-loss spectroscopies are carried out in a MOT. This has been done not only for homonuclear molecules where PA rates are quite strong but also for heteronuclear molecules for which PA rates are relatively weak. In 2015 our lab performed trap-loss spectroscopy on a two-species MOT of ^{174}Yb and ^{6}Li [113]. In that work we were able to observe one vibration state, which we identified as $v* = -2$ but no others.

To pursue a more extensive study of the electronically excited molecular states, we began new trap-loss spectroscopy experiments in late 2016, this time trapping the atoms in the ODT. This had the disadvantage of taking a lot longer than MOT-based spectroscopies in which atoms can be continuously reloaded into the trap while the PA laser frequency is scanned or stepped through different frequencies. In the ODT-based experiments, we would have to prepare the atoms in the ODT, expose the atoms to the PA light of some frequency, perform absorption imaging on the remaining atoms and then reload the ODT again and repeat the process for a different frequency of PA light. Collecting one data point in such an experiment takes about 15 seconds, with the preparation of the ultracold atom sample taking the majority if the time. Exposure of the PA light lasts typically 1 to 100 ms while the complete absorption imaging process takes a few 100 ms.

Despite the low data collection rate, performing these experiments in the ODT had two key advantages, both of which help us satisfy the condition of visibility of a PA resonance through trap-loss spectroscopy: that the rate of loss from the trap induced by photoassociation must be on the same order as any other loss process from the trap. The first advantage of the ODT is allowing for an increase in the PA rate. The PA rate is given by:

$$\frac{d}{dt} n_{\mathrm{Li,Yb}} = -K_{\mathrm{PA}} n_{\mathrm{Li}} n_{\mathrm{Yb}} \tag{3.10}$$

where $n_{\mathrm{Yb(Li)}}$ is the density of Yb(Li) and K_{PA} is the two body event rate constant that is independent of density. K_{PA} is determined by two parameters: the coupling matrix element of the electronic transition and the wave function overlap between the incoming scattering state and the bound state. Critically for this work, typical densities achievable in a MOT are about $10^{10}\,\mathrm{cm}^{-3}$, whereas in the ODT densities $\sim 10^{13}\,\mathrm{cm}^{-3}$ can be achieved.

In addition to increasing the PA rate by moving to the ODT, we were also able to limit one of the strongest competing loss processes that obscures the PA signal we are looking for: other kinds of PA. Necessarily, the PA light with which we searched for YbLi PA resonances can also drive Li_2 resonances. This is a particularly acute problem because the Li_2 PA resonances connect to an excited state molecular potential $V_D \sim -{}^{C_3}/_{R^3}$ owing to the resonant dipole-dipole interaction available in homonuclear systems between an s state and a p state. Examining the LeRoy Bernstein formula and comparing it to the $V_D \sim -{}^{C_6}/_{R^6}$ potential for YbLi* shows that the Li_2 resonances will be more numerous. Further, the longer range of the homonuclear interaction means that the coefficients K_{PA} will typically be much larger for Li_2 than for YbLi. In this way, homonuclear PA represents a strong background that must be curtailed in order to observe the heteronuclear resonances. Suppressing PA rates can be done simply by suppressing collisions between two Li atoms generally. Because we are working at temperatures well below the p-wave threshold for Li, we may limit collisions between two Li atoms simply by keeping the sample spin polarized so the sample in our trap is composed of identical fermions. Unlike in the MOT, we can readily prepare the Li cloud in the ODT in a spin polarized state. Beyond preparing the cloud in a single spin state, we also mitigate affects that would disturb the polarization. Specifically, we prepare the Li atoms in a stretched ground spin state ($|3\rangle = |m_s, m_i\rangle = |{-}{}^1\!/_2, -1\rangle$), which means that only returning to the original state is allowed by dipole selection rules. This prevents the PA laser beam from transferring atoms to other ground spin states by off-resonant scattering.

Having previously observed the $v* = -2$ resonance in our earlier PA experiments and believing that $v* = -1$ could not be observed due to large trap loss from spontaneous scatter of the atomic transition, we sought to observe the $v* = -3$ resonance with the new experiment. Each experimental run began with the creation of an ultracold mixture of atoms loaded into the ODT. For our initial experiments, we performed a modest amount of evaporative cooling and then held the trap depth constant for 1 second for thermalization. At this point, a typical starting Li(Yb) atom number was $2.0 \times 10^5 (1.5 \times 10^6)$ and they were at a temperature of $35\,\mu$K. The trap frequencies for Li were $\omega = 2\pi\{485, 330, 195\}$ Hz, with the highest trap frequency corresponding to the axis parallel to that of gravity. Subsequent changes to these initial parameters are noted along with the data presented in the remainder of this chapter. After preparation the sample was exposed to PA light of various intensities and pulse lengths, which we varied in order to achieve optimal signal.

The PA light laser system is principally composed of: an external cavity diode laser (ECDL) (DL-100 with an EYP-RWA-0670 diode), a lab-built tapered amplifier system (EYP-TPA-0670 TA chip), a Li vapor cell and a single pass acousto-optic modulator (AOM). The Li vapor cell was necessitated by the broadband spectrum of the tapered amplifier chip.

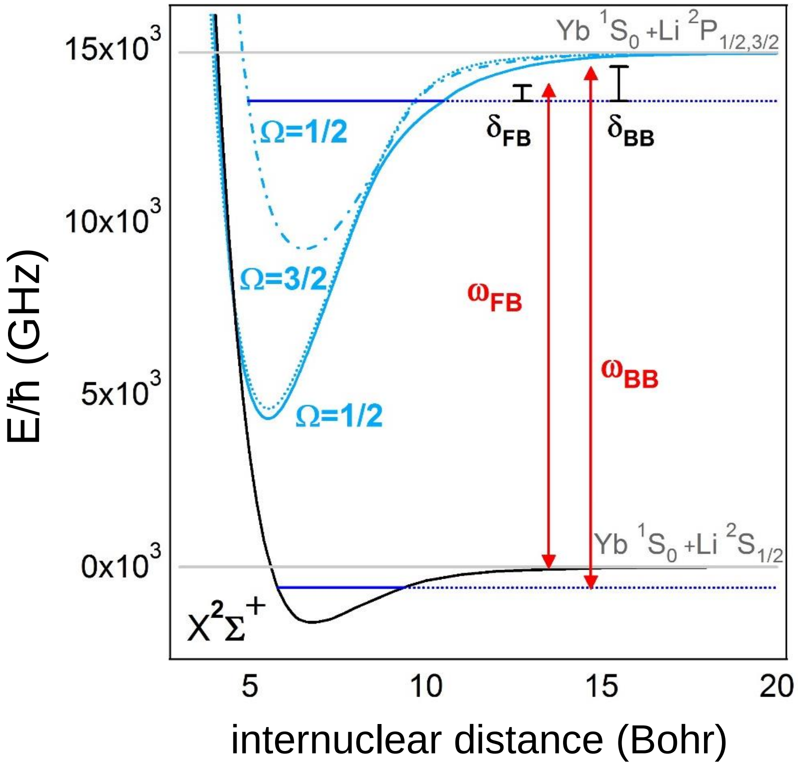

Figure 3.3: A schematic representation of the PA process is shown on top of the interatomic potentials for the relevant electronic states of the YbLi molecule. Atoms begin in the free atom pair state, which at large internuclear distance is simply the energy of the two ground state atoms. The free-to-bound laser field with frequency ω_{FB} connects the free atoms to the manifold of electronically excited states corresponding to a ground Yb atom and a Li atom excited along the D lines. For two-photon spectroscopy, the bound-to-bound laser field with frequency ω_{BB} is added to connect the electronically excited molecules to ground molecular states.

Although most of the TA spectrum is dominated by the frequency of the seed beam supplied by the ECDL, the TA acts as a light-emitting diode itself, causing output of amplified spontaneous emission (ASE). Figure 3.5 provided an example of the free-running (unseeded) and injected (seeded) TA similar to that used in this work for the PA light. The spread of the residual ASE in the spectrum was much larger than the detuning of the PA light from the atomic resonance, meaning that atoms would be exposed to resonant light if unfiltered. We found that the vapor cell needed to be heated to about 400 degrees and the PA beam sent as close to the source of the vapor as possible (skimming the bottom of the cell viewports) in order to remove the resonant component of the light. We confirmed that the resonant component was removed by noting that the lifetime of the Li atoms exposed to PA light in the trap increased quadratically with the detuning from the atomic resonance. Before the successful filtering the lifetime was linear in the detuning.

After passing through the vapor cell, the PA light was sent through a single pass AOM operating at 230 MHz and the -1 order was coupled into a polarization-maintaining (PM) fiber, allowing for fast switching *or* intensity feedback on the PA beam, whichever is more important (a shutter is also used for slow switching and blocking of leaked light during the preparation stages of the sequence). The output of the fiber was placed on the vertically oriented breadboard above the vacuum chamber. A single 100 mm lens placed just above the upper viewport of the vacuum chamber focused the PA beam near the ODT. We estimated the waist of the PA beam to be about 75 μm using a beam profiler with a mock setup of this simple beam path off the main optics table. A flipper mirror was used in the vertical MOT path to allow the PA beam to propagate from the top of the vacuum chamber towards the ODT.

The frequency of the PA laser was stabilized by using the reading of a wavemeter (High Finesse WS-7) to feedback to the ECDL grating angle. Though the wavemeter is quoted to a precision of 10 MHz, we determined through high field imaging resonances of Li atoms that the laser linewidth was less than 5 MHz when locked.

Because our typical preparation of ultracold atoms ends with Li atoms polarized in $|2\rangle$

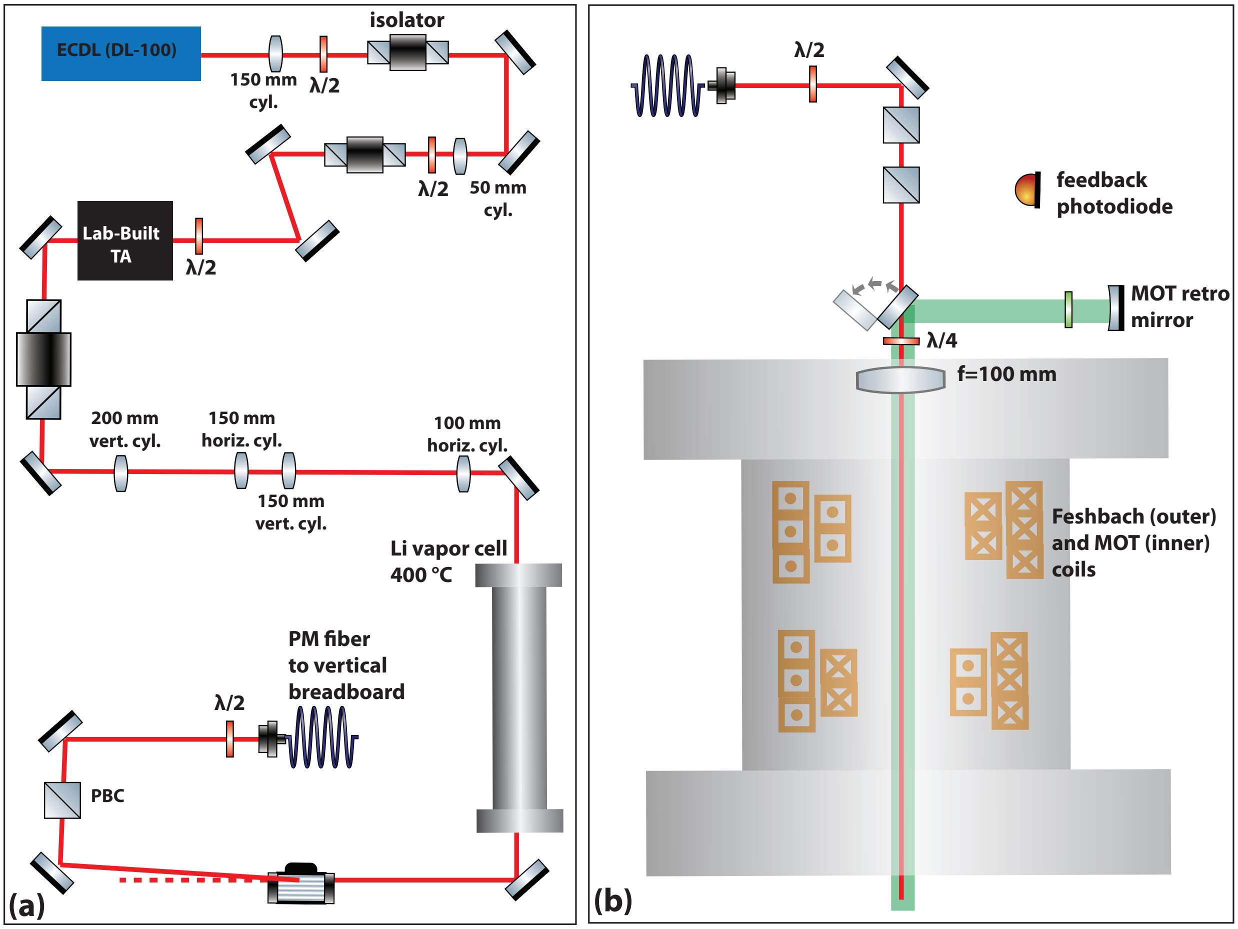

Figure 3.4: A simplified sketch of the experimental setup for one-photon PA. (a) The setup on the PA table: a tunable ECDL laser was the source of the PA light. The ECDL injects a lab-built TA unit, producing a higher intensity beam at the same frequency. After passing through a pair of cylindrical telescopes, the beam was spectrally filtered with a Li vapor cell, removing the resonant component of the TA's broad ASE spectrum. An AOM was used for fast shutoff and intensity stabilization. A PM fiber transferred the PA beam to the main optics table in (b). The PA beam followed the path of the vertical MOT retroreflection and was focused near the ODT by the f=100 mm lens mounted just above the top viewport and therefore recessed into the "bucket" that holds our magnetic field coils. After the MOT phase of each experimental run, a motorized flipper mirror on the vertical breadboard would move out of the way of the PA beam. Two polarizing beam cubes were used to create a pickoff beam required for stabilization of the intensity of the PA beam: the first cube to converted any polarization noise to intensity noise and passed on a clean polarization to the second cube such that the final reflection to the photodiode would remain proportional to the power

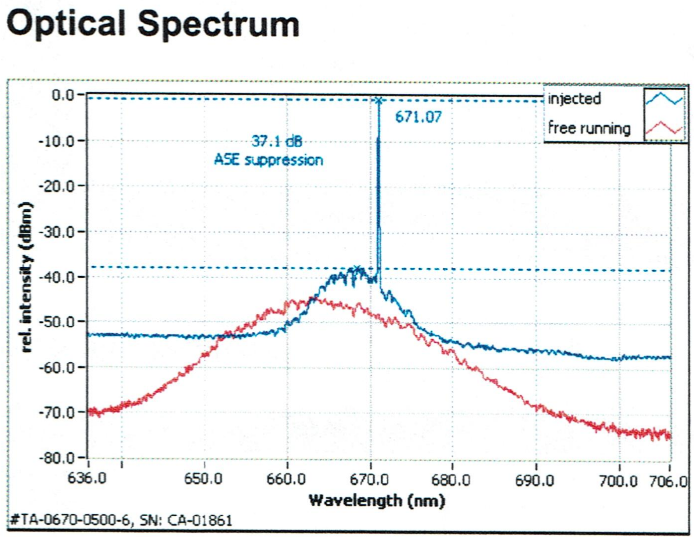

Figure 3.5: The spectrum of the tapered amplifier used in our experiments, both seeded (blue trace) and unseeded (red trace). This example spectrum was provided in the data sheet for the Toptica TA-100 laser serving as our Li cooling laser.

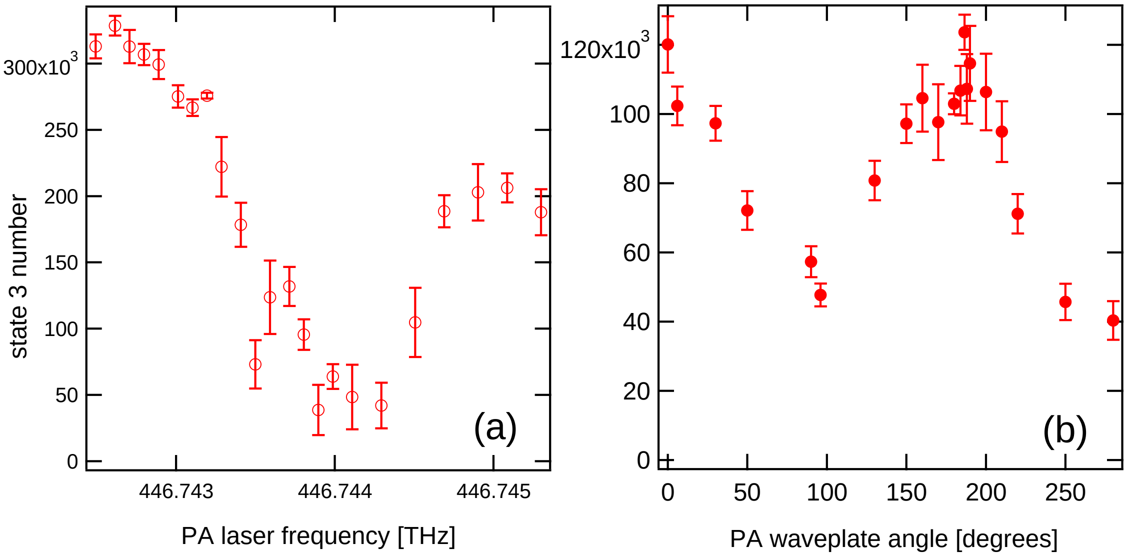

Figure 3.6: Suppression of homonuclear Li_2 PA loss. (a) A Li_2 PA resonance was observed with a 20 ms exposure of PA light at about 500 μW. (b) The PA laser frequency was set to resonance at 446.744 THz and the atoms in the trap were exposed to the light for a fixed interval of time. The PA beam polarization was changed by turning the quarter wavelate just above the focusing lens.

(see Figure 2.3), we transferred the atoms to the desired $|3\rangle$ state just before the PA pulse is applied. For details on this process, see Section 5.6. Finally, we used our observation of a known Li_2 PA resonance (see Figure 3.6(a)) to set the polarization of the PA beam to σ^- such that spontaneous scattering from the atomic transition minimally populated ground states other than ($|m_s, m_i\rangle = |-1/2, -1\rangle$). To do this, we exposed the atoms to a fixed length PA pulse resonant with the Li_2 PA resonance and turned the angle of the quarter waveplate just above the vacuum chamber (see Figure 3.4) until the atom loss in $|3\rangle$ was minimized.

3.5 *Excited Bound States*

3.5.1 Loss Resonances

Figure 3.7 shows the first strong observation of heteronuclear PA in the ODT, corresponding to resonance with $v* = -2$. We distinguished the heteronuclear PA resonance from nearby homonuclear resonances by repeating the spectroscopy in the absence of Yb. To perform the experiment without Yb we removed it from the trap with a resonant light blast on the $^1S_0 \rightarrow {}^1P_1$ transition prior to the PA light pulse. We note here that despite knowing exactly where to look for this resonance because we had observed it in our previous MOT-based experiments, the first observation of this heteronuclear resonance was quite faint. It was then that we realized that the heteronuclear PA rate was quite sensitive to the alignment of the second beam of our crossed ODT. In this sense, heteronuclear PA is a method for determining the extent of the actual spatial overlap of the two clouds in the trap.

The proximity to multiple homonuclear PA lines highlights the advantage of working in the ODT rather than the MOT. As an approximate comparison of the two methods we have plotted the trap-loss signal from both the ODT and the MOT in this range of frequencies in Figure 3.8. The colder temperature of the ODT alone (factor of 10 for Yb and 100 for Li) allows the YbLi resonance to be resolved against the background of multiple nearby Li_2 resonances. However, as is indicated by the gaps in the red trace, we were unable to scan the full frequency range in this area due to residual atom loss from homonuclear PA.

Our initial attempts to observe additional resonances began with a comprehensive scan which was uninformed by the best values to use for the PA power and exposure time and was also susceptible to low signal due to poor interspecies overlap. However, under the following conditions we scanned the range of 120 GHz to 450 GHz below the Li D2 resonance at 446.80014 THz: 0.5 mW with 1 second of exposure with a triangle wave frequency sweep amplitude of 460 MHz. After observing the $v* = -2$, we were able to use that signal to optimize the overlap and chose to revisit a narrower scan range for $v* = -3$, which was motivated by the input of the theoretically predicted value of C_6 into the LeRoy Bernstein

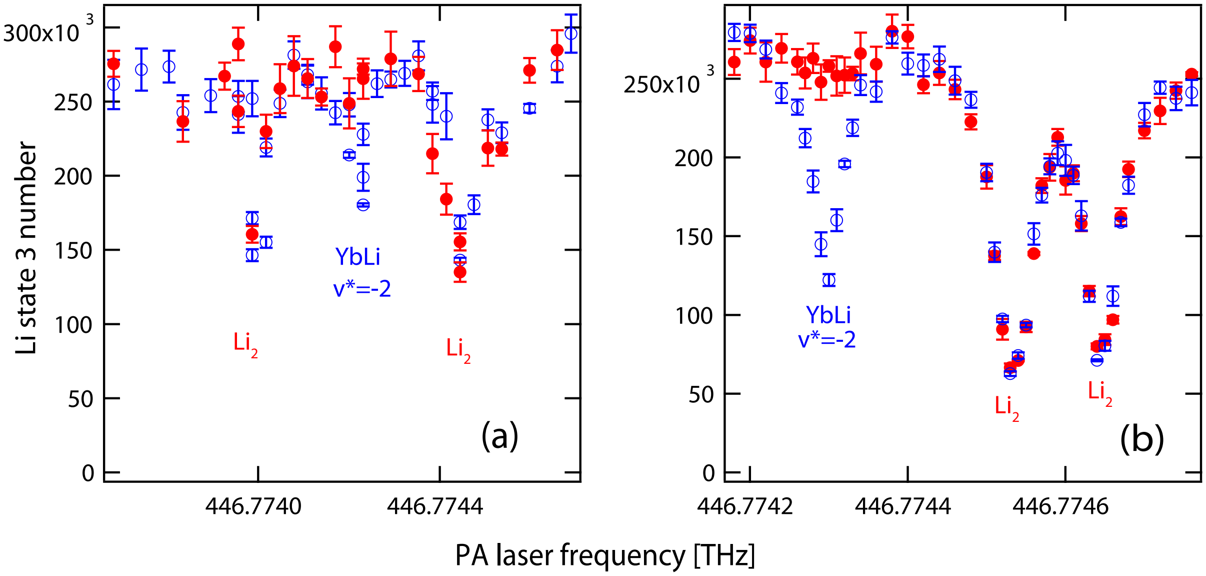

Figure 3.7: Observation of $v* = -2$ through trap-loss spectroscopy. The experiment at each PA laser frequency was done twice: first in the presence of Yb (open blue circles) and then the absence of Yb (closed red circles). From (a) it appears that the interpecies YbLi PA resonance is within a few linewidths of a homonculear Li_2 PA resonance on either side. In (b) it appears that the homonuclear resonances on the blue-detuned side of the heteronuclear resonances is a doublet. For this data the power in the PA beam was 150 μW and the exposure time was 100 ms.

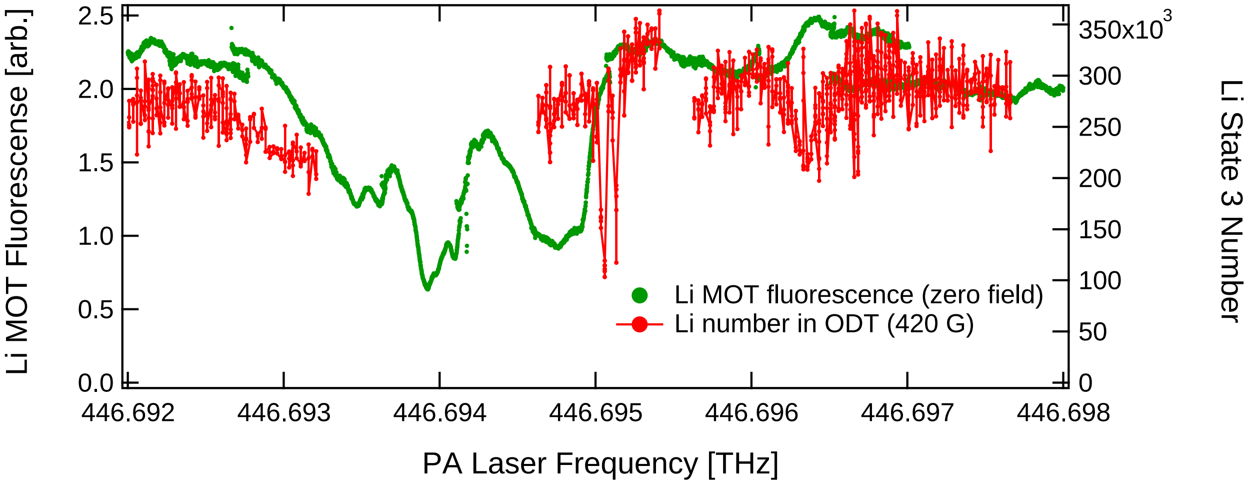

Figure 3.8: An approximate comparison between the utility of trap-loss spectroscopy in a dual species MOT as we used in [113] and an atomic mixture trapped in an ODT as we used in [114]. The green line represents the fluorescence collected from the Li atoms in the dual species MOT as the PA laser frequency was changed and the red dots (connected by lines for clarity) represent absorption imaging measurements of trapped Li atoms after exposure to the PA light. The separation of the homonuclear Li_2 PA lines is visible only in the ODT sample, making the observation of the heteronuclear resonance much easier. This is only an approximate comparison because of two important caveats: the field at which these two measurements were done was not the same and the intensity of the PA light was varied throughout the ODT data set.

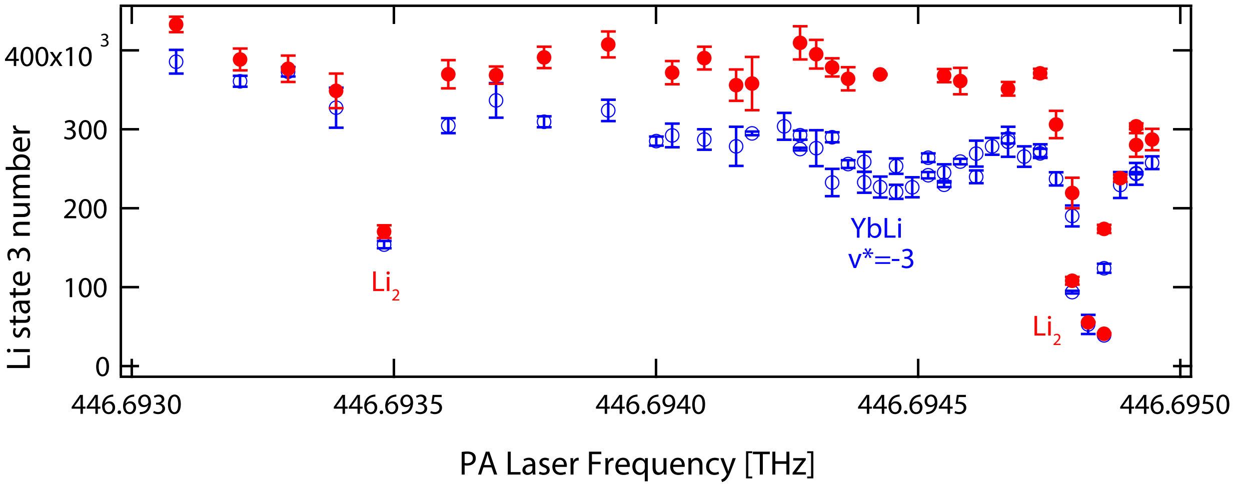

Figure 3.9: Observation of $v* = -3$ through trap-loss spectroscopy. Careful comparison between the Li atom number with (open blue circles) and without (closed red circles) Yb was required to distinguish the heteronuclear resonance from the two nearby homonuclear resonances. For this data there was 4 mW of power in the PA beam and the exposure time was 100 ms.

formula. In this second attempt we were able to observe the much weaker $v* = -3$ resonance, shown in Figure 3.9, which was not only easy to miss due to its low loss amplitude but also because the feature appeared to be anomalously broad.

3.5.2 Excited State Spectrum

The observation of the $v* = -3$ allowed us to experimentally constrain both unknown parameters of the LeRoy-Bernstein Formula (equation 3.9), allowing us to predict the locations of subsequent bound states. In practice, we found the Leroy-Bernstein formula became less effective for deeper bound states, as expected. For example our original LeRoy-Bernstein fit to the spectrum which included data on $v* = -2, 3$ missed $v* = -6$ by over 10 GHz. However, we found an alternate fitting procedure that did a better job at predicting the subsequent binding energies; rather than fitting the LeRoy-Bernstein formula to the entirety of the spectrum we had hitherto observed, we fit it to only the deepest few bound states (or those states just above the state we were wanting to predict for). In this way, we were able to observe all the bound states ranging to $v* = -9$ as shown in Figure 3.10. States deeper than $v* = -9$ could not be observed as the PA frequencies for these states lay outside the bandwidth of our PA laser. The binding energies of the eight states observed in this vibrational series are presented in Table 3.1.

It should be stressed that this method of search left gigantic swaths of the PA spectrum for YbLi unobserved. Based on the agreement with the LeRoy Bernstein formula, we know that this is a vibrational series corresponding to a single electronic state. We never observed a rotational spectrum associated with one of the vibrational states either because rotational states other than those we observed lay outside of our search range (which was limited because of the low data collection rate of this method) or more likely due to some sort of effective selection rule in this spectroscopy. Nor did we observe any PA lines outside of this vibrational series, corresponding to different electronic states, as we did in the MOT PA experiment, although we did not focus on detecting these states.

3.5.3 Free-to-Bound Transition Strengths

To quantify the relative strength of the PA resonances, we performed lifetime measurements on the atoms in the trap when exposed to PA light. We compared these lifetimes against the losses in the absence of PA-driven trap loss by also performing lifetime measurements without Yb. Figure 3.11 shows the rate of PA and non-PA loss or "background loss" for both the $v* = -2$ and $v* = -3$ resonances. Because the resonant PA light addressing $v* = -3$ is much further detuned from that of $v* = -2$ the lifetime under the same conditions is much longer. But despite this it is clear that the separation between the PA lifetime and the background lifetime is greater for $v* = -2$ because the PA rate is significantly higher. This is expected based on the Franck-Condon Principle: transitions between vibrational states of a molecule will be more likely to happen if the wavefunction overlap between the two states is higher. In the case of free-to-bound PA, the transition is actually between a scattering state

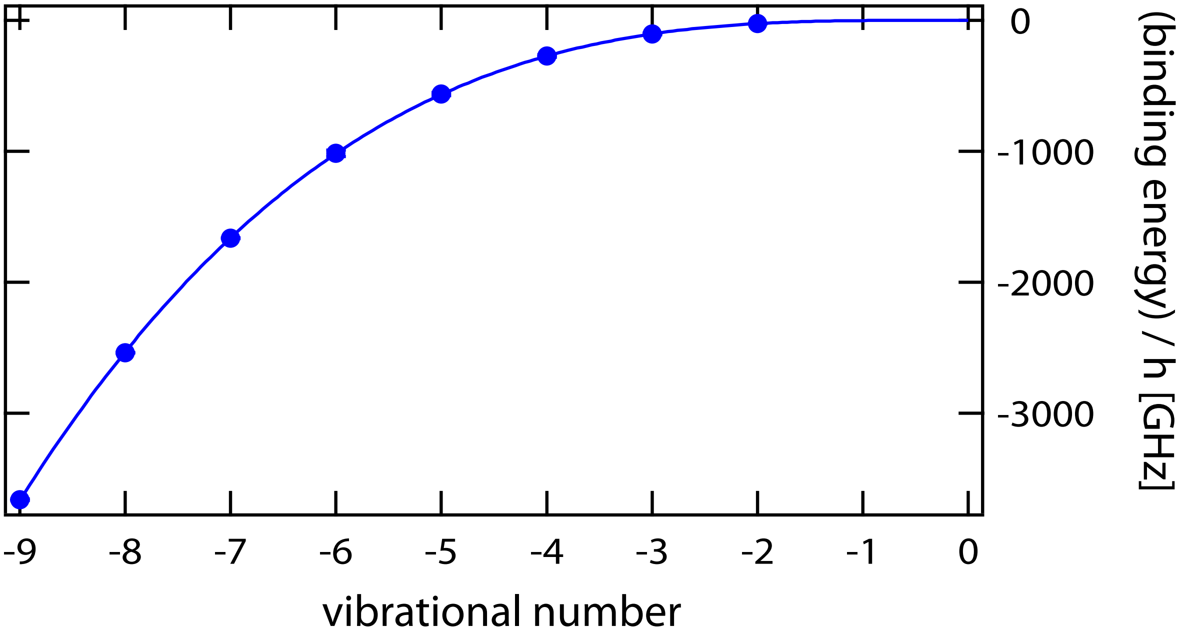

Figure 3.10: The binding energies of the near-threshold bound states of the electronically excited molecular potential manifold asymptoting to ^{6}Li ^{2}P and ^{174}Yb $^{1}S_0$. The error bars on each point are within the symbols. A LeRoy-Bernstein fit shows good agreement with the binding energies of these loosely bound states.

and a vibrational state. The bound state being concentrated at the outer turning point of the interatomic potential means that the highest lying vibrational states will generally have the highest wave function overlap with the scattering state. However, because the scattering wave function oscillates away from the localized peak, the wave function overlap will not decrease monotonically for deeper vibrational states but will exhibit oscillatory behavior mimicking that of the scattering wave function.

The extent of wave function overlap between vibrational states is parameterized by the Franck-Condon factor. We determined the Franck-Condon factors for the eight resonances observed in this work by analyzing the trap lifetimes taken for each state during PA exposure using the following assumptions.

- The loss from PA was equal to the difference in the rates gathered from data as in Figure 3.11. In other words, the removal of Yb didn't affect any loss rates other than those from heteronuclear PA.
- The intensity of light used in these experiments was well below saturation of the PA transition(further discussion of this below).
- The Li and Yb clouds were perfectly centered on each other for maximum spatial overlap.
- The electric dipole matrix element between the excited vibrational state and the ground state is the same as that between the unbound atomic state and the ground state.
- The radiative lifetime of the excited vibrational state is the same as the linewidth of the trap loss.

With these assumptions, we first experimentally determined the value of K_{PA} using equation 3.10 and then related this to the Franck-Condon factor by comparing this with the form of K_{PA} [115].

$$K_{\mathrm{PA}} = K_{\mathrm{PA}}^{\mathrm{max}} \frac{4\Gamma}{\gamma} \tag{3.11}$$

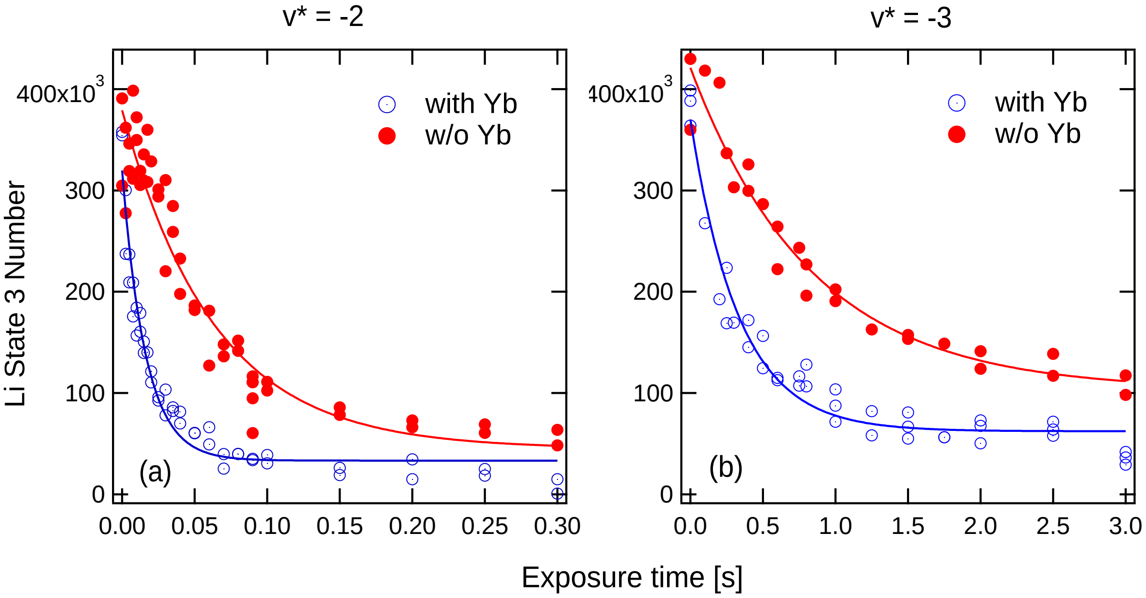

Figure 3.11: A comparison of the lifetimes of the Li atoms in the trap when exposed to resonant PA light under similar conditions. For the left-hand plot, the PA light was set to address the $v* = -2$ bound state and for the right-hand plot it was set to address the $v* = -3$ bound state. Both experiments were done with (blue open circles) and without Yb (red closed circles). Note that the timescales of the two plots differ by a factor of 10. While light tuned to address the $v* = -2$ caused significantly faster non-PA loss (red circles) due to its smaller detuning from the electronic transition in Li, the PA loss was also much greater than for $v* = -3$, owing to a larger Franck-Condon factor and in total the separation of the PA and non-PA loss timescales are greater for $v* = -2$.

Here, Γ is the atom-molecule coupling, γ is the linewidth of the excited vibrational state, and $K_{\mathrm{PA}}^{\mathrm{max}}$ is the unitarity-limited rate for any two-body collision given by

$$K_{\mathrm{PA}}^{\mathrm{max}} = \frac{\hbar^2}{\mu^{3/2}}\sqrt{\frac{2\pi}{k_B T}} \tag{3.12}$$

with μ as the reduced mass of the molecule. Γ is the value of interest as it depends on the Franck-Condon factors ($\mathrm{f_{FC}}$):

$$\Gamma = 2\pi\hbar\Omega^2 \mathrm{f_{FC}} \tag{3.13}$$

where Ω is the Rabi frequency of the electronic transition to the excited state.

Figure 3.12 shows the results of these measurements. As expected, the Franck-Condon factors drop off sharply as the states become more deeply bound but they do not do so monotonically. Figure 3.12 also displays the experimentally observed widths for the trap-loss measurements. The apparent anti-correlation between the Franck-Condon factor and the width is striking given that the calculations of the Franck-Condon factor explicitly included the dependence on the observed width. The cause of this anti-correlation is not currently known.

The magnitude of the observed PA resonance widths is also something of a mystery as it is theoretically expected that the radiative linewidths of these near-threshold states would be about the same as that of the electronic transition, $\Gamma = 2\pi \times 5.9$ MHz [116]. There are of course several factors other than the radiative linewidth that can contribute to the width. Above saturation the linewidth can be power broadened. We have attempted to power broaden the $v* = -2$ and $v* = -7$ lines but were not able to observe any significant dependence of the experimentally observed linewidth on the intensity within the range of intensities we could use (see Figure 3.13). In addition to trap loss being driven by excited state molecules which are radiatively transferred back to atomic states (either stimulated or spontaneous), excited molecules could de-excite to different molecular states, broadening the total linewidth. In particular, the 1064 nm light used to create the ODT has the correct order of magnitude energy to drive molecules between different vibrational states (though it is not known if 1064 nm is near resonance for the YbLi molecule in particular). To eliminate

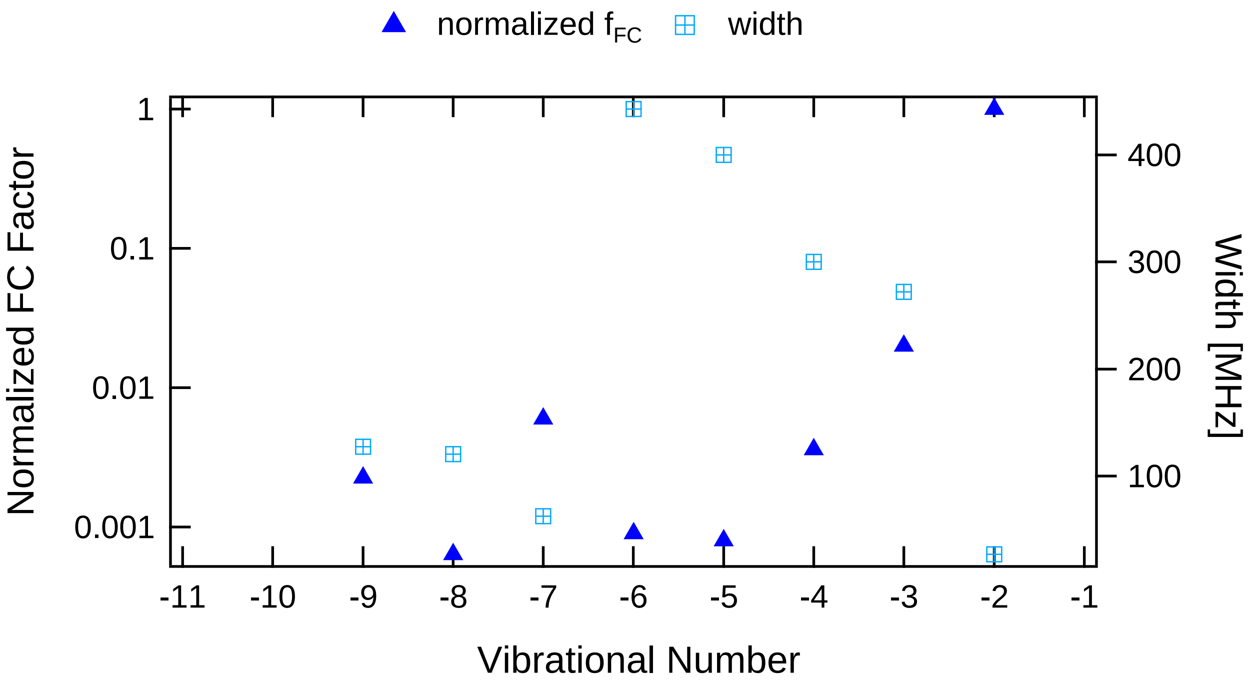

Figure 3.12: Characterizing the strength of the PA transitions. By measuring the lifetimes of the Li atoms in the presence of resonant PA light and comparing with the unitarity-limited rate determined by the overlap density of the Li and Yb clouds we can determine the value of the Franck-Condon factor, which is normalized to the Franck-Condon factor of $v* = -2$. Also plotted here are the Gaussian widths of the loss features. Note that the widths in each case were taken with different intensities of the PA power.

vibrational number	binding energy	normalized Franck-Condon factor	resonance width	power /beam waist	exposure time
$-v*$	GHz		MHz	mW/μm	ms
2	25.17	1	26.9	1.5/75	20
3	105.07	0.0216	272	4/75	100
4	272.07	0.0036	300	38/75	100
5	563.14	0.0008	400	43/75	500
6	1014.08	0.0009	443	39/38	200
7	1662.96	0.006	62.6	4.5/38	200
8	2536.04	0.0006	121	28/38	200
9	3660.56	0.0022	127	28.5/38	100

Table 3.1: The binding energies of eight of the highest-lying bound states of the observed ^{174}Yb^{6}Li excited state potential are presented along with some experimental details. The binding energies in this table are reported for a bias field of 420 G with σ^- light. Reporting the binding energy at zero field would require information on the excited state magnetic moments which we did not measure for all states. The binding energies are referenced against the zero field D2 transition in Li at 446.80014 THz. The typical starting Li(Yb) atom number was 4×10^5 (3×10^6). $v* = -1$ could not be observed due to rapid background loss from spontaneous scatter off the atomic resonance. This spectroscopy was performed in an 8.15 W trap with a painting amplitude of 0.5 V.

this possibility, we repeated the trap-loss spectroscopy technique while eliminating the effect of the ODT light. We pulsed the ODT light out of phase with PA light such that the atoms never experienced both optical fields at once but remained localized at the location of the trap. Under these conditions, we still observed loss from the atom cloud, presumably driven by atoms that achieve too much kinetic energy through dissociation during the PA phase to be recaptured by the ODT light. Indeed, the linewidth of the trap loss in the modulated case was the same as that in the unmodulated case, even when the time averaged trap depth and the time averaged PA intensity was the same in both cases.

Since a connection to other molecular states due to the trap light is not the reason for our anomalously broad PA resonances, one theory is spontaneous decay not to free atoms but to ground state molecules, an indication of unusually large Frank-Condon factors between high-lying vibrationally excited states and molecular ground states. To some extent this is an expected feature of heteronuclear dimers for which, in contrast to homonuclear dimers, the short range potential in the ground and excited states are quite similar as the excited state is not distorted by the relatively long range $V_D \approx \frac{C_3}{R^3}$ potential between the S and P states of homonuclear atom pairs.

3.5.4 Excited State Magnetic Moments

For the vibrational series observed in this work, we do not know much about the electronic state other than it converges to that of Yb ${}^1S_0$ + Li ${}^2P$ for large internuclear distance. In the spherically symmetric potential of a nucleus within an atom, an electron's state can be characterized simply by its principal quantum number n, the orbital and electronic angular momentum ℓ and s as well as their respective projections, m_ℓ and m_s. This formulation cannot be exactly applied to the electrons in dimers (though in some cases it can be approximately used) for multiple reasons. First, the involvement of two nuclei breaks the spherical symmetry of the field seen by the electrons and the resulting torque will cause the electron angular momentum to precess about the internuclear axis. How that precession happens depends on the strength of the spin-orbit coupling within the constituent atoms. In the

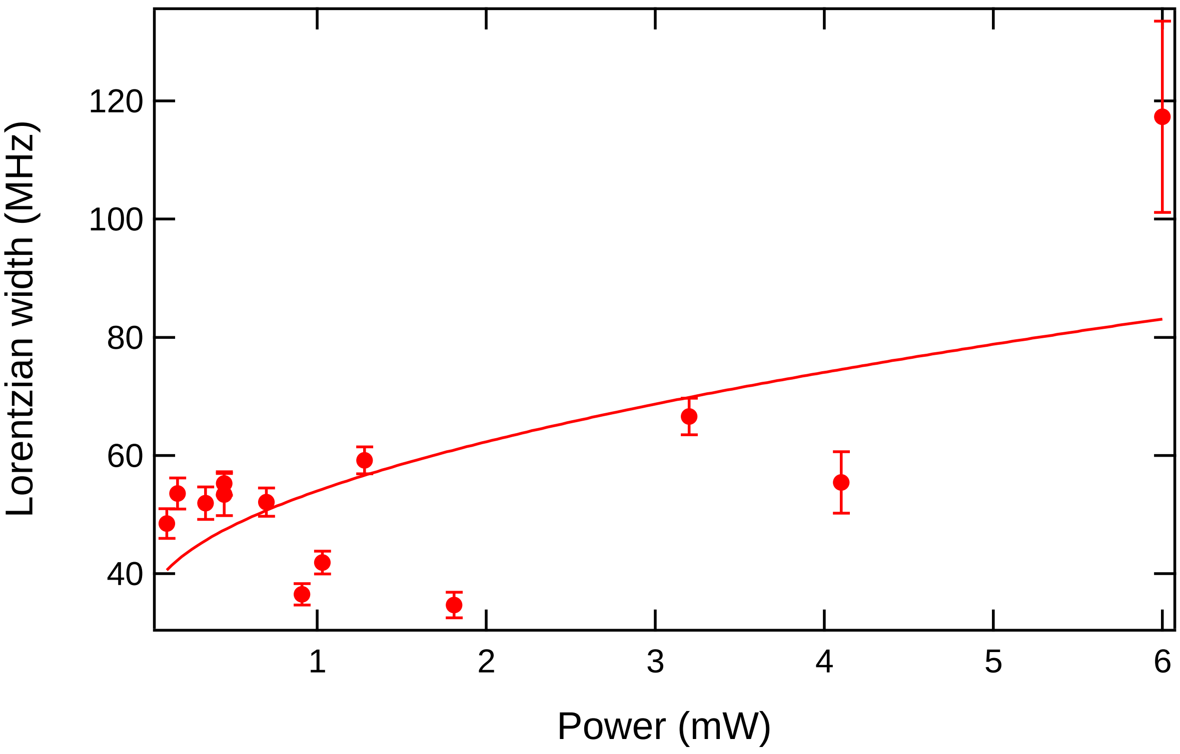

Figure 3.13: Attempt to observe saturation of the $v* = -2$ PA resonance. We were unable to measure the width at higher PA laser powers because the nearby homonuclear resonances broadened much faster that this heteronuclear line, obscuring the resonance of interest entirely at powers above about 6 mW. A square root function is drawn to suggest the theoretically achievable dependence.

case of the weakly bound molecules studied in this thesis, the spin-orbit coupling within the atom is strong meaning that $\vec{L}$ and $\vec{S}$ add vectorially to form $\vec{J_a}$ which then precesses around the internuclear axis. In this case, the interatomic potentials associated with these states are distinguished by the projection of $\vec{J_a}$ onto the internuclear axis which is conserved and assigned the quantum number Ω (see Figure 3.3).

A second complication in designating the electron's quantum state arises from the motion of the nuclei. In Section 3.1, we assumed that electrostatic interactions for the electrons were independent of the motion of the nuclei. But when considering the angular momenta of the electrons, we cannot neglect the fact that the nuclear motion associated with rotation is also quantized. This angular momentum can couple to the electronic angular momentum meaning that the electronic angular momentum states no longer represent eigenstates of the system. In the case of the dimers studied in this work, $\vec{J_a}$ couples strongly to the internuclear axis and subsequently couples to the rotation vector $\vec{R}$ to form the total angular momentum $\vec{J}$.

In the explanation above, we made several assumptions about the relative strengths of the various couplings. This set of assumptions was studied along with other limiting cases by Friedrich Hund and subsequently given the name 'Hund's case c.' However, if we were to extend our studies of the YbLi excited state potential beyond the most weakly bound states, we would expect these assumptions to fail as the individual components of the electronic angular momenta coupled more strongly to the internuclear axis than to each other, in which case they would be better described by Hund's cases a or b. In all, the model of angular momentum coupling in dimers is always an approximation.

Nevertheless, in the framework of Hund's case c it may be possible to study the magnetic moment of the electronically excited molecule in order to guess which potential in Figure 3.3 the vibrational series observed corresponds to. To this end, we measured the magnetic moment of two different vibrational states in this series as shown in Figure 3.14. This measurement was simple but time consuming because it required that we repeat the PA spectroscopy on a given vibrational state at multiple different fields, as shown in Figure 3.14.

After noting the apparent binding energy of the molecule relative to the zero field atomic energy, we subtracted the shift of the Zeeman shift of the ground states atoms to find the Zeeman shift of that particular vibrational state as shown in Figure 3.15. Since there are no unpaired electrons in Yb it is interesting to compare these magnetic moments to those of Li in the ^2P states, which are given by $g\mu_B m_J B$ for large fields with g being the g-factor for the appropriate fine structure state $^2P_{1/2}$ or $^2P_{1/2}$, μ_B is the Bohr magneton, m_J the projection of the total electronic angular momentum of the atom and B the magnitude of the external field. The comparison of the free atom magnetic moment with those measured for $v* = -5, -7$ are shown in Figure 3.16. The deviation from the atomic limit is tantalizing proof of the complexity of the molecular energies' dependence on the contributions from various different angular momenta. However, because we were principally interested in molecule formation rather than a study of molecular structure, we chose not to pursue this line of research any further.

3.6 Two-photon PA Experimental Setup

Utilizing our knowledge of the excited state PA spectroscopy, we probed the YbLi molecular ground state through two-photon PA. To understand the basis of this technique, refer to Figure 3.3. For this technique, we replicated the conditions of one-photon PA, referring to the laser field which drives atoms into the excited molecular state as the free-to-bound laser. If the free-to-bound (FB) laser is tuned to a one-photon PA resonance, a fixed amount of atom loss will occur in fixed time. The second laser field in this two-photon scheme is referred to as the bound-to-bound (BB) laser. When the BB laser energy is the same as the energy splitting between a bound state in the electronic ground state and one in the electronic excited state, the excited state will experience Autler-Townes (AT) splitting, a manifestation of the AC stark shift from the bound-to-bound laser mixing the ground molecular and excited molecular states. As can be seen in Figure 3.17, this effectively makes the FB laser non-resonant, suppressing the PA atom loss. This suppression forms the signal with which to probe the bound states ground electronic potential.

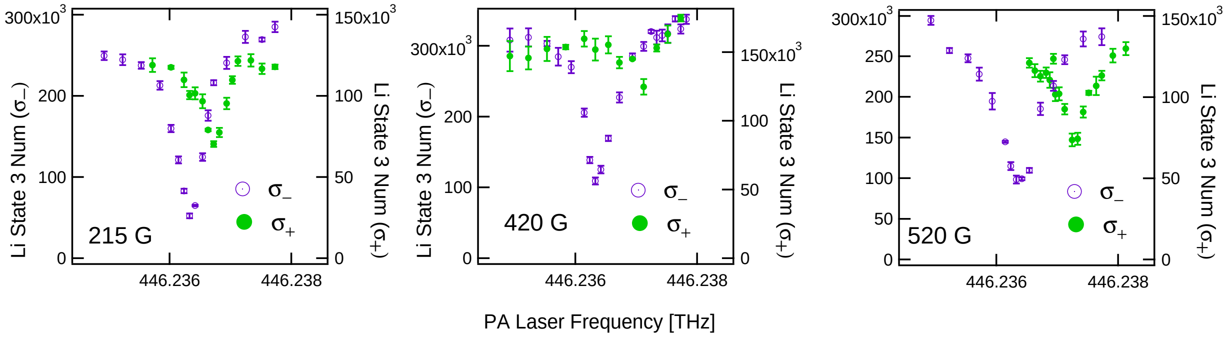

Figure 3.14: The magnetic moment of the $v* = -5$ state was measured by repeating the PA spectroscopy at multiple fields. Because the excited state manifold splits into different total spin projections, we performed this experiment with both σ^+ PA laser light (green filled circles) to address the upper state and σ^- (purple open circles) to address the lower state. Note that this method merely shows at which frequency the FB transition energy is the same as the PA laser fields and therefore doesn't show the shift of the excited states directly. Also note that the background number of atoms remaining in the trap is about half as much for the σ^+ data as the σ^1 owing to the possibility of populating additional ground hyperfine states through off-resonant scattering.

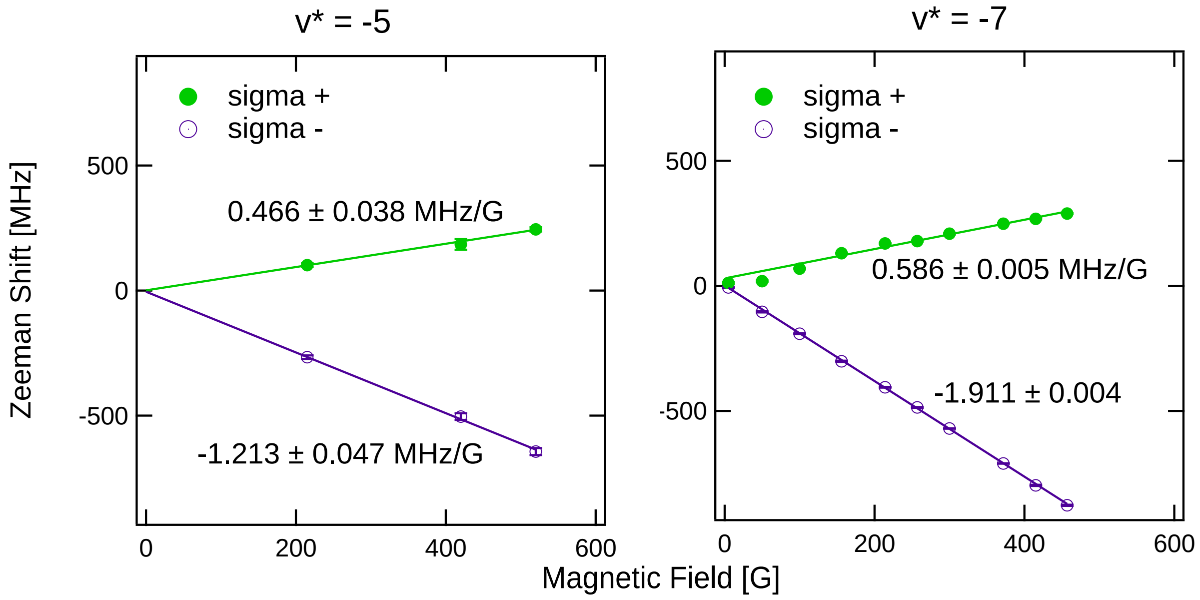

Figure 3.15: The Zeeman shifts of two excited molecular states, determined by repeating the spectroscopy at multiple fields, as shown in Figure 3.14.

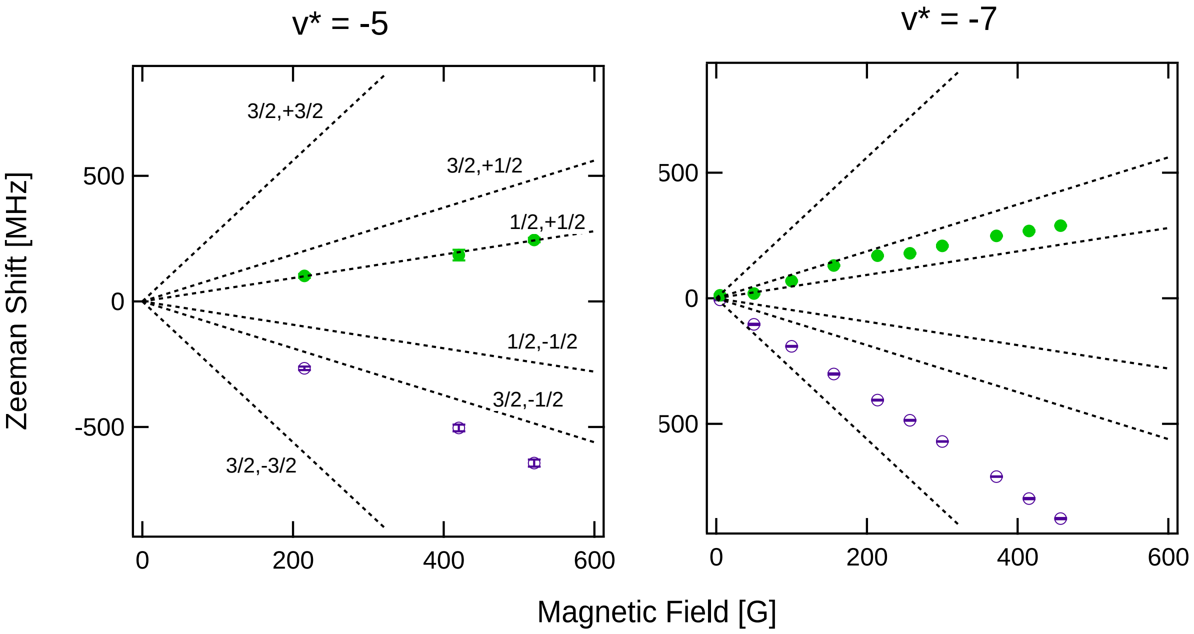

Figure 3.16: The Zeeman shifts of two excited molecular states shown in Figure 3.15 are compared to those of the Li ^2P excited states in the high field limit. Each ^2P magnetic substate is labelled by the values J, m_J.

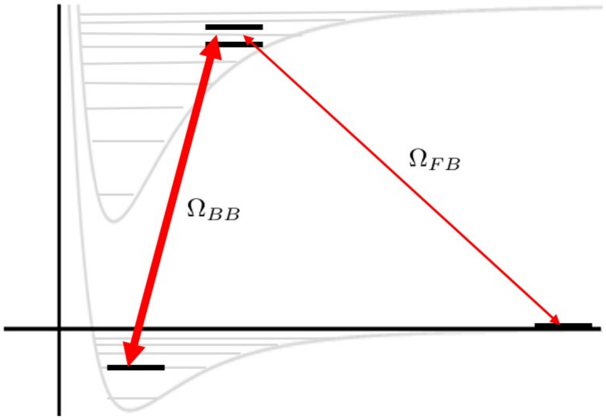

Figure 3.17: A schematic representation of the Autler-Townes splitting upon which detection in two-photon PA spectroscopy is based.

In order to implement this PA spectroscopy, we added an additional diode laser system to the creation of the PA laser beam, as shown in Figure 3.18(a). As shown in Figure 3.18(b) no changes were made to the main apparatus. The two laser beams were combined using a 50:50 beam cube so both could have the same polarization. The beam was sent through an AOM which could be used for fast switching. The -1 order out of the AOM was sent through the Li vapor cell for filtering and coupled into a PM fiber, as with our one-photon PA experiments. We used two distinct techniques to stabilize the two lasers. The FB laser (Neville Longlaser) did not need to be widely tuned as it would remain locked to a one-photon PA resonance. For this we used an offset lock, whereby the FB PA laser was locked relative to our main Li cooling laser which was itself stabilized to our atomic reference as usual. A small amount of light leaking through the isolators in the FB PA laser system was combined with a beam pickoff of our Li Zeeman slower beam and the resulting beam was fibered into our scanning Fabry Perot cavity. The signal from this scan showed two distinct peaks - one for the FB PA laser and one for the slower. We used Labview to monitor the spectral length between these two peaks. A digital PI loop then generated a feedback signal for the FB PA laser, closing the loop by connecting the output to the piezo-electric transducer (PZT) controller for the FB PA laser. The BB PA laser (Toptica DL-100), which needed to be widely tunable, was frequency stabilized using the High Finesse WS-7 wavemeter, as in our one-photon PA spectroscopies.

Detecting a bound-to-bound resonance using the AT splitting as shown in Figure 3.17 is simple in principle, but experimental success requires a careful balance of parameters. There are two considerations which are at odds. First, in order to see suppression of the one-photon PA loss, the AT splitting must be at least on the order of the one-photon PA linewidth. In order to guarantee this, one could add more power to the BB laser as the AT splitting will increase as $\Delta \sim \sqrt{I_{\mathrm{BB}}}$ (details in the following chapter). However, increasing the BB laser intensity also increases the rate of background loss from spontaneous scatter from the atomic resonance. If the background loss becomes larger than the PA loss, the one-photon signal is entirely lost, precluding the observation of a two-photon resonance. In that sense, there is a limit to the amount of BB intensity that can be used to create the AT splitting. Before proceeding with our spectroscopic search, we determined the maximum amount of BB power we could use before the background losses exceed the PA losses. Figure 3.19 shows the result of such a test. Achieving sufficient separation between the on and off resonant lifetimes in the presence of the BB laser beam restricted us to the use of relatively strong one-photon PA resonances. For that reason, all the two-photon spectroscopy work was done with the FB laser locked to either the $v* = -2$ or $v* = -7$ resonances.

3.7 Ground Bound States

Figure 3.20 shows a representative two-photon PA resonance. As with the one-photon spectroscopy, we used the LeRoy-Bernstein formula to predict the locations of the subsequent bound states. In this way we were able to observe the first six bound states in the electronic ground potential (see Figure 3.21). We were unable to observe $v = -7$, presumably because of a combination of two factors. While we did much of our two-photon PA spectroscopy with $v* = -7$ as the one-photon "intermediate" resonance required to induce the PA loss, we were unable to use this intermediate state because the expected location of $v = -7$ would put the

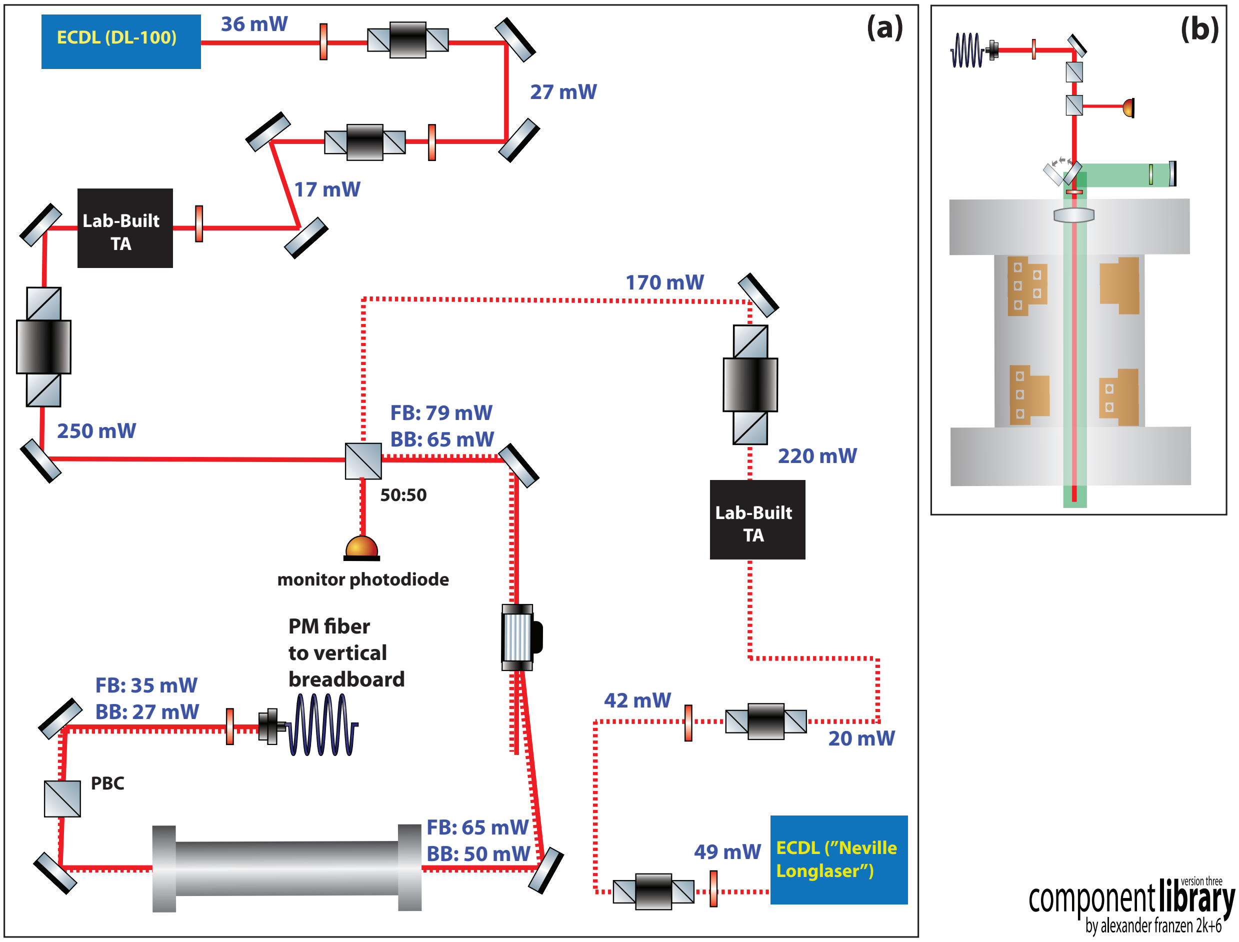

componentlibrary version three by alexander franzen 2k+6

Figure 3.18: The experimental setup for two-photon PA spectroscopy. The setup wasa similar to that for one-photon spectroscopy. An additional ECDL+TA system was used for the required second beam and the two beams were combined in a 50:50 beam cube to allow for combination with the same polarization. In (a) additional beam shaping optics are omitted and typical laser powers are indicated at various points with blue text. The setup on the main table shown in (b) is not much different from Figure 3.4 except that the feedback photodiode is now simply a monitor photodiode, owing to the complexity of feedback on the sum of two signals which may drift independently.

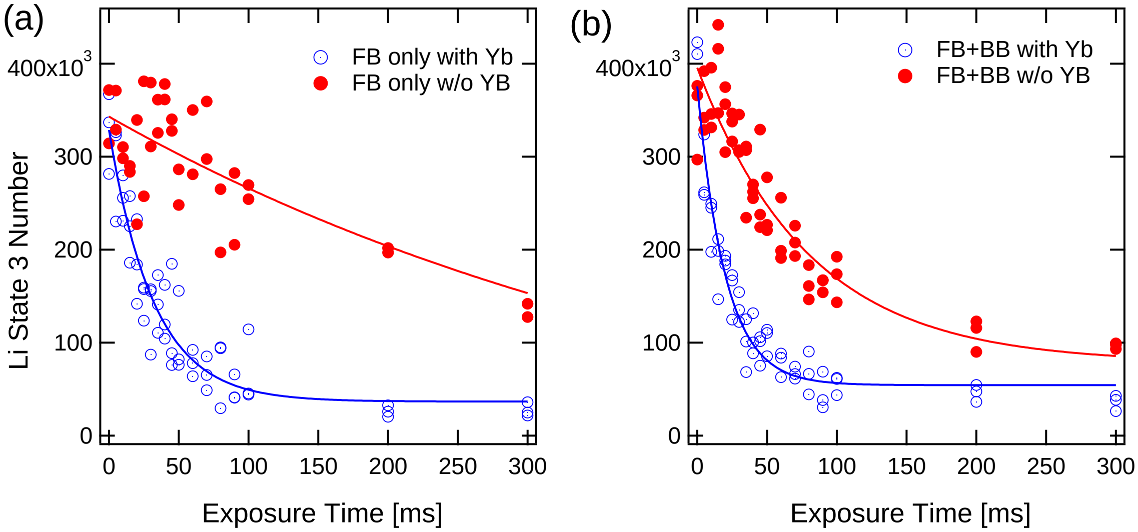

Figure 3.19: A demonstration of favorable lifetime separation on and off resonance. (a) The FB laser only was used to measure the lifetime of the atoms under the exposure to resonant PA light with (blue open circles) and without (closed red circles) Yb. (b) The lifetimes were measured with (open blue circles) and without (closed red circles) Yb but with the additional presence of the BB beam tuned away from any one- or two-photon resonances (1 GHz blue of the one-photon resonance). The FB power was 1.2 mW and the BB power, if used, was 1.0 mW.

BB laser too close to the atomic resonance to achieve sufficient lifetime separation and allow a two-photon resonance to be observed (as in Figure 3.19). The only other one-photon PA resonance with which we could achieve sufficient lifetime separation was $v* = -2$. While we attempted to observe $v = -7$ using this intermediate state, we were unsuccessful. This means that either the LeRoy-Bernstein Formula prediction failed severely and we didn't search the proper spectral range or the bound-to-bound Franck-Condon factor that ultimately limits the strength of the 2-photon signal was too small. The latter case seems more likely especially given that we had previously failed to observe any of the states $v = -4, 5, 6$ using $v* = -2$ as the intermediate.

Table 3.2 displays the binding energy of the states $v = -2$ to $v = -6$ along with the experimental parameters used in their measurement. An extensive discussion of the observation of $v = -1$ with an alternate, high precision method is discussed in the next chapter. Unlike for the one-photon spectroscopy in this thesis, we do not report on the Franck-Condon factors associated with these resonances as for each state there is a manifold of such numbers, one for each intermediate state. However, the bound-to-bound Franck-Condon factors are of central importance to work presented in the following chapter and are discussed at length there.

Moreover, unlike the excited state in which the orbital angular momentum of the Li electron plays an important role in the magnetic moment, the ground state is much simpler. Indeed the magnetic moment of the ground state should be independent of the vibrational state of the molecule. After measuring the magnetic moment in detail for $v = -1$, we also performed a two point measurement on $v = -6$, measuring the binding energy at one low field and one high field and found it was the same as that for $v = -1$.

3.8 Correction to Interspecies Scattering Length

In addition to providing crucial information on the location of bound states and the strength of the vibronic transitions which could be used for coherent association of molecules, our spectroscopy of the electronic ground state provided constraints on the long-range potential

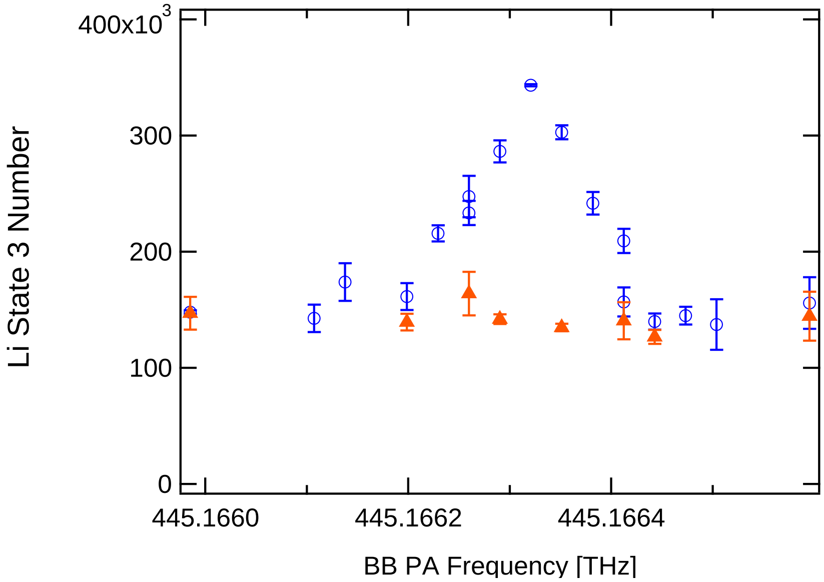

Figure 3.20: A sample two-photon PA resonance signal. Open blue circles show the remaining Li atom number in the presence of both FB and BB light as the BB frequency is changed. Closed orange triangles represent the remaining atom number with only FB light. Note that for collecting the FB only data, the BB frequency didn't need to change but repeated points are plotted against BB PA frequency to provide a background level for the FB+BB data. This is a scan of the $v = -2$ resonance. The binding energy for this state can be calculated by subtracting the frequency of the two-photon PA resonance peak from the frequency of the FB light used in this experiment: 444.13623 THz.

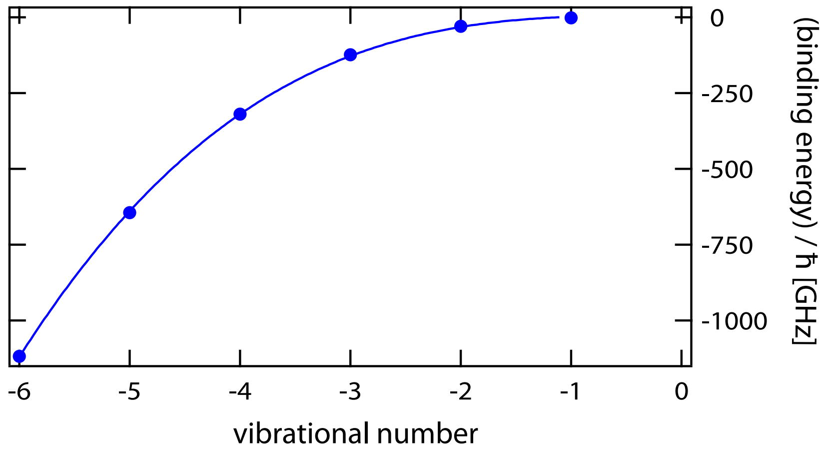

Figure 3.21: The binding energies of the near-threshold bound states of the ground molecular potential. The error bars on each point are within the symbols. A LeRoy-Bernstein fit shows good agreement with the binding energies of these loosely bound states.

vibrational number	excited state used	FB frequency	BB frequency	binding energy	power	exposure time
$-v$	$-v*$	THz	THz	GHz	(FB/BB) mW	ms
1	-	-	-	1.826	-	-
2	7	445.136265	445.1663499	30.08	9/7	100
3	7	445.136255	445.2602121	123.96	9/0.5	50
4	7	445.136255	445.4557204	319.47	9/0.5	50
5	7	445.136258	445.7807154	644.46	9/0.5	50
6	7	445.136258	446.2545534	1118.30	9/0.5	50

Table 3.2: The binding energies of the first six bound states of the ^{174}Yb^{6}Li ground state potential. This spectroscopy was performed in an 8.15 W trap with a painting amplitude of 0.5 V at a field of 100 G. Note that a precise measurement of the $v = -1$ state is discussed in Chapter 4.

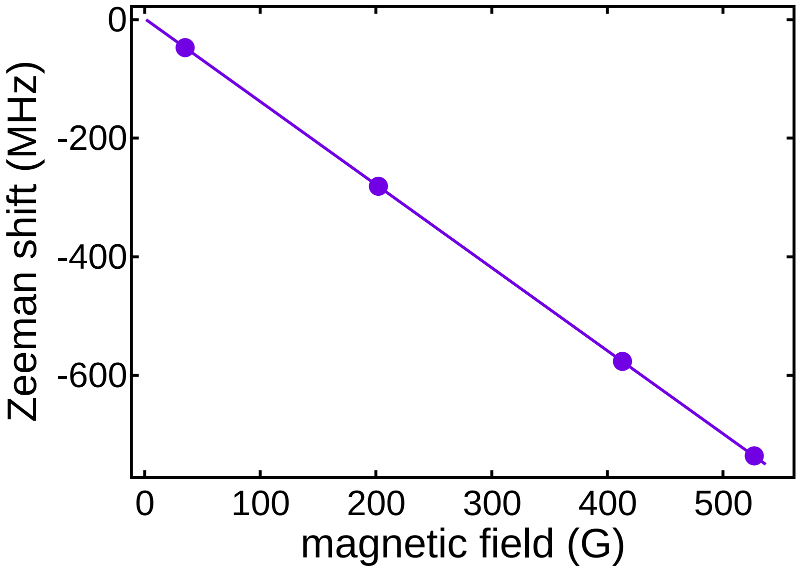

Figure 3.22: The magnetic moment of the $v = -1$ bound state is measured by repeating the two-photon loss spectroscopy at multiple fields.

between Yb and Li. As will be described in greater detail in Chapter 5, interactions between two particles at ultracold temperatures depend principally on a single parameter: the s-wave scattering length, which represents the $R = 0$ intercept of the scattering wavefunction. Assuming the interaction potential is sufficiently short ranged, the asymptotic form of the scattering wavefunction is merely a line and the intercept of this line has a strong dependence on the binding energy of the least-bound state of the potential [117].

An accurate value of the s-wave scattering length can be obtained by numerically solving the Schrödinger equation if the interatomic potential is known [118]. Our theory collaboration with the group of Svetlana Kotochigova (Temple University) allowed us to use our determination of vibrational bound states in the ^{174}Yb^{6}Li electronic ground state to produce an accurate description of the long-range potential and hence calculate the s-wave scattering length with high precision [114]. The result was 30.07 a_0. As shown in Table 3.3, this is significantly different than was previously measured using the method of interspecies ther-

Method	Reference	scattering length
interspecies thermalization	[119]	$\|a\| = 19 \pm 4$
interspecies thermalization	[101]	$\|a\| = 13 \pm 3$
PA spectroscopy	[114]	$a = 30.07$

Table 3.3: Measurements of the s-wave scattering length, $a_{\ell=0}$ for ^{174}Yb and ^{6}Li. The value is given in units of the Bohr radius, a_0. Note that measurements through interspecies thermalization actually measure the square of the scattering length and so the sign is not determined.

malization [119, 101]. However, the method of interspecies thermalization is indirect and requires accurate knowledge of the overlap density of the two atomic species in the trap and is based on the assumption that the ODT is a harmonic trap. PA spectroscopy is rather a precise probe of the fundamental scattering properties of the Yb+Li system and is not limited by systematic error from the trapping potential.

This more accurate measurement of the s-wave scattering length will be an important factor in understanding the feasibility of using a magnetic Feshbach resonance (see Chapter 5) to coherently create YbLi molecules as will be discussed in Chapter VI.

Chapter 4

ATOM-MOLELCULE COHERENCE IN ^{174}YB^{6}LI

This chapter concerns the creation of a coherent superposition state between an atomic pair state and a bound molecule. We first discuss the reasons that using PA transitions to pump atoms into a molecular state is not a feasible route to molecule production. Then we introduce the eigenstates of the atom-molecule three-state system which exhibits a 'dark' superposition state that can be manipulated to transfer atomic populations to molecular populations using two phase-coherent laser beams. We describe the method by which we observed the formation of this dark state. After describing our failed attempts to perform coherent transfer to the molecular state, we extract from our spectroscopic measurements the timescales relevant to the efficiency of the transfer process and conclude that the apparatus we used for these experiments was not suitable for association. We outline the necessary improvements under which better results can be expected.

4.1 Producing Molecules with PA Transitions

In the previous chapter we discussed photoassociation as a technique to probe the interatomic potential. This discussion overlooked the fact that photoassociation is also a technique with which to create molecules by using the ro-vibronic transitions studied in PA to transfer atoms into bound molecular states. Indeed PA as a means for molecule creation has been intensively studied both theoretically and experimentally. However, the method as described in the previous chapter generally lacks two essential properties of a useful association scheme that we now state explicitly.

- Stability: molecules must have a sufficiently long lifetime in the trap to be useful for subsequent experimentation.

- Low ro-vibrational temperature: molecules should ideally be created in just one vibrational state as many proposed studies based on ultracold molecules are premised on preparation into a single internal quantum state.

Molecules created in the excited state by one-photon PA are radiatively unstable with lifetimes similar to those of the bare atomic transition to which they correspond and are thus not suitable for subsequent experimentation. However, molecules can be formed in stable electronic states through an initial one-photon PA excitation followed by transfer to a bound state in the electronic ground state. The simplest such scheme would involve spontaneous emission into a ground bound state. However, this scheme usually fails to meet the second criterion listed above; there is no selection rule constraining the ro-vibrational states to which the molecule can decay and the result would be a mixture distributed according to the values of the various Franck-Condon factors rather than a single state. Recent theoretical work proposes to control this decay by performing one-photon PA in an optical cavity [120]. However, it should be noted that a combination of favorable Franck-Condon factors and the use of narrow electronic transitions allows for the efficient creation of a vibrationally cold sample of $^{88}Sr_2$ molecules [121] which have since been used to probe quantum chemistry [122]. This method of relying on favorable Franck-Condon factors has been studied extensively in heteronuclear systems, in particular where BB Frank-Condon factors are generally expected to be larger than for homonuclear molecules even for deeply bound, and hence more collisionally stable states [123, 124].

4.1.1 Coherent Association of Molecules with Light Fields

Preparation of a sample of ultracold atoms into a chosen quantum state can be achieved instead through coherent control of ro-vibronic transitions. The simplest imaginable coherent scheme would be a pair of π pulses: one which transfers the population into an excited molecular state, followed by a second that transfers the population down to a bound state in the electronic ground state. However, such a process is generally not possible because of the strength of the dissipation. As we saw in the last chapter, the lifetime of the excited molecular bound state is on the order of or shorter than the bare atom's electronic transition which for us is $2\pi \times 5.9$ MHz. But as we shall see later in this chapter, achievable Rabi frequencies for a typical free-to-bound ro-vibronic transition with a typical amount of laser intensity is $\sim$ 100 kHz. For this reason, coherent Rabi oscillations are rarely seen when addressing ro-vibronic transitions in ultracold molecules [125, 126].

While exploiting Rabi oscillations is not usually a feasible way to transfer population to the ground molecular state, the dissipation which prevents this can be "avoided" by incorporating the relevant states into a dressed three-state system. Before explaining the features of a three-state system which allow for coherent association of atoms into molecules, we consider why it is valid to treat a pair of atoms such as Li and Yb as a three-state system.

Figure 4.1 overlays the vibrational structure of the low-lying electronic state of a heteronculear dimer with a three-state system. We label the states in the following way:

$|a\rangle$ is the incoming scattering state

$|m\rangle$ is some ro-vibrational state in an electronically excited potential

$|g\rangle$ is some ro-vibrational state in the ground electronic potential

Since the free-to-bound ro-vibronic transitions have a linewidth $\sim$MHz but even the vibrational states are separated by $\sim$GHz or more from each other and from threshold, these transitions are well resolved. Further, while the Rabi frequencies $\Omega_{\rm FB}$ and $\Omega_{\rm BB}$, which connect states $|a\rangle - |m\rangle$ and $|m\rangle - |g\rangle$ respectively, can be controlled to some extent by changing the laser field intensity, the connection between $|a\rangle$ and $|g\rangle$ is strongly suppressed because it is only weakly dipole allowed. The strength of this $|a\rangle - |g\rangle$ connection is further reduced by extremely small Franck-Condon factors [127]. These properties of the atom-molecule system means that as long as the state $|a\rangle$ is well-defined, the system approximates the properties of a "lambda system" as it is referred to in the field of quantum optics [128, 129, 130]. Throughout this chapter, we will refer to the states as $|a\rangle\,, |m\rangle\,, |g\rangle$ and couplings $\Omega_{\rm FB}, \Omega_{\rm BB}$ as appropriate for the case of our system. However we briefly note here that the discussion

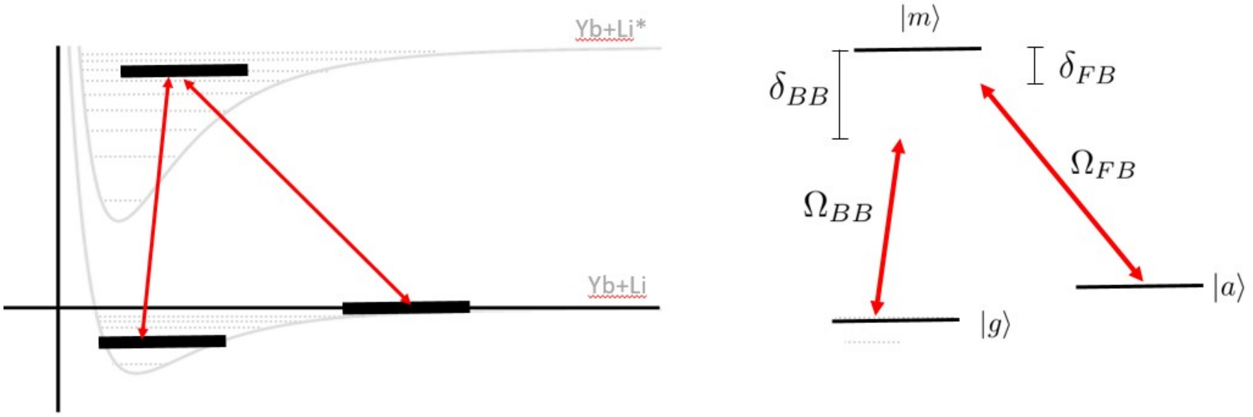

Figure 4.1: (left) The approximation of the quantum states of Yb+Li atoms as a three-state system. The scattering state and a bound state in the electronic ground state are both coupled to a bound excited state. (right) The labeling conventions used for treatment of the three-state system in this state. Ω_{FB} and Ω_{BB} are the Rabi frequencies for the free-to-bound and bound-to-bound ro-vibronic transitions respectively. δ_{FB} and δ_{BB} are the one-photon detunings of the light field from the free-to-bound and bound-to-bound PA resonances respectively (note that they are drawn with negative values in this schematic).

in the following two sections applies equally well to other three-state systems for which this labelling scheme would make little sense.

4.2 Three-state Lambda Systems

Under the rotating wave approximation, the Hamiltonian for such a system is given by the following [130].

$$H_{\mathrm{RWA}} = \hbar \begin{bmatrix} 0 & \Omega_{\mathrm{FB}}/2 & 0 \\ \Omega_{\mathrm{FB}}/2 & \delta_{\mathrm{FB}} & \Omega_{\mathrm{BB}}/2 \\ 0 & \Omega_{\mathrm{BB}}/2 & \delta_{\mathrm{FB}} - \delta_{\mathrm{BB}} \end{bmatrix} \tag{4.1}$$

Where Ω_{FB} and Ω_{BB} are the Rabi frequencies for the free-to-bound and bound-to-bound ro-vibronic transitions respectively, and δ_{FB} and δ_{BB} are the one-photon detunings of the light field from the free-to-bound and bound-to-bound PA resonances respectively. Under the conditions $\delta_{\mathrm{BB}} = \delta_{\mathrm{FB}} = 0$ the eigenstates of this system are given by the expressions below.

$$|+\rangle = \frac{\sin\theta}{\sqrt{2}}|a\rangle + \frac{1}{\sqrt{2}}|m\rangle + \frac{\cos\theta}{\sqrt{2}}|g\rangle \tag{4.2a}$$

$$|-\rangle = \frac{\sin\theta}{\sqrt{2}}|a\rangle - \frac{1}{\sqrt{2}}|m\rangle + \frac{\cos\theta}{\sqrt{2}}|g\rangle \tag{4.2b}$$

$$|0\rangle = \cos\theta\,|a\rangle - \sin\theta\,|g\rangle \tag{4.2c}$$

$$\theta = \arctan\frac{\Omega_{FB}}{\Omega_{BB}} \tag{4.2d}$$

The state designated by $|0\rangle$ is referred to as the "dark state" because it contains no projection onto $|m\rangle$, the only strongly radiative state in the system. Unlike what one might refer to as "typical" quantum interference, in which a differential phase accumulation can lead to destructive interference of probability amplitudes, a three-state system can exhibit destructive interference in the coherences, which leads to the decoupling of $|m\rangle$ from the light field.

The creation of this dark state has been studied in a variety of different physical systems such as atomic gases, quantum dots, and optical cavities [131, 132, 133, 134] where the typical experimental signature is sometimes called electromagnetically induced transparency (EIT) because for $\Omega_{\mathrm{BB}} \gg \Omega_{\mathrm{FB}}$ the absorption of the FB field is strongly suppressed over a *narrow* range of δ_{FB}, leading to transparency. Without such strict limits, the creation of the dark state may instead be interpreted as coherent population trapping (CPT) because the formation of the dark state allows for transfer into the dark state. For the purpose of this thesis, we will refer generally to the creation of the dark state as CPT.

4.2.1 Adiabatic Manipulation of the Lambda System: Stimulated Raman Adiabatic Passage

The dark state $|0\rangle$ is the key to performing population transfer from $|a\rangle$ to $|g\rangle$ while meeting the criteria outlined at the beginning of this chapter. By considering the possible values for θ in Equation 4.2, we arrive at the following two equations.

$$|0\rangle_{\theta=0} = |a\rangle \tag{4.3a}$$

$$|0\rangle_{\theta=\frac{\pi}{2}} = -\,|g\rangle \tag{4.3b}$$

We see that by changing the value of θ from 0 to $\frac{\pi}{2}$, we change the state from the atomic state to the ground molecular state, provided that the change of θ is slow enough for $|0\rangle$ to remain an eigenstate of the system. This process is given the general name of stimulated Raman adiabatic passage (StiRAP) [130]. Its application for molecule formation is referred to as free-to-bound StiRAP.

To effect the desired change in θ, the values of Ω_{BB} and Ω_{FB} may be manipulated by changing the intensities of the driving laser fields in time. For whatever temporal shape the FB and BB pulses take, in order to effect $\theta = 0 \rightarrow \frac{\pi}{2}$, the Ω_{BB} must be applied first followed by a partially time-overlapping pulse of Ω_{FB}. Since this is the reverse order compared to a pair of π pulses designed for the same objective, it is sometimes referred to as the “counterintuitive” pulse sequence.

Figures 4.2(a) and (b) show a possible StiRAP pulse sequence and the corresponding evolution of θ. In Figure 4.2(c) the population of each three-states is shown through numerically solving the Liouville equation, using H as in Equation 4.1 with the addition of a dissipation term. As an easy example, we consider the case for which $\gamma_a = 10\max(\Omega_{\mathrm{FB}}) = 10\max(\Omega_{\mathrm{BB}})$ (a case for which using π pulses is impossible). As seen in Figure 4.2, even under the condition that $\gamma_a > \Omega_{\mathrm{FB}}, \Omega_{\mathrm{BB}}$, the transfer of the population from $|a\rangle$ to $|g\rangle$ is almost 100% owing to the fact that $|m\rangle$ is barely populated through the pulse sequence.

Although this model is too crude to exactly capture the dynamics for molecule formation, the scheme has been successfully demonstrated. Free-to-bound StiRAP was used for coherent

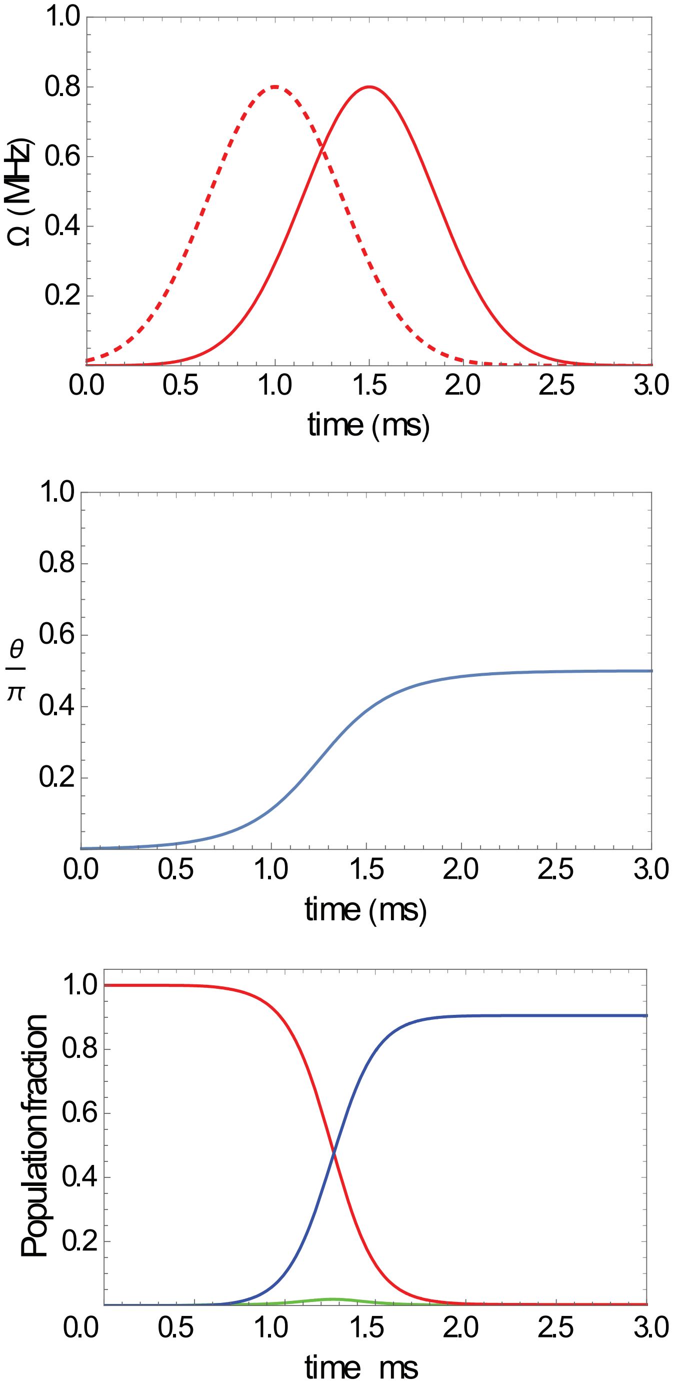

Figure 4.2: (a) A sample pair of Gaussian pulses of a strength and duration satisfying adiabaticity. (b) The time evolution of $\theta = \arctan\frac{\Omega_{FB}}{\Omega_{BB}}$ associated with the pulses in a. (c) Time evolution of the population in the in $|g\rangle$ (blue), $|a\rangle$ (red) along with the population in $|m\rangle$ multiplied by 1000(green) how the residual population of this intermediate state.

creation of Sr_2 molecules in a 3D optical lattice with formation efficiencies over 80% [80, 135]. However, to the author's best knowledge there are at this time no published accounts of successful creation of heteronuclear molecules using free-to-bound StiRAP.

4.3 Atom-molecule Coherence in Yb+Li

As a basis for molecule formation via StiRAP, we sought a coherence between $|a\rangle$ and $|g\rangle$ by addressing a pair of free-to-bound and bound-to-bound ro-vibronic transitions, connected through the same state $|m\rangle$. Although we had identified in our spectroscopy several vibrational levels of the YbLi ground state, we chose to target the $v = -1$ state for experimental simplicity. The light-driven coherence requires dressing by two laser beams which are phase coherent and separated in frequency by the binding energy of the target state in the ground potential. Since the binding energy of $v = -1$ is only 1.8 GHz, this could easily be achieved using AOMs to shift the bifurcated output of a single master laser.

Figure 4.3 shows the experimental setup for our initial studies of the atom-molecule coherence. A single ECDL was frequency locked to the wavemeter as in Chapter 3. The output of the ECDL was amplified with a lab-built tapered amplifier and split into two components. The ratio of this splitting was adjusted in order to control the ratio $\frac{\Omega_{\text{FB}}}{\Omega_{\text{BB}}}$, though a typical ratio is indicated in Figure 4.3. Each path was sent through an AOM four times using a method detailed in [136], resulting in a total frequency between the two beams of eight times the AOM frequency. The AOMs (center frequency 200 MHz) were driven by a single DDS-based frequency source (ADD9910) which was built in the lab. By independently shifting the laser frequency with the wavemeter lock and the RF frequency with the DDS source, we were able vary the values of both δ_{FB} and δ_{BB} and thereby probe the coherence. The two shifted beams were combined on a 50:50 beam cube and sent through a Li vapor cell for spectral filtering. Finally, the beam was coupled into a PM fiber. The output of the PM fiber was focused onto the atoms in the same way as discussed in Chapter 3.

We observed the formation of the "dark" coherent superposition state $|0\rangle$ through trap-loss spectroscopy [137]. A mixture of ^{174}Yb and ^{6}Li atoms were laser cooled and sequentially

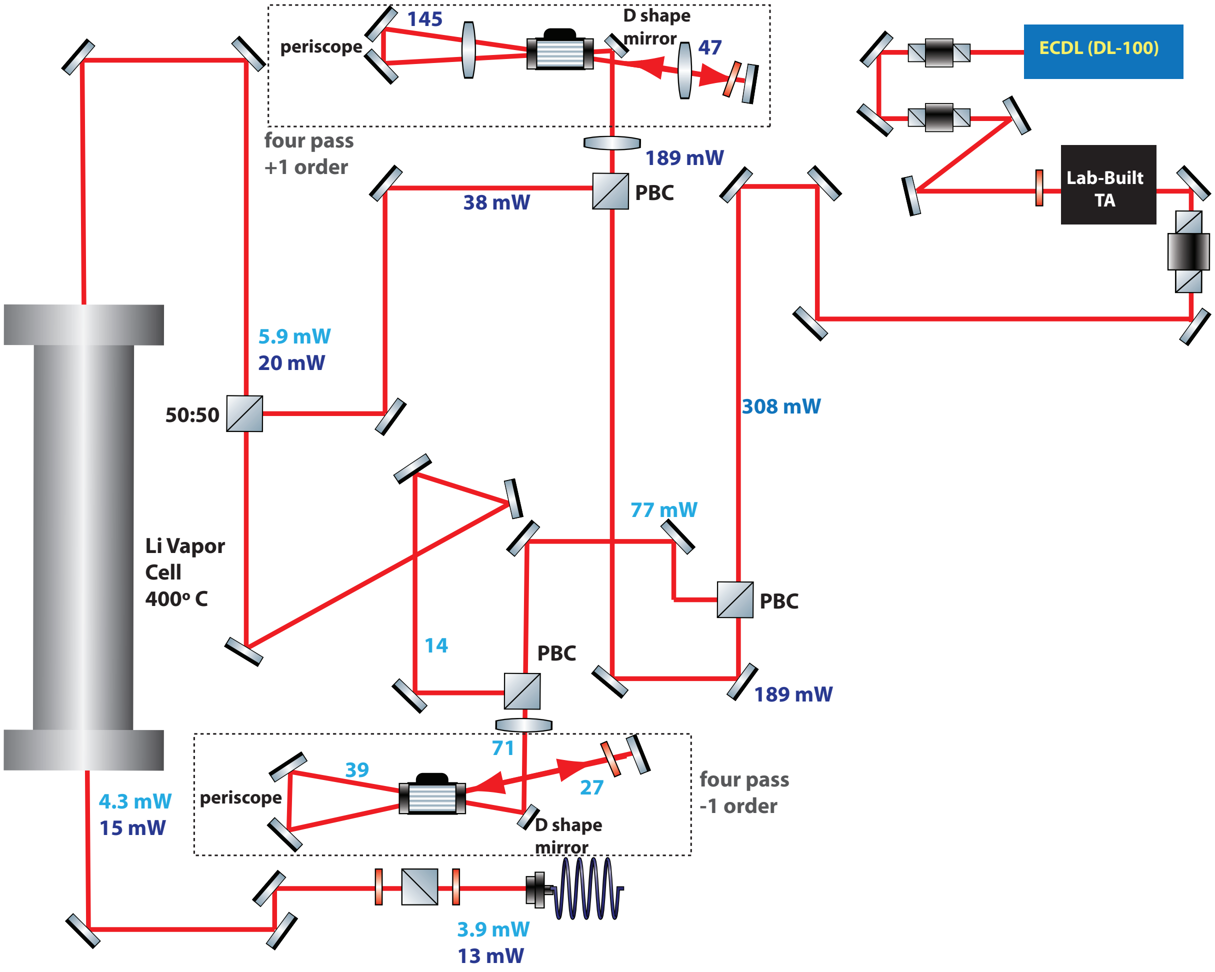

Figure 4.3: A simplified schematic of the phase-coherent two-photon PA laser system. Both the FB and BB beams are derived from the same ECDL (DL-100). Typical FB(BB) powers are shown in dark(light) blue at various points of the optical path. The output of the TA is split into two paths that are later combined on a 50:50 beam cube. Each path passes through an AOM in quadruple pass configuration. Beam shaping optics are not shown.

loaded into the ODT. After forced evaporative cooling the Li was prepared in state $|3\rangle$ through RF sweeps as described in Chapter 5. Typical starting conditions for this spectroscopy are detailed below.

Yb(Li) Number: 2.1×10^6 (3.1×10^5)
Yb(Li) Temperature: 4.8(6.1) μK
Yb Trap Frequency: $\omega = 2\pi \times \{481, 220, 135\}$ Hz
ODT Trap Parameters: $P = 3$ W, painting amplitude = 0.5 V

To perform spectroscopy we applied a simultaneous square pulse on both the FB and BB laser beams. The pulse length and the intensity of the FB beam were chosen such that absent the BB laser beam $50 - 80\%$ of the Li atoms were lost from the trap, mostly due to loss through decay of the molecular excited state. After we exposed the atomic sample to these pulses, we measured the remaining atoms in the trap through absorption imaging. We repeated this process at different values of δ_{FB}, keeping δ_{BB} constant.

Figure 4.4 is a sample spectrum obtained through trap-loss spectroscopy. The number of atoms remaining in the trap has a loss dip in a range of detunings spanning about 25 MHz as would be expected from the strong coupling of $|a\rangle$ to the lossy state $|m\rangle$ through photoassociation. However, within a narrow range of about 2.7 MHz the trap loss is strongly suppressed. This response relative to detuning takes the same form as the transmission through a medium characterized by a dressed three-state system and is likewise an indication of CPT. The creation of a spectral feature narrower than the natural linewidth of the atomic electronic transition of $\Gamma = 2\pi \times 5.9$ MHz indicates that the excited state linewidth is no longer the strongest source of decoherence in the system.

To assess the feasibility of manipulating this atom-molecule coherence for the efficient creation of molecules, we must first consider whether we can fulfill the adiabaticity requirements for StiRAP.

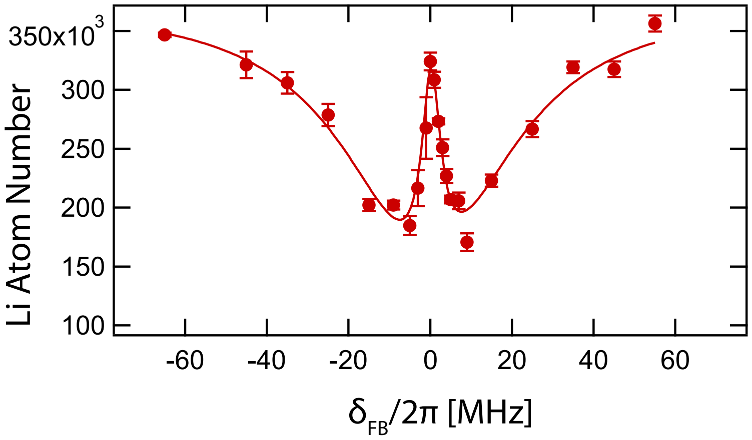

Figure 4.4: Observation of CPT in the coherent atom-molecule superposition "dark" state. For this data the pulse length was 3 ms, the FB power was 21 μW, the FB power was 419 μW and the beam waist was approximately 38 μm. A double Lorentzian fit to the data gives a width of the "CPT window" as about 2.7 MHz.

4.4 Adiabaticity and Quantifying $\Omega_{\rm FB}$ and $\Omega_{\rm BB}$

For the system to remain in the state $|0\rangle$ as the parameter θ is changed at a rate $\dot{\theta}$ the energy separation between $|0\rangle$ and the other two instantaneous eigenstates $|\pm\rangle$ must be much larger than $\dot{\theta}$.

$$\hbar\dot{\theta} \ll |E_0 - E_\pm| \tag{4.4}$$

The separation is given by the following equation [138].

$$E_0 - E_\pm = \pm\frac{\hbar}{2}\sqrt{\Omega_{\rm FB}^2 + \Omega_{\rm BB}^2} \equiv \pm\frac{\hbar}{2}\Omega_{\rm eff} \tag{4.5}$$

Using Equations 4.2(d) and 4.5, we rewrite Equation 4.4 in terms of the Rabi frequencies.

$$\left|\frac{\dot{\Omega}_{\rm FB}\Omega_{\rm BB} - \Omega_{\rm FB}\dot{\Omega}_{\rm BB}}{\Omega_{\rm BB}^2 + \Omega_{\rm FB}^2}\right| \ll \Omega_{\rm eff} \tag{4.6}$$

From the above equation we can intuit that the FB and BB pulses should change at about the same rate and have approximately the same value at their peak i.e. we should be able to robustly produce both the condition $\frac{\Omega_{\text{FB}}}{\Omega_{\text{BB}}} \ll 1$ and $\frac{\Omega_{\text{FB}}}{\Omega_{\text{BB}}} \gg 1$. Assuming the pulses are indeed smooth, we may integrate both sides of (4.4) over all time and use (4.5) to find the following general constraint.

$$\frac{\pi}{2} \ll \frac{1}{2}\int_{-\infty}^{+\infty} \Omega_{\text{eff}} dt \sim \max(\Omega_{\text{FB}}, \Omega_{\text{BB}})T \tag{4.7}$$

where T is the width of the two pulses. From this we see that the adiabaticity is approximately limited by the maximum achievable value of both the free-to-bound and bound-to-bound Rabi frequencies, given that additional contributions to decoherence (discussed later) will impose a limit on T.

We first consider the values of Ω_{FB} that can be achieved under feasible experimental conditions. The maximum magnitude of Ω_{FB} can be increased by increasing either the atomic density, n or the intensity of the FB laser, I_{FB}. This is given by the proportionality $\Omega_{\text{FB}} \propto \sqrt{n\, I_{\text{FB}}}$ [80]. To quantify the magnitude of Ω_{FB}, we analyze lifetime measurements as seen in Chapter 3, exposing the atomic mixture only to FB light. We fit these lifetime measurements to the following functional form [139].

$$N_{\text{Li}}(t) = N_{\text{Li}}(0)e^{-\frac{\Omega_{\text{FB}}^2}{\gamma_m}t} \tag{4.8}$$

Where γ_m is the natural linewidth of the PA transition, which we take to be equal to the minimum observed linewidth in our one-photon PA experiments.

To quantify Ω_{BB}, we performed Autler-Townes spectroscopy. As was mentioned in Chapter 3, Autler-Townes splitting arises in our system when the strong coupling caused by a bound-to-bound PA resonance mixes the electronic excited and electronic ground molecular states, splitting the excited state into two states that can be probed with one-photon PA. The splitting between these two states is given by the following equation [140].

$$\Delta_{\text{AT}} = \sqrt{\delta_{\text{BB}}^2 + \Omega_{\text{BB}}^2} \tag{4.9}$$

With this in mind, we performed multiple measurements of the Autler Townes splitting, with a fixed frequency on the BB laser. By repeating this for several BB laser frequencies

ground state	excited state	Ω_{BB}	Ω_{FB}
$\lvert g\rangle$	$\lvert m\rangle$	$\sqrt{\frac{I_{\text{BB}}}{W/cm^2}}$	$\sqrt{\frac{I_{\text{BB}}}{W/cm^2}}\sqrt{\frac{n}{cm^{-3}}}$
$v = -1$	$v* = -2$	$2\pi \times 25.3$ MHz	$2\pi \times 6.9$ kHz

Table 4.1: The scaled Rabi frequencies for the candidate three-state system for the YbLi molecules. The value of Ω_{BB} was measured once and scaled based on the intensity of the BB laser beam used for that measurement. The value of Ω_{FB} was measured once and scaled based on the intensity of the FB laser beam used and the interspecies overlap density of the atomic sample used in the measurement.

we were able to determine both the frequency for which $\delta_{\text{BB}} = 0$ and the value of Ω_{BB} (see Figure 4.5). Using the proportionality $\Omega_{\text{BB}} \propto \sqrt{I_{\text{BB}}}$, we may determine the value of the Rabi frequency for any laser power. However, since Ω_{BB} also depends on the bound-to-bound Franck-Condon factor, this procedure must be done individually for each BB transition of interest.

Through these two types of measurements, we calculated the Rabi frequencies available in our system for the most favorable case. The value of Ω_{BB} has been scaled for the intensity used and the value of Ω_{FB} has been scaled for both the intensity and the approximate overlap density n. Note that because the overlap density is often lower than our estimates, the value of Ω_{FB} reported here is more likely to be an underestimate. The results are shown in Table 4.1. The extreme disparity between the values of Ω_{BB} and Ω_{FB} indicate that the relative intensity of the two laser beams must be carefully controlled for StiRAP to be efficient.

4.5 Two Regimes for the Three-state System

Based on the framework discussed in the previous section, one might think that the adiabaticity requirements could be met simply by increasing the time of the StiRAP pulses. However, while the lifetime of the excited state $\lvert m\rangle$ can be effectively ignored in StiRAP, other sources of decoherence limit the time of this pulse. In this section we will first demon-

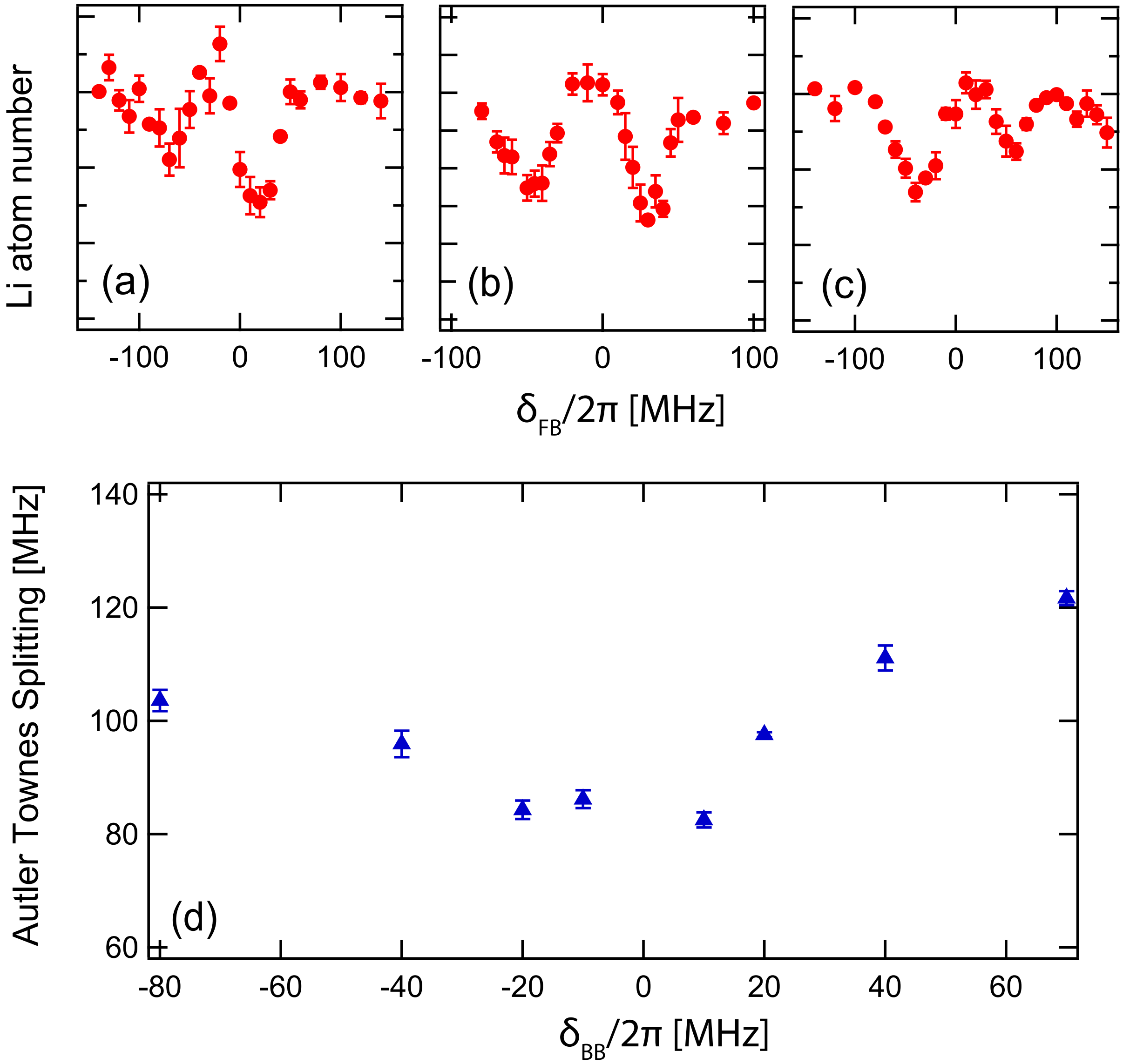

Figure 4.5: Autler-Townes splitting at multiple detunings from the BB resonance for states $v = -1$ and $v* = -2$. For (a) , Ω_{BB} is about $2\pi \times 80$ MHz, for (b) $\delta_{\mathrm{BB}} \approx 0$ MHz and for (c) $\delta_{\mathrm{BB}} \approx -40$ MHz. (d) shows the change in the Autler Townes splitting for various BB detunings. For this intensity of the PA laser, $\delta_{\mathrm{BB}} \approx +40$ MHz.

strate that the excited state lifetime is not a relevant source of decoherence. In Section 4.7 we will consider alternate sources of decoherence.

To understand the robustness of the dark state to the presence of dissipation in the excited state, we must first note that the signature effect of the dark state - coherent population trapping - arises in the low Ω_{BB} limit of Autler-Townes splitting (ATS). Though, we note briefly that while CPT requires phase-coherent driving fields, ATS can be seen with or without a fixed relative phase between the fields.

To determine which regime we are working with in our system, we consider the cutoff between weak and strong coupling of the BB transition [141, 142]. Assuming only the excited state contributes to the dissipation, we need to understand the coherence term between the excited molecular state and the atomic state. This matrix element, probed through our spectroscopy, is given by the following equation.

$$\rho_{a,m} = \frac{\Omega_{\mathrm{FB}}\Delta}{\Delta\left(\Delta - i\gamma_m\right) - \left(\frac{\Omega_{\mathrm{BB}}}{2}\right)^2} \tag{4.10}$$

Where we have taken $\Delta = \delta_{\mathrm{FB}} - \delta_{\mathrm{BB}}$. Equation 4.10 can be rewritten to more clearly illustrate the difference between the weak and strong coupling regimes.

$$\rho_{a,m} = \eta\left[\frac{\Delta_- - \Delta_0}{\Delta - \Delta_+} + \frac{\Delta_0 - \Delta_+}{\Delta - \Delta_-}\right] \tag{4.11a}$$

$$\Delta_0 = i\gamma_m \tag{4.11b}$$

$$\Delta_\pm = i\frac{\gamma_m}{2} \pm \sqrt{\left(\frac{\Omega_{\mathrm{BB}}}{2}\right)^2 - \left(\frac{\gamma_m}{2}\right)^2} \tag{4.11c}$$

$$\eta = -\frac{\Omega_{\mathrm{FB}}}{2\sqrt{\left(\frac{\Omega_{\mathrm{BB}}}{2}\right)^2 - \left(\frac{\gamma_m}{2}\right)^2}} \tag{4.11d}$$

Where we have taken $\delta_{\mathrm{BB}} = 0$ for simplicity.

Strong Coupling Regime In the strong coupling regime $\Omega_{\mathrm{BB}} \gg \gamma_m$ such that $\eta \rightarrow \frac{-2\Omega_{\mathrm{FB}}}{\Omega_{\mathrm{BB}}}$ and $\Delta_\pm \rightarrow \frac{i\gamma_m}{2} \pm \Omega_{\mathrm{BB}}$. The resulting expression for $\rho_{a,m}$ is below.

$$\rho_{a,m} \propto \eta\left[\frac{-\frac{i\gamma_m}{2} - \frac{\Omega_{\mathrm{BB}}}{2}}{(\Delta - \frac{\Omega_{\mathrm{BB}}}{2}) - \frac{i\gamma_m}{2}} + \frac{\frac{i\gamma_m}{2} - \frac{\Omega_{\mathrm{BB}}}{2}}{(\Delta + \frac{\Omega_{\mathrm{BB}}}{2}) - \frac{i\gamma_m}{2}}\right] \tag{4.12}$$

And this simplifies to the following equation in the $\Omega_{\mathrm{BB}} \gg \gamma_m$ limit.

$$\rho_{a,m} \propto \Omega_{\mathrm{FB}} \left[\frac{1}{(\Delta - \frac{\Omega_{\mathrm{BB}}}{2}) - \frac{i\gamma_m}{2}} + \frac{1}{(\Delta + \frac{\Omega_{\mathrm{BB}}}{2}) - \frac{i\gamma_m}{2}} \right] \tag{4.13}$$

To understand the absorption of the light field and therefore the loss of atoms from the trap, we take the imaginary portion of equation 4.13.

$$-\Omega_{\mathrm{FB}} \left[\frac{\frac{\gamma_m}{2}}{(\Delta - \frac{\Omega_{\mathrm{BB}}}{2})^2 + \left(\frac{\gamma_m}{2}\right)^2} + \frac{\frac{\gamma_m}{2}}{(\Delta + \frac{\Omega_{\mathrm{BB}}}{2})^2 + \left(\frac{\gamma_m}{2}\right)^2} \right] \tag{4.14}$$

This reproduces the Autler-Townes splitting profile: two inverted Lorentzians separated by Ω_{BB}. To verify that for high values of Ω_{BB} we observe Autler-Townes splitting, we fit this functional form to CPT spectra collected for various values of I_{BB}. As seen in Figure 4.6 the purple fit function correspond to a pair of inverted Lorentzians and fits well to the data with the highest value of Ω_{BB}, Figure 4.6(a).

Weak Coupling Regime In the opposite regime $\Omega_{\mathrm{BB}} \ll \gamma_m$ such that $\eta \to \frac{i\Omega_{\mathrm{FB}}}{\gamma_m}$ and $\Delta_{\pm} \to \frac{i\gamma_m}{2} \pm \frac{i\gamma_m}{2}\left[1 - \left(\frac{\Omega_{\mathrm{BB}}}{\gamma_m}\right)^2\right]$. Here, we consider a higher order in the quantity $\frac{\Omega_{\mathrm{BB}}}{\gamma_m}$ to prevent the value of Δ_{-} from vanishing. The result for $\rho_{a,m}$ is below.

$$\rho_{a,m} = \eta \left[\frac{i\frac{\Omega_{\mathrm{BB}}^2}{2\gamma_m} - i\gamma}{\Delta - i\gamma_m} + \frac{i\frac{\Omega_{\mathrm{BB}}^2}{2\gamma_m}}{\Delta - i\frac{\Omega_{\mathrm{BB}}^2}{2\gamma_m}} \right] \tag{4.15}$$

And this simplifies to the following equation in the $\Omega_{\mathrm{BB}} \ll \gamma_m$ limit.

$$\rho_{a,m} = \Omega_{\mathrm{FB}} \left[\frac{1}{\Delta - i\gamma_m} + \frac{-(\frac{\Omega_{\mathrm{BB}}}{2\gamma_m})^2}{\Delta - i\frac{\Omega_{\mathrm{BB}}^2}{2\gamma_m}} \right] \tag{4.16}$$

Again taking the imaginary part of $\rho_{a,m}$ we find the functional form of the loss from trap in the weak coupling limit.

$$\Omega_{\mathrm{FB}} \left[\frac{-\gamma_m}{\Delta^2 + \gamma_m^2} + \left(\frac{\Omega_{\mathrm{BB}}}{2\gamma_m}\right)^2 \frac{\frac{\Omega_{\mathrm{BB}}^2}{2\gamma_m}}{\Delta^2 + (\frac{\Omega_{\mathrm{BB}}^2}{2\gamma_m})^2} \right] \tag{4.17}$$

As in the case of strong coupling, this produces two peaks but they are not both inverted. Rather there is one inverted Lorentzian that mimics the one-photon PA transition along with a narrower Lorentzian (because $\Omega_{\mathrm{BB}} \ll \gamma_m$) that is peaked at the same value of Δ but is not inverted. This is the characteristic CPT profile. We confirm that we are able to experimentally reach this regime at low values of Ω_{BB} by fitting the data in Figure 4.6 with yellow curves. The agreement of this fit with the data in Figure 4.6(c) confirms that we are in the weak coupling regime for our lowest Ω_{BB} values.

To make the comparison between the two regimes more distinct, we note that upon taking the Fourier transform, the two limits exhibit different behavior in the time domain [142].

$$\mathcal{F}\left[Im\left(\rho_{a,m}\right)\right] = -\Omega_{\mathrm{FB}} e^{-\gamma_m t} \cos\left(\Omega_{\mathrm{BB}} t\right) \quad \text{for strong coupling} \tag{4.18a}$$

$$\mathcal{F}\left[Im\left(\rho_{a,m}\right)\right] = e^{-\gamma_m t} + \left(\frac{\Omega_{\mathrm{BB}}}{2\gamma_m}\right)^2 e^{-\frac{\Omega_{\mathrm{BB}}^2}{2\gamma_m}} t \quad \text{for weak coupling} \tag{4.18b}$$

In order to better visualize our ability to work in the weak coupling regime, we performed a discrete Fourier transform on the spectra in Figure 4.6. As seen in Figure 4.6(c), the time dynamics mostly consist of an exponential decay with very little oscillatory component, indicating that we are in the weak coupling regime. The physical intuition behind this decay behavior is that $|m\rangle$ is decaying too rapidly to be efficiently populated - even virtually - by Ω_{BB}. Alternately, one could interpret this as the two states of the Autler-Townes doublet becoming degenerate, approximating the closely spaced levels of a continuum and thus mimicking a Fano resonance.

4.6 StiRAP Attempts in ODT

After observing evidence of the creation of coherent atom-molecule superposition in the YbLi system, we chose to attempt temporal control of that state to execute StiRAP. We performed these attempts in the same trap for which the CPT spectra were collected. We searched for evidence of efficient transfer to the molecular ground state $v = -1$ by relying on the reversibility of the StiRAP process. The general procedure is:

1. use a pair of delayed Gaussian pulses with the FB pulse following the BB pulse which would transfer the atoms from state $|a\rangle$ to $|g\rangle$ provided sufficient adiabaticity and

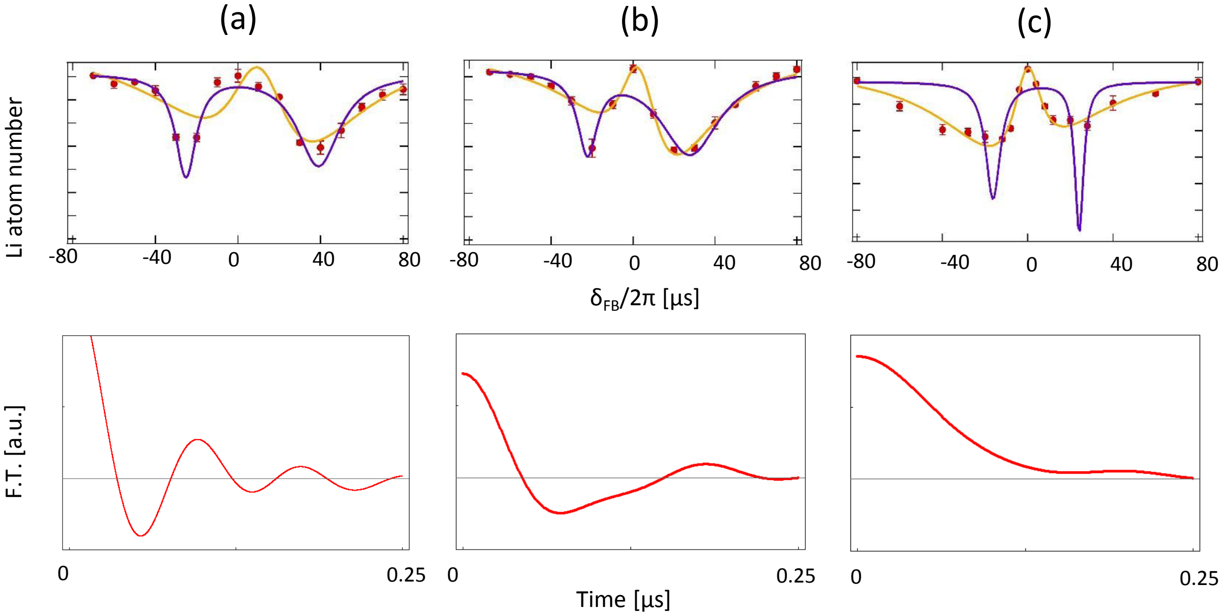

Figure 4.6: Dark state spectroscopy in three regimes. For each regime, the data is presented with filled red circles on the upper plot. Two fits are done to each set of data. The purple fit corresponds to the functional form in Equation 4.14 while the yellow fit corresponds to the functional form in Equation 4.17. The red curve in the lower panel represents a discrete Fourier transform of the experimental data. (a) The high coupling or ATS regime with $I_{\mathrm{BB}} = 300\,\mu\mathrm{W}$, (b) The intermediate regime with $I_{\mathrm{BB}} = 150\,\mu\mathrm{W}$, and (c) The low coupling or CPT regime with $I_{\mathrm{BB}} = 30\,\mu\mathrm{W}$.

coherence

2. remove all unassociated atoms from the trap using a laser pulse resonant with the atomic transitions ${}^2S_{1/2} \rightarrow {}^2P_{3/2}$ for Li and ${}^1S_0 \rightarrow {}^1P_1$ for Yb
3. use a pair of Gaussian pulses with the BB pulse following the FB pulse to transfer any molecules in state $|g\rangle$ back to $|a\rangle$
4. count the atoms remaining through absorption imaging

Knowing that we would be limited by the low values of Ω_{FB} in the existing coherent two-photon spectroscopy setup, we made a relatively simple upgrade to the setup shown in Figure 4.3 in order to boost the power in the FB laser beam. After passing through the 4-pass AOM used to shift the FB laser beam, the beam was not coupled through a fiber to the atoms but rather coupled into a free-running diode laser mount for injection locking. The output of this beam was sent to a lab-built tapered amplifier to produce the FB laser beam, still phase coherent with the BB beam. In this way we were able to produce about 20 mW of FB light and 5 mW of BB light as measured just before the beam was focused on the atoms. Before attempting StiRAP we also sought to increase Ω_{FB} by narrowing the PA beam waist to 38 μm.

We also sought to make the removal of unassociated atoms as fast as possible such that any population of molecules formed during the initial StiRAP did not fully decay before they could be transferred back to $|a\rangle$ for detection. Since the same beam used for absorption imaging was used to remove unassociated atoms, we began controlling the intensity in each of these beams through the RF power to the AOMs used to produce these beams. This control boosted the imaging power during the removal pulse such that a pulse of 5 μs would remove all the atoms.

We repeated the attempts to confirm successful StiRAP using the procedure above, always using the maximum amount of FB power available. We varied the BB power over several orders of magnitude and tried a variety of different pulse times. We also varied the time between pulses. Additionally, we tried using both $v* = -2$ and $v* = -7$ as the intermediate state. This could have been a critical decision as the maximum amount of FB power which we could use for $v* = -2$ was limited by the proximity of the Li_2 PA lines (see Chapter 3) which would power broaden and merge with the YbLi resonance, making the $v* = -2$ resonance unusable for StiRAP. However, the FB Franck-Condon factor for $v* = -7$ being so much smaller than $v* = -2$ meant that even if we used more power, the achievable Rabi frequency in either case was about the same: $\Omega_{\mathrm{FB}} \approx 2\pi \times 200$ kHz. Despite our various attempts we were unable to observe any formation of molecules via a free-to-bound StiRAP process.

4.7 Numerical Model for Three-state System

To understand the possible reasons for our failure to transfer atoms into molecules via StiRAP, we performed numerical modeling of an ideal three-state system under the condition that all three-states $|a\rangle, |m\rangle, |g\rangle$ could decay and be lost from the system at rates $\gamma_a, \gamma_b, \gamma_g$. We add this dissipation to Equation 4.1 to get the following Hamiltonian.

$$H = \hbar \begin{bmatrix} -i\gamma_a & {}^{\Omega_{\mathrm{FB}}}\!/_2 & 0 \\ {}^{\Omega_{\mathrm{FB}}}\!/_2 & -i\gamma_m + \delta_{\mathrm{FB}} - \delta_{\mathrm{BB}} & {}^{\Omega_{\mathrm{BB}}}\!/_2 \\ 0 & {}^{\Omega_{\mathrm{BB}}}\!/_2 & -i\gamma_g + \delta_{\mathrm{FB}} \end{bmatrix} \tag{4.19}$$

In the following three subsections we will discuss how we determined appropriate values to input into this model by analyzing dark state spectroscopy measurements.

4.7.1 Determining Ω_{FB} and Ω_{BB}

Ω_{FB} and Ω_{BB} were chosen according to the values in Table 4.1, although in practice we assumed that Ω_{BB} could be set to essentially any relevant value. Since we set both beams to resonance, δ_{FB} and δ_{FB} are assumed to be zero as $I_{\mathrm{FB}}, I_{\mathrm{BB}} \to 0$. Though a Stark shift on each state is added according to experimental measurements of the dark state shift with increasing intensity. Since under typical conditions $I_{\mathrm{FB}} \gg I_{\mathrm{BB}}$, we only consider shifts from the FB laser.

4.7.2 Determining γ_a

We assume that γ_a is given by the loss of atoms from the trap from spontaneous scatter off the atomic transition, which we measure through off-resonant lifetimes. Critically, γ_a will increase with intensity, limiting the beneficial effects of using more intensity to increase Ω_{FB}.

4.7.3 Determining γ_g

As was demonstrated experimentally in [137], the linewidth of the CPT curve is limited by the decay of the ground molecular state, γ_g, in the limit of vanishing Ω_{BB} according to the equation below.

$$\Delta_{\mathrm{CPT}} = \frac{\Omega_{\mathrm{BB}}^2}{\gamma_m} + \gamma_g \tag{4.20}$$

To quantify γ_g we performed several measurements of the CPT linewidth for different values of Ω_{BB}, shown in Figure 4.7. We extrapolated these results to $\Omega_{\mathrm{BB}} = 0$ to find a value of γ_g under the three-state model. We obtained a value of $\gamma_g \approx 2\pi \times 300$ kHz. The physical cause of γ_g is unknown however it is expected that these highly vibrationally excited molecules exhibit significant inelastic loss both with each other as well as with atoms in the trap which are not associated into molecules. If this is the case, we could expect a sharp reduction of γ_g if the Yb and Li atoms are loaded pairwise into individual sites of a deep optical lattice.

4.7.4 Results of Numerical Modeling

Under the condition that all the atoms begin in the atomic state $|a\rangle$ we numerically solved the Liouville equation for Gaussian pulses [143].

$$\dot{\rho} = -\frac{i}{\hbar}[H, \rho] \tag{4.21}$$

where H is given by Equation 4.19. The results of this calculation are shown in Figure 4.8(a). Consistent with our experimental observation, no population is transferred to the ground

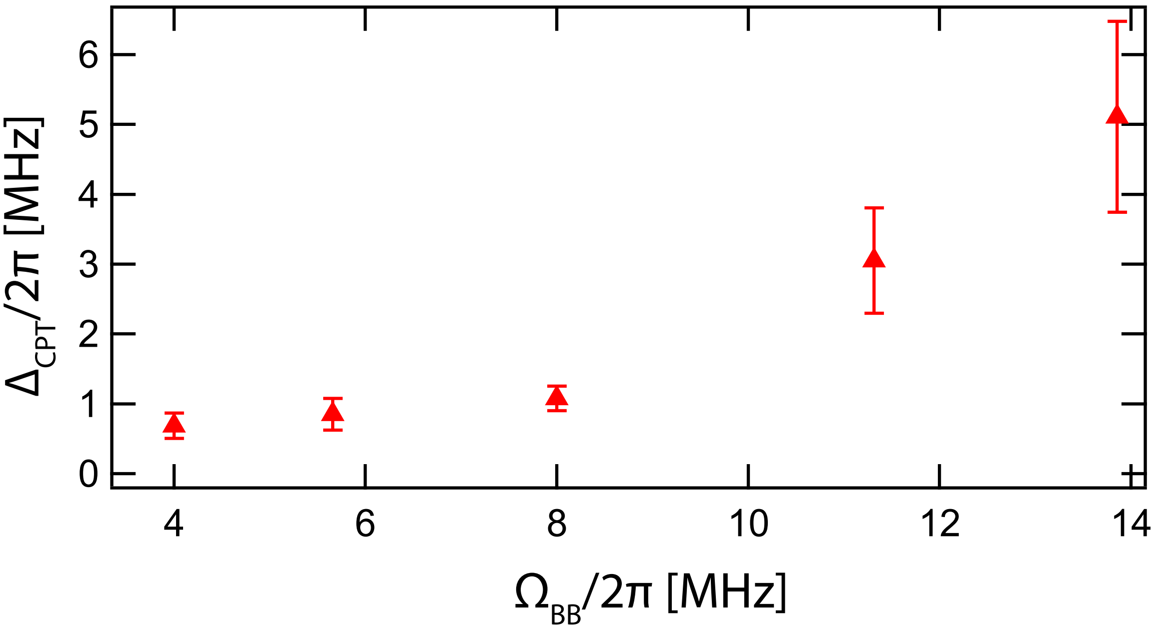

Figure 4.7: The linewidth of the inner CPT curve peak measured for different values of $\Omega_{\rm BB}$. The values of $\Omega_{\rm BB}$ are scaled for the intensity used based on a measurement of the Autler-Townes splitting at a fixed power. The error bars give the fit errors which become large as the system approaches the ATS regime. These CPT spectra were taken with $v* = -7$ as the intermediate state.

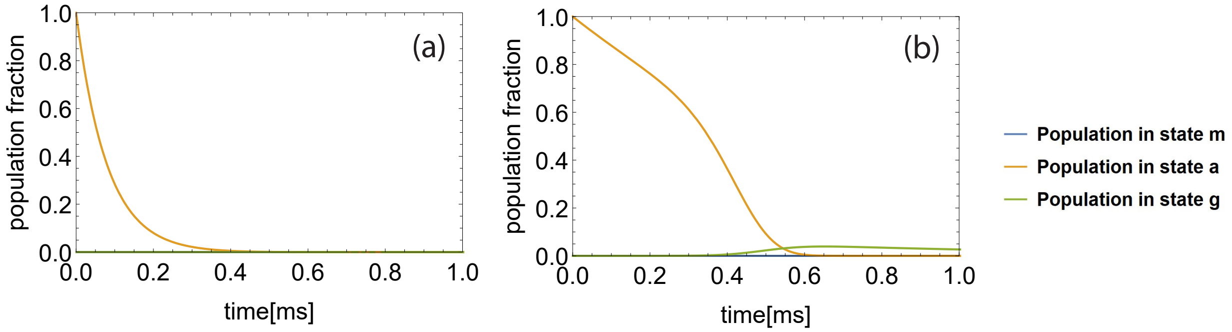

Figure 4.8: Numerical modeling of StiRAP in our system. The population in $|a\rangle$ is shown in yellow while the population in state $|g\rangle$ is shown in green. The population in $|m\rangle$ is not large enough to be visible on this scale. In both cases, Gaussian pulse of 200 μs are used separated from each other by 800 μs. (a) a realistic model based on experimentally measured parameters as described in the text. (b) a more optimistic model that may be achievable in an optical lattice as described in the text.

state $|g\rangle$. Analysis of this model indicated that the magnitude of both γ_a and γ_g were limiting factors. In order to assess a more favorable but still perhaps realistic situation, we considered the potential effects of attempting this in an optical lattice instead. Here, we would expect γ_g to be strongly suppressed if the atomic sample is prepared with one pair of atoms on each lattice site and the tuneling rate is low. Additionally, we expect the atomic density n to be considerably higher. With higher n we can achieve higher values of Ω_{FB} with the same amount or less power. We repeated the numerical model under the following conditions: $\gamma_a = 2\pi \times 0.1$ kHz, $\gamma_g = 2\pi \times 0.1$ kHz, $\Omega_{\mathrm{FB}} = 2\pi \times 400$ kHz, $\Omega_{\mathrm{BB}} = 2\pi \times 400$ kHz. As shown in Figure 4.8(b), these conditions hold more promise for producing a sample of ultracold molecules that could be detected.

4.8 Isotope Shift Measurements

We utilized the phase-coherent laser system in order to perform an isotope shift measurement of the YbLi $v = -1$ bound state. Isotope shift measurements provide a constraint on the short range portion of the interatomic potential. A sufficiently precise measurement would allow us to determine the number of bound states supported by the potential, predicting the full spectrum. Such a measurement was relatively easy to perform by switching the isotope of Yb which, unlike the Li isotope, can be changed without a major overhaul of the laser system. However, owing to the extreme mass imbalance between Li and Yb, changing the Yb isotope only changes the reduced mass by $\sim 0.1\%$, making the spectroscopic shifts too small to discern using regular two-photon PA. In contrast, the precision afforded by the relatively narrow linewidth of the CPT curve is sufficiently high [144].

An example isotope shift measurement is shown in Figure 4.9 where we perform dark state spectroscopy of YbLi $v = -1$ bound state in a sample containing either ^{172}Yb or ^{174}Yb. By performing Gaussian fits to the CPT window we determine the binding energy of each isotope. We measured the isotope shift between ^{172}Yb^{6}Li and ^{176}Yb^{6}Li to be 80.6 MHz with a statistical uncertainty of 0.3 MHz. However, we observed systematic shifts of about 0.5 MHz in repeated measurements, which ultimately prevented us from using the isotope shift measurements to constrain the number of bound states supported by the interatomic potential. We speculated that these systematic errors may be Stark shifts from fluctuations in the beam intensity, particular from physical drifts of the beam alignment optics.

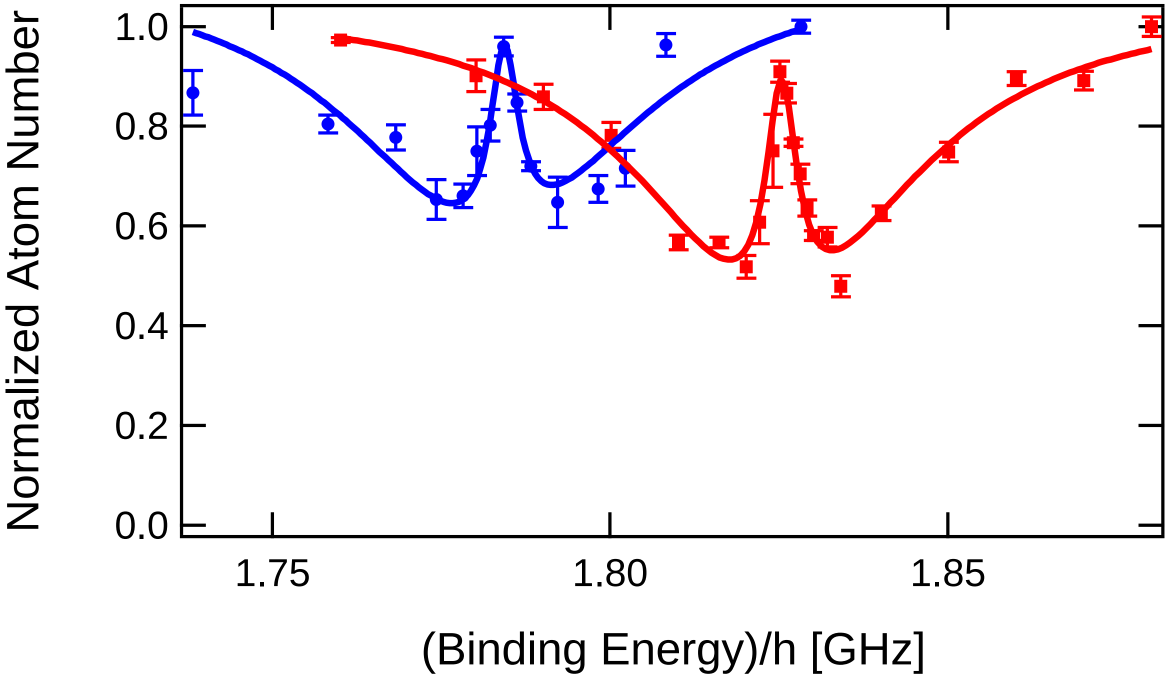

Figure 4.9: We repeated our dark state spectroscopy using a sample of ^{172}Yb (blue filled circles) to compare to our usual measurements with ^{174}Yb. The narrow linewidth in the CPT signal allows for the isotope shift to be determined with a statistical uncertainty that is about 10 times lower than in typical two-photon PA spectroscopy.

Chapter 5

MAGNETIC FESHBACH RESONANCES IN ^{173}YB^{6}LI

This chapter concerns the first observation of magnetic Feshbach resonances (MFR) in YbLi. In the previous chapter we discussed StiRAP as the first of two possible methods for coherent formation of YbLi molecules. Magnetic Feshbach resonances represent the second possible method. As we shall see, the observation of MFRs in YbLi was made possible by our knowledge of the YbLi molecule's vibrational spectrum, obtained in Chapter 3. The first section of this chapter explains the origin of scattering resonances such as MFRs. Because MFRs are considerably different than the resonances discussed in previous chapters, we will also contextualize the importance of MFRs by discussing the ways in which these resonances have enabled the study of ultracold gases to gain insight into key elements of few- and many-body physics. Next, we discuss the unique challenges and benefits for observing MFRs in YbLi. Finally, we present and analyze our observation of MFRs in YbLi after a description of the experimental technique.

5.1 Scattering Resonances

Ultracold atoms provide a unique setting in which to study quantum scattering (i.e. scattering for which semiclassical approximations will fail) [145]. This is a consequence of multiple properties of these gases:

- Their low densities mean that scattering is dominated by two-body events.

- For neutral atoms, their interaction is usually short ranged and isotropic, allowing for a central potential model for the interaction between two atoms.

- Their low temperature leads to low scattering energies, approximately limiting collisions to s-wave (head on) collisions. Notably, when s-wave collisions are not allowed, residual p-wave collisions dominate.

All these factors combined make ultracold atoms the simplest experimental platform with which to study scattering as it is presented in any introductory quantum mechanics textbook. In this section, we will briefly consider the nature of two-body scattering and from there discuss the origin of scattering resonances. Then we will discuss the key feature that distinguishes magnetic Feshbach resonances from scattering resonances in general.

We work in the center-of-mass frame where two-particle scattering can be formulated as a single particle scattering off a central potential $V\left(\vec{R}\right) = V(R)$, parameterized by $\vec{R} = \vec{r_1} - \vec{r_2}$, the interparticle separation vector between atoms 1 and 2 and $\vec{k} = \vec{k_1} - \vec{k_2}$, the relative scattering wave vector. In this formalism, the particle is considered to approach the finite-ranged central potential from infinity. Without loss of generality, the particle is assumed to approach along the z direction. It can be shown that in the limit of large r, the scattering wave function takes the form of the sum of an incoming plane wave and an outgoing spherical wave [117].

$$\psi(R) = e^{ikz} + f(\vec{k})\frac{e^{ikR}}{R} \tag{5.1}$$

Thus "solving" the scattering problem amounts to determining the function $f(\vec{k})$. It is typical to determine $f(\vec{k})$ through partial wave analysis in which both the incoming and outgoing waves are expanded in the spherical harmonic basis, giving the following expansion which exploits the cylindrical symmetry of the scattering problem in a central potential.

$$f\left(\vec{k}\right) = \sum_{\ell=0}^{\infty} (2\ell+1)\, f_\ell\,(k)\, P_\ell\,(\cos\theta) \tag{5.2}$$

In the above, θ is the polar angle with respect to the z-axis. Noting that the central potential cannot couple different partial waves and that the total probability must be conserved, it can be shown that each partial wave scattering amplitude f_ℓ hinges on its particular phase shift δ_ℓ according to the following:

$$f_\ell\left(\vec{k}\right) = \frac{1}{k}\frac{1}{\tan\delta_\ell - i} \tag{5.3}$$

In samples of ultracold atoms, it is often more important to consider the effective potential that includes both the real potential and the centrifugal barrier.

$$V_{\text{eff}}(R) = V(R) + \frac{\hbar^2\ell(\ell+1)}{2\mu R^2} \tag{5.4}$$

In the above, μ is the reduced mass. Figure 5.1(b) schematically represents the further simplification of the scattering problem in ultracold neutral atoms: the angular momentum barrier classically forbids accessing the short-ranged central potential. In reality this only means that scattering from the higher order partial waves is strongly suppressed. Absent symmetry considerations for identical particles, only s-wave scattering need be considered.

Under certain conditions, the potential at long range may be neglected entirely. This is justified in the limit that $kR_0 \ll 1$ with R_0 being the effective range of the potential $V(R)$. For a typical Van der Waals interaction between neutral atoms $R_0 = \left(\frac{1\mu C_6}{\hbar^2}\right)^{1/4} \sim 10\,a_0$ whereas atoms that have been through even just the typical first stage of laser cooling can have a relative wave vector $\frac{1}{k} \sim 1000\,a_0$. It may be shown that for power law potentials $V \propto R^{-s}$ with $s > 2\ell+3$ the condition $kR_0 \ll 1$ enforces an asymptotic power law dependence on the scattering phase shifts, giving the following result for the s-wave phase shift [146, 117].

$$a_{\ell=0} \equiv a = -\lim_{k\to 0}\frac{\tan\delta_0}{k} \tag{5.5}$$

It is through this single parameter that the scattering properties of ultracold gases are typically analyzed (a notable exception being for identical fermions, which do not collide via s-wave for symmetry reasons). Beyond this point the s-wave scattering length will be referred to simply as *the* scattering length. As was briefly discussed in Chapter 3, the scattering length depends critically on the energy of the nearest threshold bound states supported by

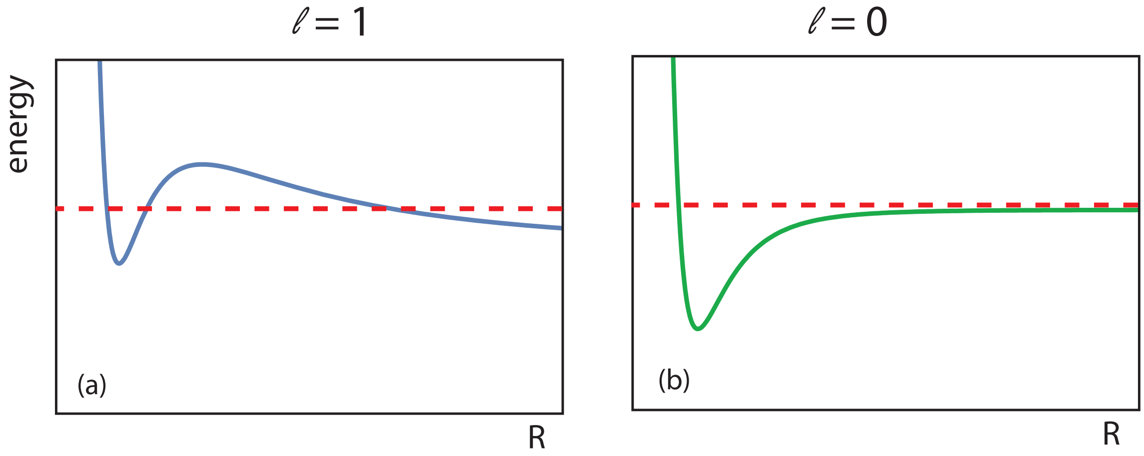

Figure 5.1: Two effective potentials for two-particle scattering. (a) is the effective potential for a *p*-wave collision that includes an angular momentum barrier. The scattering energy, $E = \frac{(\hbar k)^2}{2\mu}$ (dashed red) is drawn below the centrifugal barrier in order to suggest the minimal effect of the short-ranged central potential. (b) is the effective potential for particles in a *s*-wave collision in the same potential.

the interatomic potential. Further, the value and sign of a for certain combinations of ultracold gases have practical implications for cooling the gases.

Beyond determining the scattering length in general, the presence of bound states can cause resonant behavior, inducing a large change in the scattering length over a relatively narrow region of an experimentally tunable parameter space. In particular, a Feshbach resonance can arise when there are two or more distinct potentials through which the particles can scatter, as sketched in Figure 5.2(a). These different potentials are distinguished by different internal states of the scattering atoms in the large R limit and may be coupled to each other. The atoms will approach each other in an"open channel" where the scattering energy is above the asymptotic limit of the potential. However, under the condition that a second "closed channel," with asymptotic energy above the scattering energy, becomes nearly degenerate with the open-channel scattering state, the coupling strongly modifies the outgoing scattering wave.

It can be shown that the nature of this modification results in a resonant part of the scattering phase called δ_0^{res}. This additional phase is added to the uncoupled scattering phase that exists far from resonance in the open channel which we refer to as the background scattering phase, δ_0^{bg} [147]. Thus the total scattering phase is

$$\delta_0 = \delta_0^{\mathrm{bg}} + \delta_0^{\mathrm{res}} \tag{5.6}$$

Since we already know that the value of δ_0^{bg} is largely determined by the energies of the nearest threshold bound states, it remains to consider the form of δ_0^{res} and what effect it has on the scattering length. δ_0^{res} takes the Breit-Wigner form as shown below [147].

$$\delta_0^{\mathrm{res}} = -\arctan\left(\frac{\Gamma/2}{E - E_{\mathrm{res}} - \delta E}\right) \tag{5.7}$$

Here Γ describes the lifetime of the transiently occupied bound state in the closed channel, E_{res} is the energy at which the resonance occurs and δE is a shift of the resonance location from the energy of the closed-channel bound state. Although not explicitly formulated in

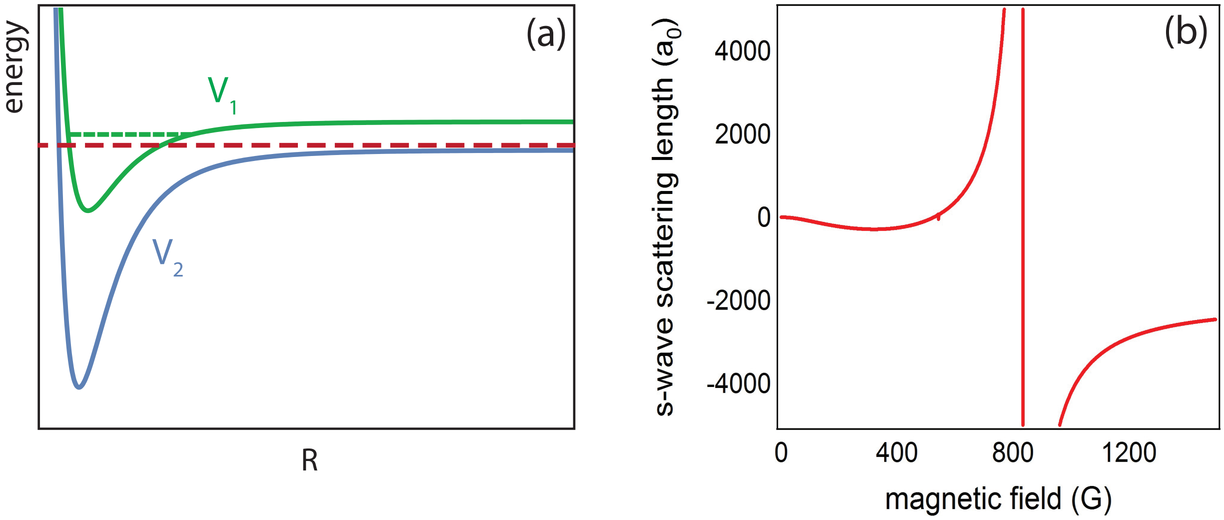

Figure 5.2: (a) A schematic example of two particle scattering in two distinct channels. V_1 and V_2 are distinguished by the internal states of the two scattering particles and may be coupled in the collisional Hamiltonian. These central potentials are drawn to suggest a typical dispersion interaction between typical neutral ground state atoms. (b) The s-wave scattering length between ^{6}Li atoms in two different hyperfine states, $|F, m_F\rangle = |1/2, -1/2\rangle$ and $|1/2, -1/2\rangle$ as a function of magnetic field. The broad resonance at 832 G dominates the spectrum but a much narrower resonance, barely resolved on this scale, is visible at 543 G.

the above, δE and Γ are k dependent.

To determine the effect of this resonant scattering phase on the scattering length, we plug into Equation 5.5 the new value of δ_0.

$$a = -\lim_{k\to 0}\frac{\delta_0^{\mathrm{bg}}}{k} - \lim_{k\to 0}\frac{1}{k}\arctan\left(\frac{\Gamma/2}{E - E_{\mathrm{res}} - \delta E}\right) \tag{5.8}$$

We note that the first term is simply the usual scattering length which we now label a_{bg} and apply the two threshold laws that govern the behavior of these resonances at low values of k: $\Gamma/2 \to k a_{\mathrm{bg}}\Gamma_0$ and $E_{\mathrm{res}} + \delta E \to E_0$ with Γ_0 being a k-independent constant that depends on the coupling between the open and closed channels.

$$a = a_{\mathrm{bg}} - \lim_{k\to 0}\frac{1}{k}\arctan\left(\frac{k a_{\mathrm{bg}}\Gamma_0}{E - E_0}\right) \tag{5.9}$$

$$a = a_{\mathrm{bg}} - \frac{a_{\mathrm{bg}}\Gamma_0}{E - E_0} = a_{\mathrm{bg}}\left(1 - \frac{\Gamma_0}{E - E_0}\right) \tag{5.10}$$

Now that we understand the effect of the resonant portion of the scattering phase shift on the scattering length, we focus in particular on the possibility that the quantity $E - E_0$ can be experimentally changed. This will be possible via the Zeeman effect if the bound state in the closed scattering channel (green dashed line in Figure 5.2) and the scattering state of the open channel (red dashed line in Figure 5.2) have different magnetic moments. By calling the difference in their magnetic moments δ_μ we find that the scattering length is a function of magnetic field.

$$a = a_{\mathrm{bg}}\left(1 - \frac{\Gamma_0/\delta_\mu}{(E - E_0)/\delta_\mu}\right) = a_{\mathrm{bg}}\left(1 - \frac{\Delta}{B - B_0}\right) \tag{5.11}$$

A resonance which arises through Zeeman tuning is called a “magnetic Feshbach resonance” and is by far the most common scattering resonance exploited in ultracold atoms. From Equation 5.11 we conclude that if a Feshbach resonance exists at $B = B_0$, the scattering length will experience a pole with a width $\Delta = \Gamma_0/\delta_\mu$, as seen in the example of ^{6}Li, shown in Figure 5.2(b). Thus the scattering length is tunable not only in magnitude but also in sign, allowing an experimenter to both control the strength of the contact interactions between ultracold atoms but also to change their character from attractive to repulsive - all by simply changing the magnetic field. In the following section, we will see the many ways in which this has expanded the scientific reach of ultracold atoms.

5.2 Applications of MFRs to Cold Atom Physics

MFRs are critical ingredients in a large subset of cutting edge ultracold atoms experiments and have long been considered a standard “tool” on the experimenter’s metaphorical workbench. The most powerful aspect of the MFR is the ability to control the s-wave scattering length as is demonstrated in Figure 5.2(b) [148]. This ability to tune the interactions between particles using a magnetic field is of fundamental importance to cold atom studies of many- and few-body physics.

Outside of the observation of MFRs themselves, using MFRs to modify the interactions between ultracold atoms has made them a fruitful platform for studies of few-body physics through their ability to study “universal properties” which are exhibited in different physical systems with different interactions [149, 150, 151]. This universal scattering regime can be engineered within an ultracold sample by eliminating the importance of the interatomic spacing and the interaction range. Although this spacing remains large in these dilute gases ($\sim 10^5 a_0$), near an MFR the s-wave scattering length can be made arbitrarily large such that both the interparticle spacing and interaction range are irrelevant.

By using the tunability of the scattering length near an MFR, ultracold atoms were the first platform to allow the direct observation of a particular aspect of this universal behavior: the formation of Efimov states [152], families of three-body bound states that exist even when the constituent two-body interactions are too weak to support a bound state themselves [153]. While Efimov physics has been studied in a number of unique ultracold systems, including mixtures of different species, the interplay between resonant interactions and symmetrization requirements is a vast area of theoretical study and motivates experimental input through the extension of Efimov studies in ultracold gases to new atomic mixtures [154].

Ultracold atoms are presently the leading platform for quantum simulation, a broad field of study that leverages the controllability of an experimenter's quantum system to model phenomena in other systems of interest which both defy explication by an analytical or numerical model and are experimentally less amenable to manipulation or observation [155, 156]. Using an MFR to change the interactions of a model system is fundamental to exploring its phase space. A prominent example of quantum simulation with ultracold atoms is the precise study of the BEC-BCS crossover using ultracold fermions, the theory of which is thought to be intimately connected to that of high temperature superconductivity [157]. Feshbach resonances have also been used to observe quantum phase transitions such as the Mott insulator-superfluid transition [158], the BEC-supersolid transition [159, 160, 161] and the Berezinskii–Kosterlitz–Thouless transition [162].

It is common to see the use of MFRs in the simulation of condensed matter systems in which ultracold atoms are loaded into an optical lattice which simulates the ionic structure of solids, but quantum simulation with ultracold atoms can also be applicable to many other fields of physics. For example, ultracold atoms can be used to simulate cosmic inflation [163, 164], lattice gauge theories [165], and neutron stars [166].

While one might say that the studies described above used MFRs as a tool to achieve their result, the interactions were themselves part of the physics being studied. In contrast, MFRs have been utilized as a tool simply to create novel forms of ultracold gases. The use of MFRs is critical to the observation of superfluidity in Fermi gases [167]. As a more practical example, the ability to control the scattering length was a critical step in the formation of BECs in ^{85}Rb and ^{133}Cs for which the effective use of evaporative cooling to create a BEC is impossible without the use of MFRs [168, 169].

But in terms of using MFRs as a tool to create more exotic quantum gases, the most prominent example is the efficient creation of ultracold dimers via association of ultracold atoms. In the most naive interpretation, one can think of using an MFR to essentially trap the molecules which transiently formed as a bound state in the closed channel by raising the scattering energy, or alternately, lowering the energy of the bound state relative to the scattering energy. This is something we can do with the magnetic field! However, such a naive scheme would not be very efficient.

It is better to exploit the atom-molecule coupling inherent to MFRs to perform an adiabatic transfer from an atomic state to a molecular state. Figure 5.3 shows the premise of this strategy. At the location of an MFR there is a crossing between a scattering state (which we would consider to be a pair of free atoms) and a bound state (which we would consider a molecule). However, coupling between the two-particle scattering channels opens an avoided crossing. Thus, by sweeping the magnetic field adiabatically across this avoided crossing, atomic states can be efficiently and coherently transformed into molecular states without any change to the center-of-mass motion [71].

A practical implication of using Zeeman tuning to control a scattering resonance is that these "Feshbach" molecules are almost always formed in the least-bound state of the molecule, or in other words, the most vibrationally excited state. In this state molecules are collisionally unstable. Collisions between two molecules or between molecules and unassociated atoms may change the vibrational, rotational or hyperfine state of the molecule, always releasing energy. However, there are ways of creating collisionally stable molecular samples starting from the ultracold Feshbach molecules created by with magnetic field ramp. Thus use of an MFR is an essential first step in creating ultracold molecules via the indirect method.

5.3 Prototypical MFR: Interactions in the Bialkali Dimer

After the first observation of a magnetic Feshbach resonance in ultracold atoms in 1998, the number of new publications with the word "Feshbach resonance" increased by about a factor of 10 [170, 171, 147]. This can be attributed not only to the scientific allure of the rich applications described in the previous section, but also because MFRs were broadly accessible; MFRs can be found at experimentally achievable fields in almost all alkali species, the class of atoms that dominates the ultracold atoms population. To draw a better contrast with the work in this thesis, it is worthwhile to briefly consider the reasons for this seeming

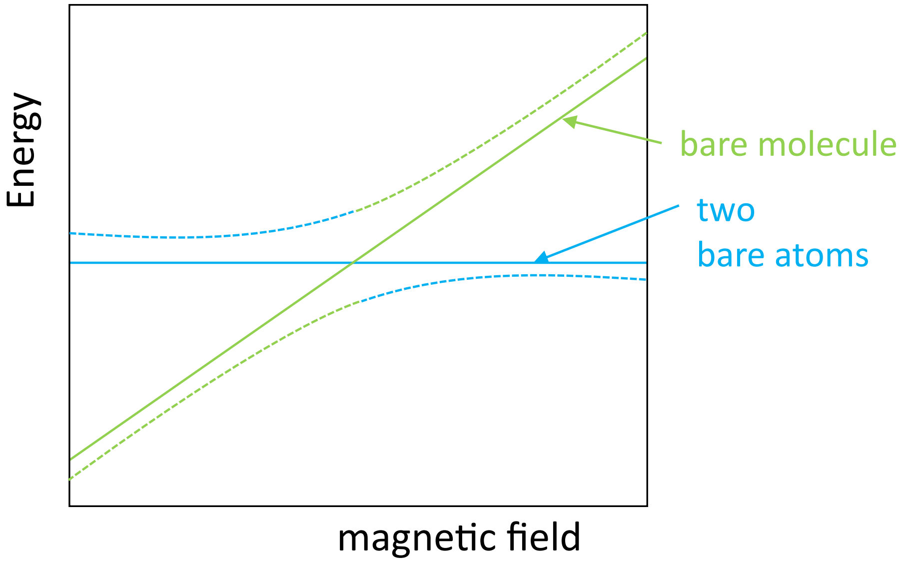

Figure 5.3: A schematic representation of a Feshbach resonance as an avoided crossing between atomic (scattering) and molecular (bound) states. The differential magnetic moment gives rise to a crossing between the scattering (blue) and bound state (green) which is avoided if there is a coupling between the two. The dashed lines represent the adiabatic eigenstates of the atom-molecule system.

abundance of MFRs.

As mentioned in Section 5.1, Feshbach resonances can arise only when there is a coupling between two different scattering channels. Alkali+alkali combinations, when colliding in the electronic ground state, represent a combination of ^2S and ^2S electronic states. Thus there are two distinct scattering channels depending on the relative orientation of the valence electron with $s_1 = s_2 = 1/2$: the singlet and triplet channels. These channels will be coupled to each other due to the combined effect of the hyperfine coupling present in each constituent atom. To examine this in more detail, consider the Hamiltonian of a pair of alkali atoms [172]:

$$H = \frac{-\hbar^2}{2\mu}\nabla^2 + V_D + \underbrace{[\mu_1\vec{s_1} + \mu_2\vec{s_2}] \cdot \vec{B}}_{\text{Zeeman shifts}} + \underbrace{[a_1\vec{s_1} \cdot \vec{i_1} + a_2\vec{s_2} \cdot \vec{i_2}]}_{\text{hyperfine interactions}} \tag{5.12}$$

In the above, V_D captures the electrostatic interaction between atoms 1 and 2, and μ is the reduced mass in the relative kinetic energy term. Not included for simplicity here are the relatively small nuclear Zeeman shifts and direct interactions between $\vec{s_1}$ and $\vec{s_2}$. The coupling that is responsible for most MFRs exhibited in alkali+alkali combinations is due to the fact that the combined hyperfine interactions are not diagonal in the total spin $\vec{S} = \vec{s_1} + \vec{s_2}$ as can be seen through a suggestive rewriting of the sum of the hyperfine interaction terms:

$$[a_1\vec{s_1} \cdot \vec{i_1} + a_2\vec{s_2} \cdot \vec{i_2}] = \vec{S} \cdot \left(\frac{a_1}{2}\vec{i_1} + \frac{a_2}{2}\vec{i_2}\right) + \frac{a_1}{2}\left(\vec{s_1} - \vec{s_2}\right) \cdot \vec{i_1} + \frac{a_2}{2}\left(\vec{s_2} - \vec{s_1}\right) \cdot \vec{i_2} \tag{5.13}$$

The last two terms in Equation 5.13 are not diagonal in the $\left\{\vec{S} = 0, 1\right\}$ basis. This provides the coupling between the singlet and triplet states that is at the heart of the majority (though not all) MFRs among pairs of alkali atoms.

5.4 Exotic MFRs

In the previous section we saw that a relative spin degree of freedom was responsible for distinguishing two coupled scattering channels. However, MFRs can arise from scattering channels distinguished by other degrees of freedom, such as the orbital angular momentum.

Indeed the photoassociation processes studied in the previous chapter constitute Feshbach resonances hinging on the orbital angular momentum, though the scattering resonances in photoassociation are typically referred to as *optical* Feshbach resonances because they are not tuned with the Zeeman effect [173, 174].

Another opportunity to utilize the orbital angular momentum degree of freedom to control interactions - without the use of a laser field - is found in the electronic structure of alkaline-earth (e.g. Sr) and alkaline-earth-like (e.g. Yb) atoms which exhibit metastable excited states with lifetimes in excess of 10 or even 100 seconds [175, 176]. Thus, it is possible to prepare a long-lived mixture of ground and excited state atoms which may exhibit Feshbach resonances due to novel couplings. For example it was predicted and later observed that inter-orbital spin exchange interactions between the ${}^1S_0$ and ${}^3P_0$ states of ^{173}Yb causes an MFR [177, 178].

MFRs have also been observed in the ${}^1S_0$ and ${}^3P_2$ combination in both ^{170}Yb and ^{174}Yb, arising not from a relative spin degree of freedom but from anisotropic contributions to the electrostatic interaction V_D [179]. Interactions of this character were also predicted to exist in heteronuclear combinations and were observed by our group between ground state ^{6}Li and ^{174}Yb in the ${}^3P_2$ excited state [180, 181, 182, 183]. Indeed interactions of this kind have proven to be rather widespread, leading to MFRs that have been observed in the lanthanides dysprosium [184, 185, 186, 187] and erbium [188, 187]. More recently, an anisotropy-induced MFR was observed between ground state dysprosium and potassium [189]. Feshbach resonances have also been observed in an ultracold gas containing atomic potassium and the dimer NaK [190].

Finally, the first observation of MFRs between closed- and open-shell atoms was made in RbSr [83] which will be explained in the following section. In the next section, we will discuss the origin of the exotic MFRs observed in this thesis: those between ${}^2S$ (open shell) and ${}^1S$ (closed-shell) atoms such as ground state Li and Yb.

5.5 *Interactions in the* ^1S + ^2S *System*

First consider the Hamiltonian for a pair of such atoms which we will label using the subscripts Li and Yb for concreteness.

$$H = \frac{-\hbar^2}{2\mu}\nabla^2 + V_D + H_{\mathrm{Li}}^{\mathrm{asym}} + H_{\mathrm{Yb}}^{\mathrm{asym}} + U_{\mathrm{int}} \tag{5.14a}$$

$$H_{\mathrm{Yb}}^{\mathrm{asym}} = g_{\mathrm{Yb}}\mu_N \vec{i_{\mathrm{Yb}}} \cdot \vec{B} \tag{5.14b}$$

$$H_{\mathrm{Li}}^{\mathrm{asym}} = g_{\mathrm{Li}}\mu_N \vec{i_{\mathrm{Li}}} \cdot \vec{B} + g_{\mathrm{e}}\mu_B \vec{i_{\mathrm{Li}}} \cdot \vec{B} + a_{\mathrm{Li}}\vec{s_{\mathrm{Li}}} \cdot \vec{i_{\mathrm{Li}}} \tag{5.14c}$$

Here g_e is the electronic g-factor for the Li $^2S_{1/2}$ ground state, g_{Li} and g_{Yb} are the appropriate nuclear g-factors, μ_B is the Bohr magneton, μ_N is the nuclear magneton, and a_{Li} is the hyperfine constant for Li (often labeled as ζ_{Li} in the literature).

The existence of MFRs arising from this Hamiltonian depends on the nature of U_{int}. In the efforts to predict the locations of feasible MFRs (that is to say resonances at fields low enough to be reached in a cold atoms lab and wide enough to be used for magneto-association) in the $^1S +^2 S$ system, many different interactions have been considered for U_{int} [191, 192, 193, 83]. We will discuss only those interactions presently considered to be the strongest: those arising from a change to the electron spin density at one nucleus in response to the proximity of the other nucleus, which are given below.

$$U_{\mathrm{int}} = \underbrace{\Delta a_{\mathrm{Li}}\vec{i_{\mathrm{Li}}} \cdot \vec{s_{\mathrm{Li}}}}_{\text{coupling mechanism I}} + \underbrace{\Delta a_{\mathrm{Yb}}\vec{i_{\mathrm{Yb}}} \cdot \vec{s_{\mathrm{Li}}}}_{\text{coupling mechanism II}} \tag{5.15}$$

Here the modification to the hyperfine constants Δa_{Li} and Δa_{Yb} are dependent on the internuclear distance R and are nonzero only at short range ($R \lesssim 10\, a_0$). The name "coupling mechanisms I and II" are used as shorthand in the literature.

Before our experimental study of MFRs in the YbLi system, the nature of the MFRs arising from these two coupling mechanisms had been investigated theoretically by two groups. Although accurate predictions for the locations of these resonances required the input of experimental data, the widths were theoretically predicted and the relevant selection rules

	Width from [191]	Width from Kotochigova Group	Selection Rule
coupling mechanism I	1.0 μG	0.48 μG	$m_{F,\mathrm{Li}}^{\mathrm{final}} = m_{F,\mathrm{Li}}^{\mathrm{initial}}$
coupling mechanism II	824 μG	49.6 μG	$m_{F,\mathrm{Li}}^{\mathrm{final}} - m_{F,\mathrm{Li}}^{\mathrm{initial}} = \pm 1$

Table 5.1: Theoretical predictions on the properties of MFRs in ^{173}Yb^{6}Li. The predicted widths, Δ, will vary depending on the spin states of the atoms involved so here the maximum predicted width is shown as an example. Details on the identification of the spin states are in Section 2.4.1.

for s-wave MFRs noted. As described in greater detail in Section 5.8.2, the selection rules associated with the coupling mechanism can be combined with experimental data on the near-threshold molecular bound states to accurately predict the locations of the MFRs. Table 5.1 summarizes the theoretical predictions for MFRs in ^{173}Yb^{6}Li, the isotopologue used in this work.

Before discussing the predictions for the locations of the MFRs studied here, we will review the experimental work required to observe them. The first requirement was to switch the Yb isotope we were trapping. Up to this point, the experimental results in this thesis have been collected by using our ultracold atoms apparatus to create samples of ^{6}Li and ^{174}Yb. However, the widest MFRs predicted in YbLi require a nonzero nuclear spin in Yb which ^{174}Yb does not possess. As we wished to access the widest MFRs, we needed to switch to producing mixtures of ^{6}Li and ^{173}Yb instead. A description of this switch can be found in the appendix.

In order to study the spin dependence of the YbLi MFRs we aimed to repeat our trap-loss spectroscopy with both the Li and Yb in various single nuclear spin states. The methods for creating spin-polarized samples are discussed in the next two sections.

5.6 Controlling the Li Spin Polarization

Throughout this discussion the Li spin state will be described as in Section 2.4.1.

5.6.1 Determining the spin composition of the ultracold Li sample

In the course of completing this thesis we have worked exclusively with Li in the states $|1\rangle$, $|2\rangle$, and $|3\rangle$ as the final product of our cooling and trapping stages. We determine the spin composition of our ultracold Li sample by performing state dependent absorption imaging on these states. Although all correspond to $m_J = -\frac{1}{2}$, these states are split by $\sim 100\,\mathrm{MHz}$ at fields exceeding $\sim 100\,\mathrm{G}$ as shown in Figure 2.3. This splitting is much larger than the natural linewidth ($\Gamma/2\pi = 5.9\,\mathrm{MHz}$) of the electronic transition connecting the ${}^2S_{1/2}$ ground state to the ${}^2P_{3/2}$ excited state which we use for absorption imaging. By simply performing absorption imaging three times - each time using a frequency resonant with the state of interest - we can determine how many of the total number of atoms are in each state.

In reality, our experimental setup used to control the frequency of the imaging beam (composed principally of a double passed AOM operating at 200 MHz) cannot easily span the full range of frequencies required to be resonant with all three states at the same field. Therefore it is our general practice to shift the field at which imaging takes place by 20 - 50 G to bring the resonance of interest near the imaging AOM's center frequency and use our control of the AOM frequency to finely adjust the laser frequency to match the resonance at that field. We note here that preparation of the Li in a single spin state is such a routine procedure that for most experiments we do not bother imaging the sample all three times, each time resonant with a different state.

5.6.2 Preparing the Li spin

We control the Li spin state through a combination of optical pumping, removal by resonant scattering, and Landau-Zener sweeps across RF resonances. For a typical experimental run on our apparatus, the Li is prepared in $|2\rangle$ for the evaporation stage in the following way.

After the MOT compression stage, atoms in the ODT are in all six hyperfine ground states. We then extinguish the repump beam such that only light addressing the $^2S_{1/2}\,(F = 3/2) \rightarrow {}^2P_{3/2}\,(F')$ transition is applied to the atoms, pumping them into the $F = 1/2$ state. While holding this mixture of $|1\rangle$ and $|2\rangle$ in the trap, we ramp the magnetic field to $\approx 500\,\mathrm{G}$. At this field, the hyperfine ground states are resolved (see Figure 2.3) with respect to the probe electronic transition and we apply a laser pulse resonant only with $|1\rangle$ to remove those atoms from the trap.

More recently, we accidentally discovered that maintaining the various DC fields used to compress the MOT during the optical pumping pulse allowed us to prepare the sample of atoms entirely in $|2\rangle$. We have speculated that the field is splitting the excited hyperfine states to such a degree that the optical pumping pulse is more strongly populating those excited m_F' states that connect to $|2\rangle$ though this could only explain a slight imbalance in favor of $|2\rangle$, not an entire transfer into $|2\rangle$ that we observe.

After the atoms are prepared in $|2\rangle$, we typically perform evaporative cooling on Yb before preparing the Li spin state as desired. If not wanting to perform experiments with $|2\rangle$ we perform Landau-Zener (LZ) sweeps across the RF resonance $|2\rangle \leftrightarrow |3\rangle$ or $|2\rangle \leftrightarrow |1\rangle$. To perform these sweeps, we first identify the resonant frequency at the field chosen for the transfer using the same method as described in Section 5.9.2. Then, we must find a suitable frequency ramp across this resonance. We typically choose a frequency range spanning $80\,\mathrm{kHz}$. We then empirically determine the sweep time that will make the process adiabatic and thus an efficient transfer scheme. Figure 5.4 gives an example of a transfer from $|2\rangle$ to $|1\rangle$ by plotting the atom number in each of the two states as the total time for the sweep is changed, changing the rate of the LZ sweep. For a typical $2\,\mathrm{W}$ of RF power, the time needed for efficient transfer is $\approx 100\,\mathrm{ms}$. Although we typically use this method to completely transfer into a single state, we can also use this method to create superpositions of two adjacent states by choosing a nonadiabatic ramp speed. Such a superposition will subsequently decohere into a spin mixture, which is important for observing interactions between different Li spin states.

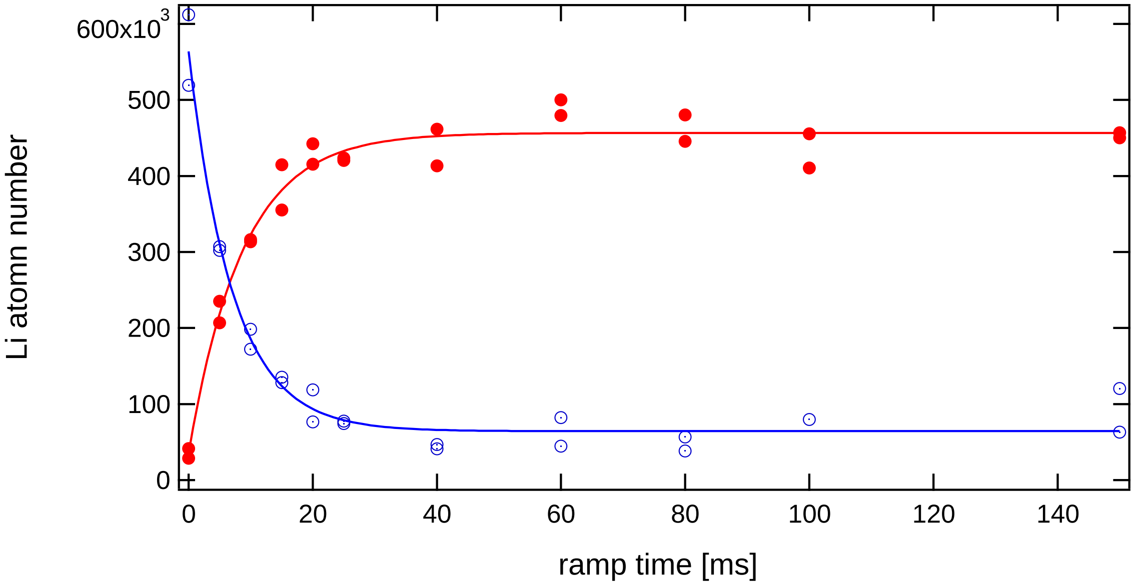

Figure 5.4: The population in $|1\rangle$ (closed red circles) and $|2\rangle$ (open blue circles) as the total time of the Landau-Zener sweep is varied. The frequency span of the sweep is kept the same. For each time, the experiment is done twice - once while imaging $|1\rangle$ and once while imaging $|2\rangle$. This resonance was taken at 480 G. The RF power supplied to the antenna was 1 W and the sweep range was 20 kHz. We typically remove the residual population in $|2\rangle$ using a resonant light pulse.

5.7 Controlling the Yb Spin Polarization

The central feature of Yb in the context of making YbLi molecules is its closed-shell electronic structure. However, this feature complicates the necessity of preparing the ^{173}Yb in a particular nuclear state. Unlike Li there is no hyperfine coupling in the ground state that splits different nuclear states by a significant amount. Because $S = 0$, different m_I states in ^{173}Yb split at a rate of $E_{\text{Zeeman}} = g_N \mu_N m_I B$. Thus, the six different nuclear states split at a rate $\sim 1\,\text{kHz/G}$. This splitting is too small to allow for each of the nuclear states in the ground state to be individually addressed as in Section 5.6, assuming the we would use the strong $^1S_0 \rightarrow {}^1P_1$ transition. Instead we used distinct techniques for both diagnosing and controlling the spin population of the Yb sample.

5.7.1 State Labeling

In the case of ^{173}Yb in the $^1S_0$ ground state, there is only a single hyperfine ground state at zero field, which is the sum of $S = 0$ and $I = {}^5\!/_2$, namely $F = {}^5\!/_2$. Consequently, m_F is equivalent to m_I. When discussing the magnetic substates of $^1S_0$ in this thesis, we will use these labels interchangeably.

5.7.2 Optical Stern-Gerlach

To determine the spin composition of the Yb sample, we perform a Stern-Gerlach test, spatially separating the spin states before taking an absorption image that allows us to count the number of atoms in each cloud. A typical Stern-Gerlach experiment would use a DC magnetic field gradient to provide a spin dependent force on the sample. But the weak magnetic moment of Yb atoms means that the magnetic field gradient required to separate the different spin states before each cloud disperses into the vacuum is infeasibly high. To be more specific, the rate of separation of the different spin states must exceed the rate of expansion as the cloud is released from the trap. The rate of expansion goes as $\sqrt{\frac{k_B T}{m}}$ where k_B is the Boltzmann constant, T is the temperature of the gas and m is the mass of the

Yb atom. The rate of separation goes as $\frac{g_N \mu_N B'}{m} t$ where t is the time since release from the trap. Supposing a typical expansion time of 10 ms, a gradient of $> 1\,\mathrm{T/cm}$ would be required to make these two rates comparable.

An optical Stern-Gerlach (OSG) procedure obviates the need for a magnetic field gradient by providing a spin dependent force with laser light [194, 195, 196]. Specifically, the optical dipole force is used to create a potential with a strength that decreases as the value of the nuclear spin state increases from $-\frac{5}{2}$ to $+\frac{5}{2}$ (or the reverse). Consider the dipole force under the assumption that the laser beam is tuned near to only one electronic transition of the Yb atom [100]:

$$\vec{F} = -\nabla U_{dip} \tag{5.16}$$

$$U_{dip,g} = \frac{3\pi c^2 \Gamma}{2\omega_0^3} I(r) \sum_e \frac{\mid c_{ge} \mid^2}{\delta_{eg}} \tag{5.17}$$

where we have suggestively labeled the state of interest as g (for ground) and the states contributing to the sum e (for excited). Γ is the natural linewidth of the electronic transition relevant for this calculation. δ_{eg} is the detuning from the $g \to e$ transition, c is the speed of light and ω_0 is the energy the $g \to e$ transition in radial frequency units. $I(r)$ is the spatially dependent intensity of the laser beam. Of the most importance for subsequent discussion is c_{eg}, the Clebsch-Gordan coefficient.

Figure 5.5 demonstrates the principle of creating a spin dependent force on the magnetic substates of the Yb ground state using the optical dipole potential. We use a laser beam which is tuned near the ${}^1S_0 \to {}^3P_1$ transition. Considering as a first example only the light-matter interaction with the $F' = 7/2$ state, it's clear that a σ^+ laser beam would exert a significantly greater force on the $m_F = +5/2$ state than the $m_F = +3/2$ and that subsequent decrease in the spin state projection quantum number would every time decrease the dipole force experienced. This is because the only term in Equation 5.17 which varies from state to state is $\mid c_{ge} \mid^2$, a monotonic function in m_F as long as the light is circularly polarized.

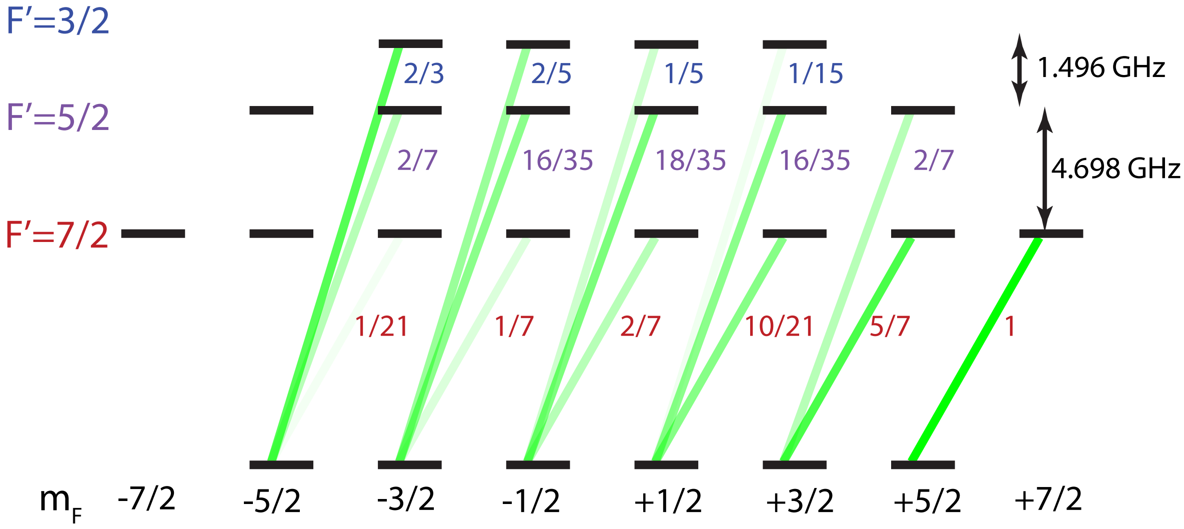

Figure 5.5: Electric dipole transitions between the hyperfine states of $^1S_0$ and $^3P_1$ (not to scale). Only σ^+ transitions are shown for clarity. The transitions are shaded according to their relative strength and each transition is labelled with the value of the square of the Clebsch-Gordan coefficient.

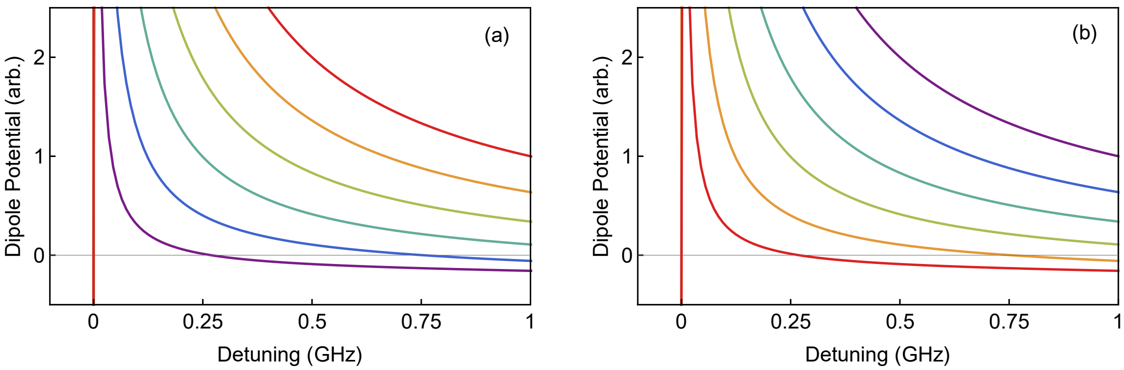

Figure 5.6: The relative strength of the dipole potential experience by each of the six hyperfine ground states of ^{173}Yb depending on the detuning from the $^1S_0\,(F = {}^5\!/_2) \rightarrow {}^3P_1\,(F' = {}^7\!/_2)$ transition. Only contributions from the $^1S_0 \rightarrow {}^3P_1$ need be considered. The states are distinguished on the plot by a rainbow gradient with purple for $m_F = -{}^5\!/_2$ and red for $m_F = +{}^5\!/_2$. (a) assumes pure σ^+ polarization while (b) assumes pure σ^- polarization.

However, contributions from the other two excited hyperfine states will also add to the sum in Equation 5.17. By properly selecting a laser frequency (and hence setting a suitable detuning from each excited hyperfine state) we can create a dipole potential that is monotonic in the value of m_F. Figure 5.6 displays the relative dipole potential experienced by the six ground states for various detunings from the $^1S_0\,(F = {}^5\!/_2) \rightarrow {}^3P_1\,(F' = {}^7\!/_2)$ transition.

In our lab it was most convenient to produce a laser beam with $\delta = +2\pi \times 860\,\mathrm{MHz}$, resulting in a repulsive potential for most states. This was close enough to achieve reasonably disparate dipole forces for all six states while preventing deleterious spontaneous scatter during the OSG test. For reasons described in the appendix, the polarization of the OSG beam is σ^+. Note that the $m_F = -{}^5\!/_2$ state actually experiences an attractive force and the $m_F = -{}^3\!/_2$ state nearly none at all because the force on these have larger contributions from the excited states which the laser is actually red-detuned from. If the practical constraints of producing the OSG beam by shifting the zeroth order of the MOT AOM were not critical,

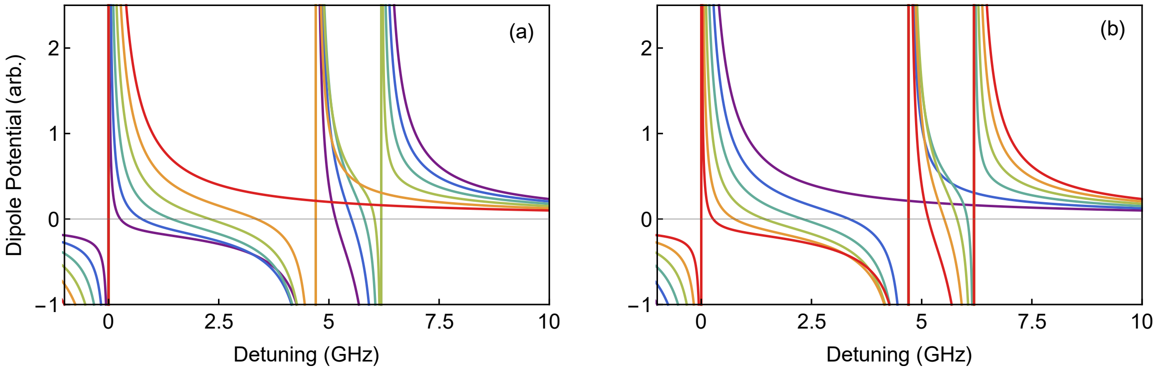

Figure 5.7: The relative strength of the dipole potential experienced by each of the six hyperfine ground states of ^{173}Yb, now considering a larger range of detunings from the $^1S_0\,(F = 5/2) \rightarrow {}^3P_1\,(F' = 7/2)$ transition. Only contributions from the $^1S_0 \rightarrow {}^3P_1$ need be considered. The states are distinguished on the plot by a rainbow gradient with purple for $m_F = -5/2$ and red for $m_F = 5/2$. (a) assumes pure σ^+ polarization while (b) assumes pure σ^- polarization.

we might have wanted to use a beam that was blue detuned from all hyperfine transitions such that both the $m_F = -5/2$ and $m_F = -3/2$ states would experience a repulsive potential (see Figure 5.7) and thus be easier to distinguish in the OSG test.

The behavior of the Yb atoms under the influence of the OSG beam is highly sensitive to the placement of the OSG beam relative to the location of the trapped atoms. The alignment of the OSG beam is discussed in the appendix. To perform an OSG test, we release the Yb atoms from the ODT in which they are held and simultaneously flash on the OSG beam for 1-2 ms as the atom cloud is expanding in time of flight. The OSG beam is both larger in width than the trapped atom cloud at and intentionally misaligned from the cloud as shown schematically in Figure 5.8(a). We attempt to point the OSG beam so that the atoms sample the largest gradient of the laser intensity along one direction while sampling very little in the other direction. After 4-6 additional ms of time of flight absent the OSG beam,

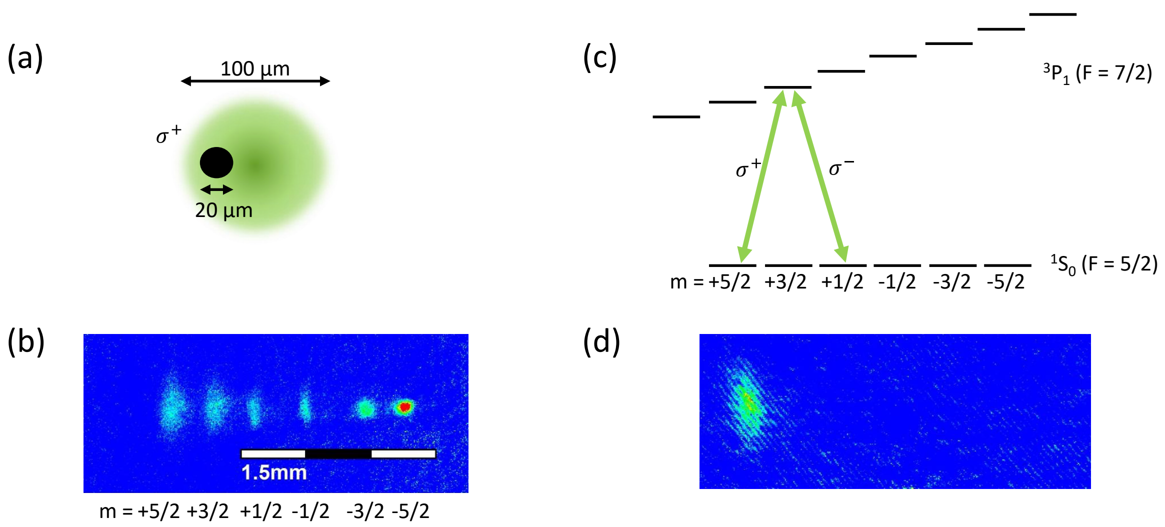

Figure 5.8: Schematic and results for OSG and optical pumping. (a) a representation of the OSG beam (green) placement relative to the atomic cloud (black). (b) an absorption image taken after OSG is performed under the condition that no optical pumping is performed. (c) a schematic representing one stage of optical pumping which would pump atoms from $m_F = +5/2$ and $m_F = +1/2$ into $m_F = +3/2$. (d) an absorption image taken after OSG is performed. Here, a series of optical pumping pulses has been used to transfer the population into the $m_F = +5/2$ state prior to the OSG test.

the atoms are imaged by absorption on the $^1S_0 \rightarrow {}^1P_1$ transition. Figure 5.8(b) shows the results of this test when it was performed on a “typical” sample of Yb atoms in our trap. It should be noted that fully separated clouds as shown in Figure 5.8(b) are only possible in the coldest samples we could easily achieve for these tests. In practice we found that we could not produce good OSG results if the temperature of the cloud before release from the trap was greater than 500 nK. A field of 7 G is used to set the quantization axis.

5.7.3 Optical Pumping

We saw in Section 5.6 that the residual effects of the hyperfine coupling within the Li atom allowed us to manipulate the spin polarization of our sample at high field because the different ground hyperfine states are resolved. We could either address these ground hyperfine states individually through removal by resonant scattering or by rapid adiabatic passage with RF transitions between adjacent ground magnetic substates. As alluded to at the beginning of this section, the lack of hyperfine coupling in the Yb ground state precludes the first option. The second option is impossible because the RF resonances between different hyperfine ground state are necessarily degenerate because they are split from each other only by Zeeman energy of the nuclear spin states (no hyperfine coupling).

Instead we utilize the relatively narrow ${}^1S_0 \rightarrow {}^3P_1$ transition to perform optical pumping, targeting different ground magnetic substates through proper choice of the polarization and dependence on selection rules rather than frequency selectivity between the ground substates. In contrast to the ground state, the ${}^3P_1$ excited state has a sizable magnetic moment $\sim \mu_B$. Given that for this transition ${}^{\Gamma}\!/_{2\pi} = 180\,\mathrm{kHz}$, a field of only a few G is required to split the states by many times the linewidth of this transition. In reality we are limited by the $\sim 1\,\mathrm{MHz}$ linewidth of the 556 nm laser used to address these transitions, so in order to selectively address the different magnetic substates of ${}^3P_1$, we usually apply a magnetic field of $50\,\mathrm{G}$, splitting adjacent states by $21.4\,\mathrm{MHz}$.

Figure 5.8(c) shows how addressing resolved magnetic substates in the ${}^3P_1$ state allows us to manipulate the spin polarization of the ground state population. In this example, laser light is resonant with ${}^1S_0\,(m) \rightarrow {}^3P_1\,(m' = +{}^3\!/_2)$. Atoms in the $m'_F = +{}^3\!/_2$ state can decay back to $m_F = +{}^5\!/_2, +{}^3\!/_2, +{}^1\!/_2$ but only $m_F = +{}^3\!/_2$ is dark to the optical pumping light so population will be pumped from $m_F = +{}^5\!/_2, +{}^1\!/_2$ into $m_F = +{}^3\!/_2$. By applying multiple pulses in sequence, each targeting a different m'_F state, the Yb sample can be prepared in a single ground magnetic substate, as demonstrated in Figure 5.8(d).

Conveniently, the apparatus needed very little modification for implementing optical pumping of this kind as laser beams tuned near the ${}^1S_0\,(F = 5/2) \rightarrow {}^3P_1\,(F' = 7/2)$ transition already entered the vacuum chamber from several directions in the form of the MOT beams. For this reason, the beams that achieve the optical pumping will simply be referred to as the MOT beams. To achieve the proper polarizations for the optical pumping, we used a motorized flipper mount to block the two horizontal MOT beam pairs. The vertical MOT beam pair runs parallel to both our two principal electromagnets - the anti-Helmholtz coils for the MOT gradient and the Helmholtz coils for the bias field. Thus, the vertical MOT beam pair has a polarization designed to address both σ^+ and σ^- transitions in the presence of the bias field used to split the excited magnetic substates.

To selectively address different m'_F states, we changed the frequency of the MOT beams by controlling the RF tone applied to the MOT AOM. To determine the frequency to apply to the AOM in order to address each individual state, we first calculated the g-factor of the ${}^3P_1\,(F' = 7/2)$ state to be 0.58. We used this calculation to predict the shift of each state from the zero field ${}^1S_0 \rightarrow {}^3P_1$ resonance at 50 G. With this initial guess we performed spectroscopy to determine the shift more accurately. For simplicity this took the form of a "blast resonance" in which we apply the MOT beams to the atoms held into ODT for a fixed amount of time and measure the remaining atom number. Resonant light scattering removes atoms from the trap leading to dips in the atom number on resonance (See Figure 5.9). Note that for this purpose, we use all six MOT beams, rather than the vertical pair alone, to prevent optical pumping from stopping the loss from the trap.

Once the proper frequency for each resonance is known, we took care to prevent MOT light from reaching the atoms unless we were performing intentional optical pumping. This was challenging as a small amount of light can diffract through the AOM and reach the atoms even when we have set the RF power to the AOM to be zero with our control system. For this reason, a typical optical pumping scheme would follow this sequence: set the MOT AOM frequency to the first target m'_F state, open the MOT shutter and pulse on the MOT AOM, turn off the MOT AOM and close the MOT shutter, change the MOT AOM frequency to the second target m'_F, etc.

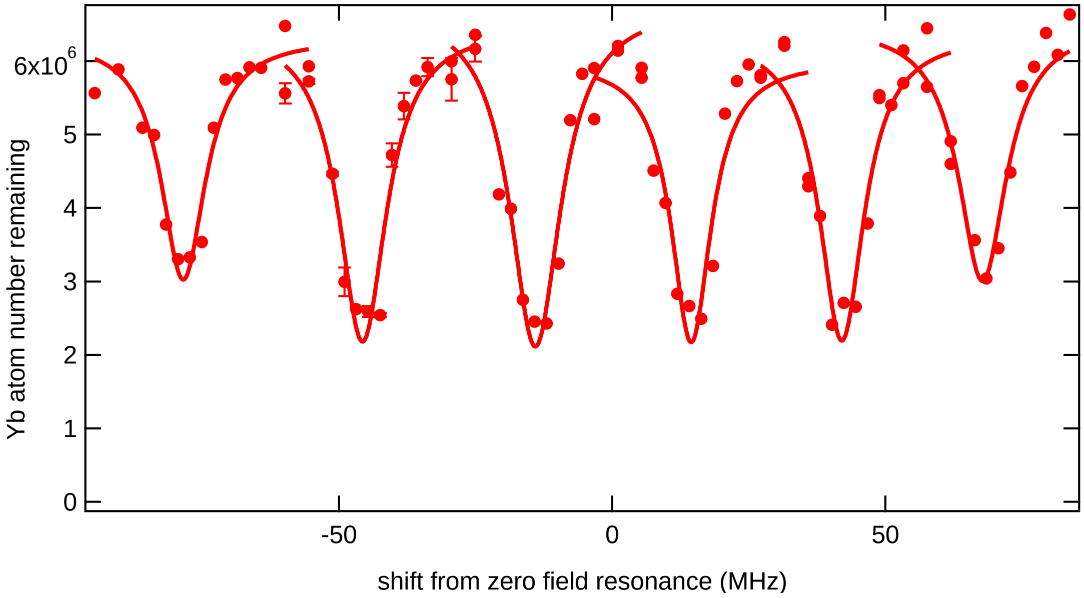

Figure 5.9: “Green blast resonance”. All six MOT beams are used to blast atoms from the trap when on resonance. Here are six peaks corresponding to the states $m'_F = -5/2, ..., 5/2$. States $\pm 7/2$ could also be addressed but were not reachable by the bandwidth of our AOM at the chosen 50 G field.

After performing the proper sequence of optical pumping pulses to transfer the population to the desired ground m_F state, we perform OSG and absorption imaging to test the result of the optical pumping. As mentioned in Section 5.7.2, the OSG requires that we evaporatively cool the atoms to less than about 300 nK. However, in such a low trap the recoil from the optical pumping can rapidly deplete atoms from the trap. For this reason we perform most of the optical pumping sequence at a higher trap depth. While we do pump population from four of the non-target states into the target state at this higher trap, we retain one state with its population unchanged by any optical pumping. The purpose of retaining this "sacrificial" state is to provide non-identical particles with which the target state can collide, enabling evaporative cooling in the sample of fermionic Yb even after some pumping has taken place. After evaporation to the trap depth at which we reach the ≈ 500 nK level, we blast the atoms in the sacrificial state using a resonant blast with all six MOT beams. At last we check the result of the optical pumping sequence by performing OSG and absorption imaging. The timescales required to accomplish one stage of the optical pumping are shown in Figure 5.10.

5.7.4 Alternative Polarization Test: Green Blast Resonances

For much of the experiments in the following section, we preferred to use our typical side imaging system to probe the atoms. But doing so would prevent us from being able to consistently check the efficacy of the optical pumping steps used to prepare the sample in the proper spin state because the OSG signal can only be viewed with vertical imaging. For this reason we sometimes relied on an alternative method as a quick check on the spin polarization. This method basically involved performing a quick blast resonance like that in Figure 5.9. The fraction of the total atoms lost when the blasting light is resonant with each of the eight excited state transitions can be analyzed to approximate the spin distribution as follows: when the blasting light is resonant with the $m'_F = +^7\!/_2$ state, only atoms in the $m_F = +^5\!/_2$ state will be removed from the trap. From this number we determine the number of atoms in $m_F = +^5\!/_2$. Whereas when the blasting light is resonant with the $m'_F = +^5\!/_2$

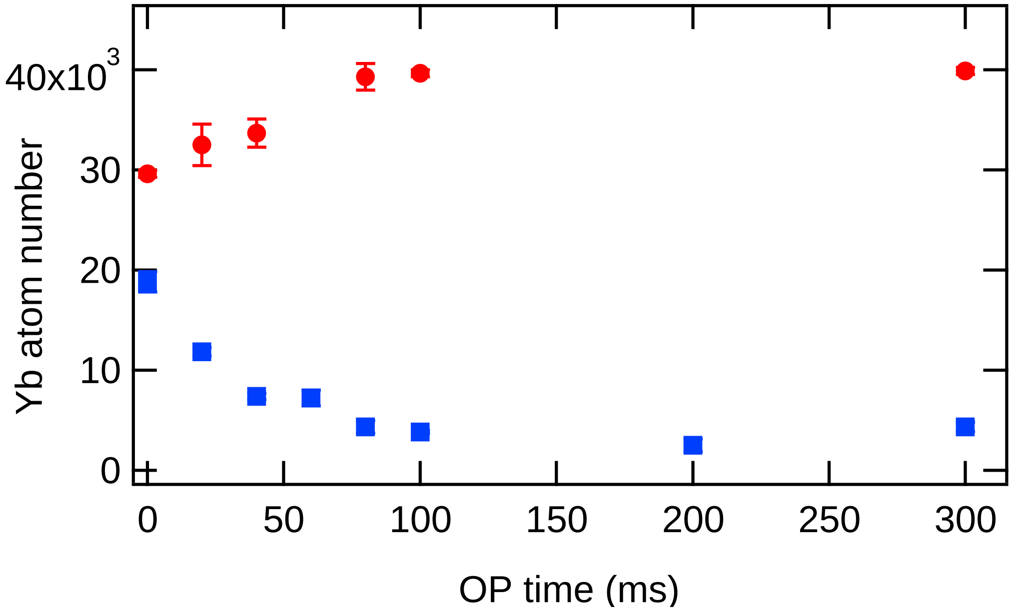

Figure 5.10: The typical timescale for optical pumping. In this plot we have determined as an example the number of atoms in states $m_F = -{}^5\!/\!{}_2$ (blue squares) and $m_F = -{}^3\!/\!{}_2$ (red circles) after optical pumping is applied with σ^- and σ^+ beams tuned to resonance with the $m'_F = -{}^3\!/\!{}_2$ state. The number in each state is determined through selective analysis of the absorption image after OSG: we determine by eye a region of interest that contains atoms which appear to belong to one single state and count the atoms in it with our usual integration method. For this data, the intensity in a single MOT beam was approximately 74 $^{\mu\mathrm{W}}\!/\!_{\mathrm{cm}^2}$, corresponding to a saturation parameter $s \approx 0.5$.

state, only atoms in $m_F = +5/2, +3/2$ states will be removed. Thus, the amount removed in the second case minus the amount removed in the first case constitutes the number of atoms in $m_F = +3/2$. Repeating the blast resonance for all eight excited states can then give you the population of each ground state through iterative subtraction.

5.8 *First Observation of MFR in Yb+Li*

5.8.1 Trap-Loss Spectroscopy Method

The capstone result of this thesis is the observation of magnetic Feshbach resonances between Yb and Li. In this work, the signature of heteronuclear Feshbach resonances is the observation of rapid loss from the trap through inelastic, exothermic collisions which are enhanced in the vicinity of an MFR [171, 197, 198].

The procedure for observation of MFRs through trap-loss spectroscopy can be roughly divided into two phases: the preparation phase followed by the spectroscopy phase. Since the spectroscopy phase is necessarily destructive to the ultracold atomic mixture, a new sample must be prepared for every variation in the magnetic field, which is our independent variable.

A brief description of the preparation step follows: laser-cooled ^{173}Yb atoms are captured in a crossed ODT composed of two focused laser beams at 1064 nm, remaining in an approximately even spin mixture of all six ground states. Laser-cooled ^{6}Li are subsequently loaded into the trap and allowed to thermalize with the colder ^{173}Yb at about $20\,\mu$K. Just after loading, the Li atoms are optically pumped into $|F\rangle = |\frac{1}{2}\rangle$. A large magnetic field is applied which allows us to remove the $|m_s, m_I\rangle = |-\frac{1}{2}, +1\rangle$ atoms through a frequency resolved resonant light pulse, leaving the Li sample entirely in the $|m_s, m_I\rangle = |-\frac{1}{2}, 0\rangle$. Forced evaporative cooling of Yb is performed by lowering the intensity of the ODT laser and Li is cooled sympathetically. When the temperature of both species has reached about $10\,\mu$K, the reduction in intensity is paused and the Yb spin population is manipulated via optical pumping on the $^1S_0 \rightarrow {}^3P_1$ transition in a $50\,$G bias field, individually addressing the resolved excited states with a mixture of σ^+ and σ^- polarizations. Typically, a “target state” is chosen for the majority of the population to be transferred to by pumping, while a small amount of the population remains in the "sacrificial state." The sacrificial state is retained to serve as a scattering partner for the "target state" during a second stage of evaporation. In most of this work, the atoms are cooled to a temperature of about $1\,\mu$K by further reducing the intensity of the trap. In the final stage of the preparation, the sacrificial state is removed from the trap through a resolved resonant light pulse.

After preparation the Li atoms are in $|m_s, m_I\rangle = |-\frac{1}{2}, 0\rangle$ and the Yb atoms are in a single nuclear spin state with at least 90% purity at around $1\,\mu$K. The spectroscopy phase begins when the field is ramped to a fixed magnetic field and held for 4 seconds. The field is then reduced to about 500 G and absorption imaging is performed on Li, principally recording the number of atoms remaining in the trap. This method suffices to roughly locate the resonance location, but it is susceptible to a slight asymmetry arising from the finite time needed to reach the target magnetic field. The mechanism of this asymmetry and the methods we have used to mitigate it are described in Section 5.9.2. We iterate the combination of preparation and spectroscopy, changing the holding field each time.

5.8.2 Observation at Predicted Locations

After discussing the experimental strategy for observing MFRs with our apparatus, the final consideration is the field at which these resonances are expected. The single ground electronic state in the YbLi system ($^2\Sigma$) makes the location of these resonances easy to understand in theory. Loosely bound vibrational states in the ($^2\Sigma$) electronic potential will exhibit the same splitting in the magnetic field as the Yb+Li atom pair because any coupling of the constituent spins to the nuclear motion is typically very weak for loosely bound states. Thus, as seen in Figure 5.11(a), the MFRs in this system can occur when the high field seeking atomic states intersect the low field seeking molecular states. These states shift relative to each other at a rate of $2\,\mu_B$. Therefore, to determine the rough location of the MFRs, it is sufficient to know the energy separation of the atomic and molecular states at zero field. The energies of these states was determined by our theory collaborators at Temple University by using the potential from our work in [114] to find the bound states of ^{173}Yb^{6}Li. Finer prediction of the field required only the additional consideration of the splitting between the Li hyperfine states and the selection rules determined by the coupling mechanisms. In Figure 5.11(a) we mark the location of three MFRs corresponding to coupling mechanism II, one for each Li hyperfine state in the high field seeking manifold.

We use the method of trap-loss spectroscopy to observe each MFR indicated by triangles in Figure 5.11(a). The spectrum is shown in one plot in Figure 5.12, with colored symbols matching those in Figure 5.11(a), though it should be noted that the sample preparation step was changed for each data set such that the sample was prepared in the appropriate Li hyperfine state for each experiment.

We also performed a search for the resonances in this area which were predicted to arise from coupling mechanism I, however we found that these resonances were too weak to be observed with our current experimental setup. Further improvements to the apparatus such as the loading of the atomic mixture into a deep optical lattice or a reduction of our magnetic field noise may make their observation possible, though as they are much narrower than the coupling mechanism II resonances, they may not be of much experimental interest.

We also investigated the dependence of these interspecies MFRs on the spin state of ^{173}Yb. We repeated our trap-loss spectroscopy measurements this time always preparing Li in $|2\rangle$ but changing the state in which we prepare the Yb. The results are shown in Figure 5.13. Five of the six ground states exhibit a resonant loss feature, indicating that these five states have a magnetic field-controlled scattering resonance with ^{6}Li in the $|2\rangle = |F = 1/2, m_F = -1/2\rangle$ state. This is an expected consequence of the selection rule associated with coupling mechanism II:

$$m_{F,\mathrm{Li}}^{\mathrm{final}} - m_{F,\mathrm{Li}}^{\mathrm{initial}} = \pm 1 \text{ and } m_{I,\mathrm{Yb}}^{\mathrm{final}} - m_{I,\mathrm{Yb}}^{\mathrm{initial}} = \mp 1$$

Since the only available crossings are characterized by $m_{F,\mathrm{Li}}^{\mathrm{final}} - m_{F,\mathrm{Li}}^{\mathrm{initial}} = +1$ only $m_{I,\mathrm{Yb}} = -5/2$ exhibits no resonance.

Of the five Yb nuclear spin states that exhibit an MFR, each is shifted relative to the

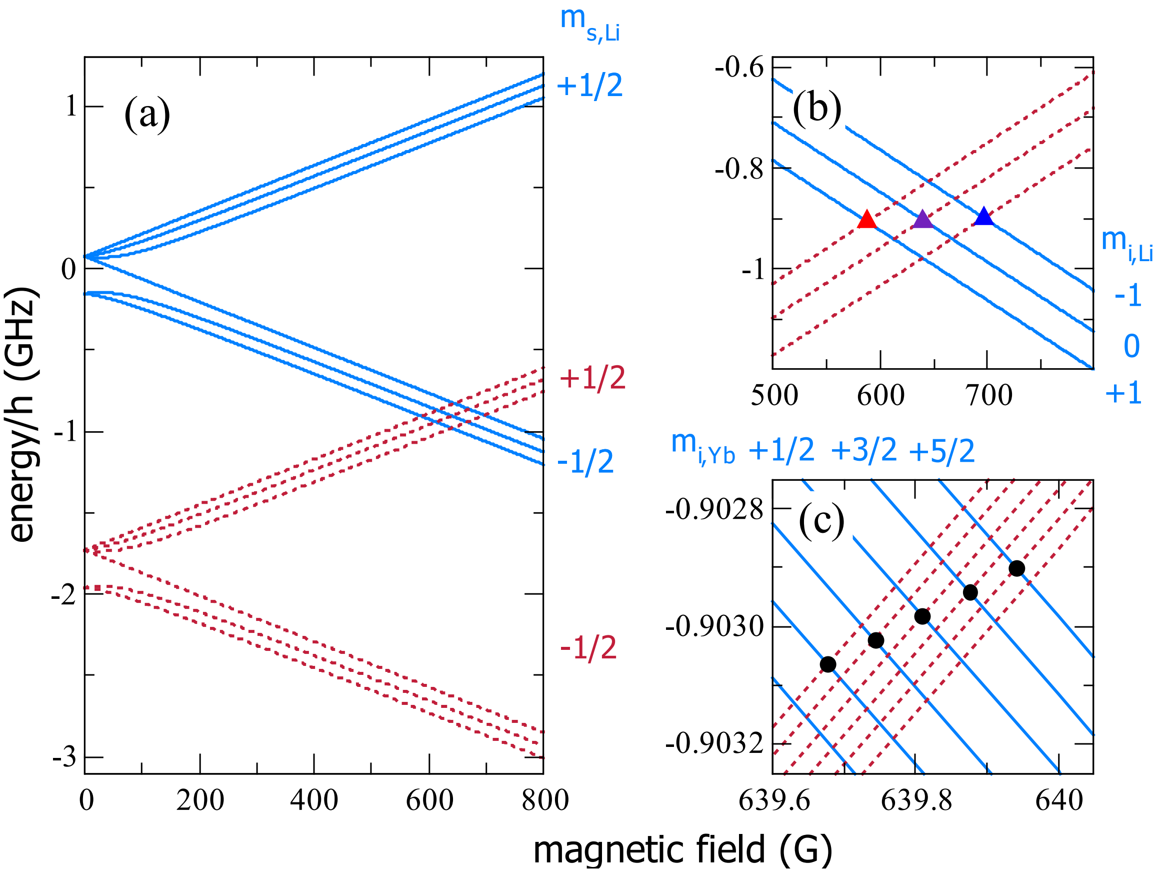

Figure 5.11: Energies of the Yb+Li atomic state (solid blue) and the YbLi molecular state of interest for this work (dashed red) as a function of magnetic field. The crossings visible in (a) are focused on in (b). Colored triangles indicate the location of Feshbach resonances caused by coupling mechanism II. (c) shows the level crossing for the Li $|F = {}^1\!/\!_2, m_F = -{}^1\!/\!_2\rangle$ state with the six different Yb m_I states which is not resolvable in (b) and circles are used to indicate crossings that would lead to a s-wave MFR.

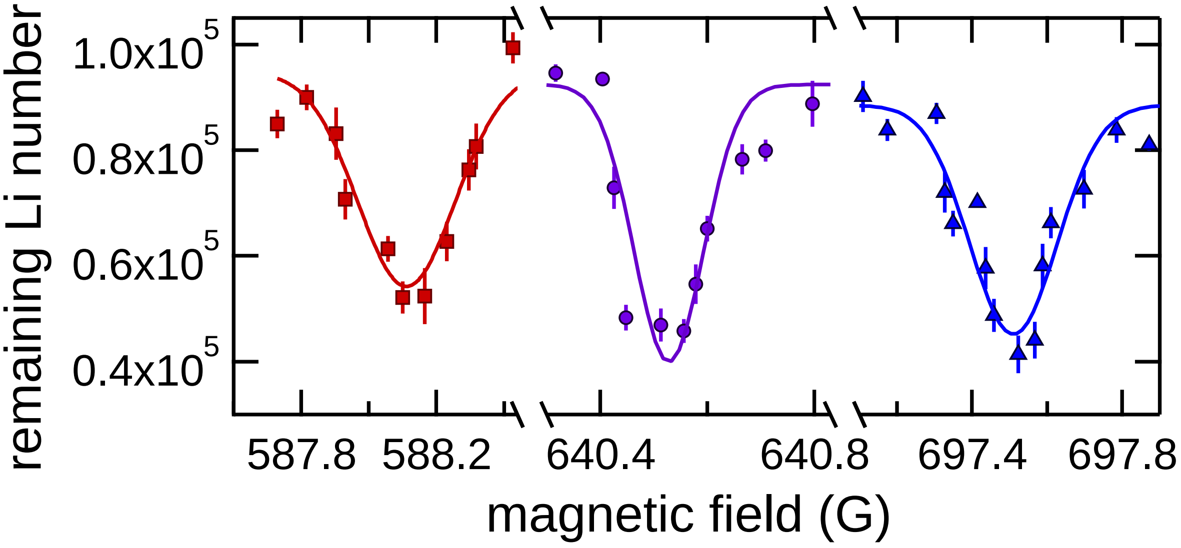

Figure 5.12: First observation of MFRs in ground state YbLi. In all cases the Yb sample was prepared in $m_{i,\mathrm{Yb}} = +5/2$. The Li was prepared in $|1\rangle$ (red squares), $|2\rangle$ (purple circles) or $|3\rangle$ (blue triangles). The sample was held at field for 4 seconds.

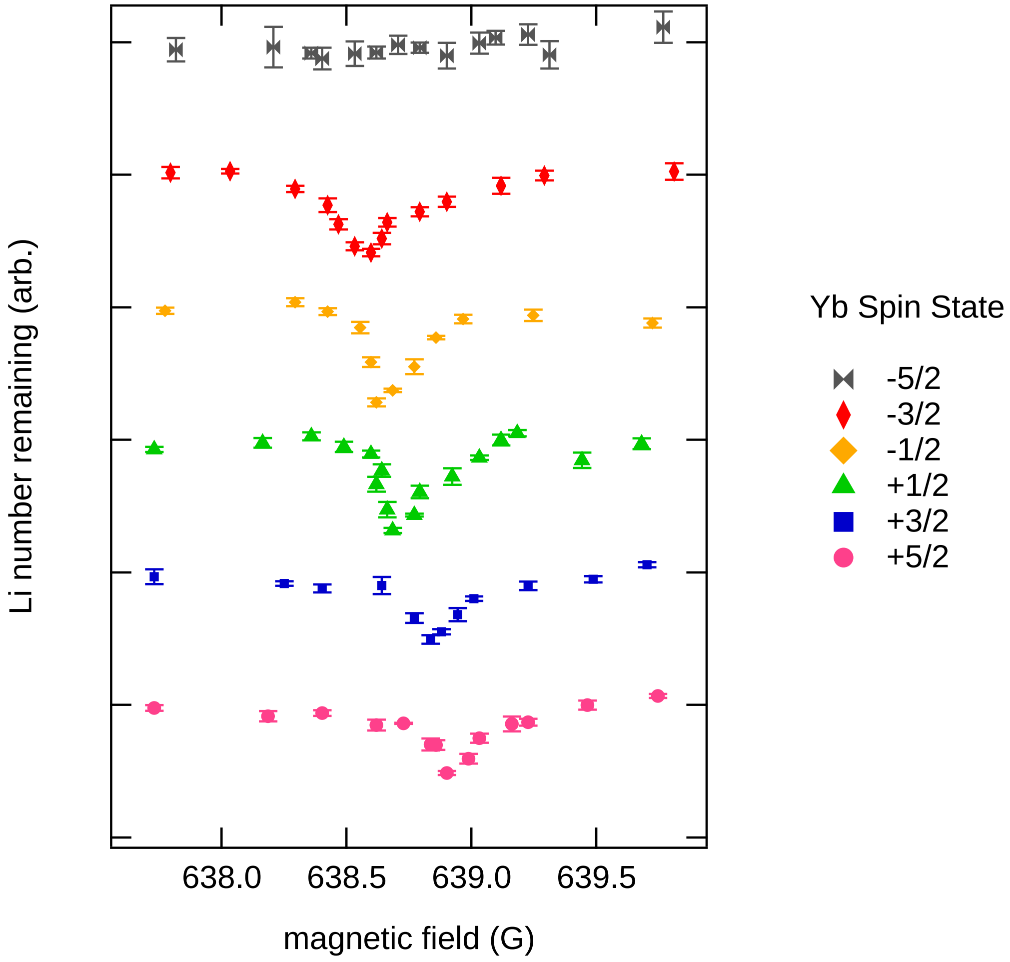

Figure 5.13: MFRs in each Yb nuclear spin state, $m_{I,\mathrm{Yb}}$. In all cases, Li was prepared in $|2\rangle$. The atoms were held at the target field for 1.5 seconds. The Li temperature was 1.8 μK and the Yb temperature was 1.0 μK.

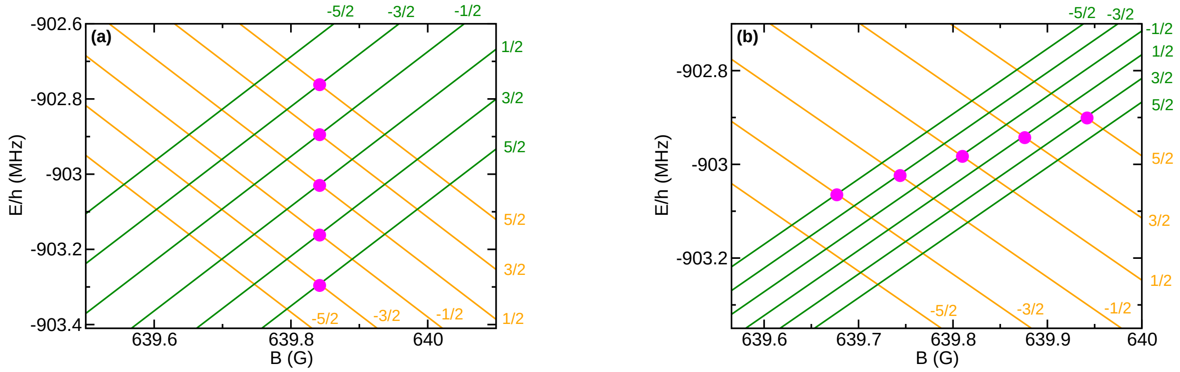

Figure 5.14: The energy levels of the relevant atomic (yellow) and molecular (green) states in the vicinity of the MFR between ^{173}Yb and ^{6}Li in the $|2\rangle$ state. Each state is labeled with the value of $m_{I,\mathrm{Yb}}$. In both plots the atomic states are separated according to the linear nuclear Zeeman shift. In (a) the molecular states are plotted as if the hyperfine interaction term responsible for the MFRs is zero. In (b), the states are plotted including the effect of this term. These plots were provided by Hui Li, working in the Kotochigova group at Temple University. Pink circles represent the location of MFRs.

next by $\sim 100\,\mathrm{mG}$ as seen in Figure 5.13. To understand the origin of this shift, consider Figure 5.14. If we assume that the Zeeman shift coming from the Yb nuclear spin within the loosely bound molecule is the same as that of the free Yb atom, then all five resonances would occur at the same magnetic field. However, if the Yb nucleus inside the molecule has an effective magnetic moment that is different than that of the free atom, the resonances will appear shifted relative to each other. In the case of the resonance studied in Figure 5.13 and 5.14 the effective magnetic moment of the Yb nucleus inside the molecule is larger in magnitude and of the opposite sign as that of the free atom. This means that the magnetic moment of the Yb nucleus inside the YbLi molecule has the opposite sign as that of the free Yb atom.

The effective magnetic moment of the Yb nucleus inside the molecule depends on the

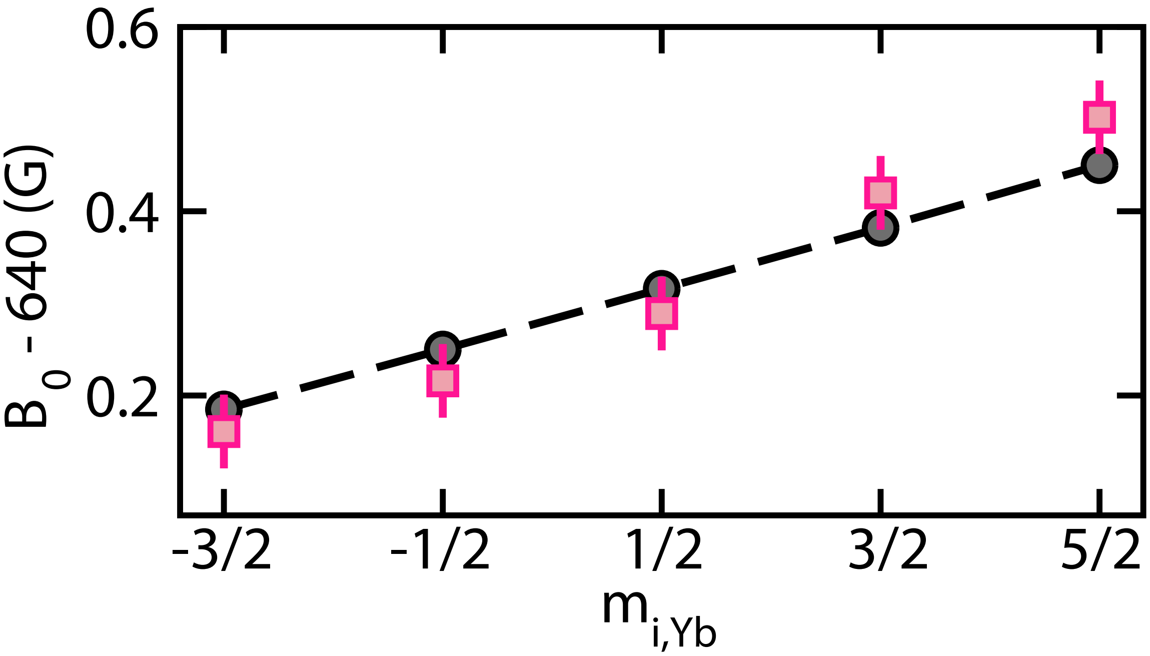

Figure 5.15: MFR location for each Yb ground hyperfine state. We determine the location of the magnetic Feshbach resonance by performing Gaussian fits on our spectra in Figure 5.13. The location of each resonance is plotted with pink squares. The slope of the dashed line is determined by theoretical calculation of the effective magnetic moment of the Yb nucleus inside the molecule, provided by Hui Li and our theory collaborators at Temple University. The gray circles are the expected locations of resonances based on this calculation, provided that the absolute measurement of the binding energy of the $v = -1$ molecule can be shifted within the uncertainty.

strength of the hyperfine interaction referred to as coupling mechanism II. Working with our collaborators at Temple University, we have compared the relative shift of the five resonances with the theoretically predicted relative shift using the nonrelativistic configuration valence bond (CI-VB) method. The results of this comparison are shown in Figure 5.15. The theoretical prediction fits well to the experimental data. A best fit line to the experimental data yields a differential shift of 0.088 ± 0.013 G per Zeeman state. The experimental and theoretical shifts are in agreement, assuming a 10% error on the theoretical shift.

5.9 Magnetic Field Calibration

5.9.1 overview of the data collection method

The data presented in Section 5.8 is plotted with the value of the magnetic field on the horizontal axis. However, we do not obtain direct measurements of the magnetic field to which the atoms are exposed using any sort of commercial, manufacturer-calibrated probe principally because such a device cannot be placed in close enough proximity to the atoms on account of the vacuum chamber. We instead assume the following:

- the magnetic field produced by our Helmholtz coils is a linear function of the current supplied to the coils
- any additional magnetic field not produced by our Helmholtz coils is constant

The extent to which these assumptions are only approximately true is described later.

We produce plots of the atom number vs. field by first collecting the atom number vs. the current supplied to the coils (measured by the Hall Probe) and then converting the current to a field relying on the above assumptions. Specifically, we assume that

$$B = B_0 + \alpha V_{HP} \tag{5.18}$$

where B is the magnetic field in Gauss, and V_{HP} is the reading of the Hall probe, itself proportional to the current in the coils. The Hall probe provides an inductive measure of the current and is placed around the 000 gauge wire connecting the power supply to the Helmholtz coils at the return side. B_0 and α are determined through calibration, with B_0 depending on the sum of all fields at the atoms which are not produced by the Helmoltz coils (we assume that to a good approximation this background field points in the same direction of the Helmholtz coils). α is dependent on the conversion factor of the Hall probe and the size and number of windings of the coils, in addition to their distance from the atoms.

By reading V_{HP} for all data collected, we need only determine values for α and B_0 to determine the field at each data point.

5.9.2 methods of calibration

To determine the values of α and B_0 we perform various field-dependent spectroscopies on the atoms in our trap. These spectroscopies either have a precisely known relation to the magnetic field through calculation from fundamental constants or have simply been repeated by multiple research groups, providing a precise average against which our results can be normalized. Below is a description of the methods we have used, along with some sample calibration data.

RF resonances. A reliable and commonly used method is to perform RF spectroscopy to probe the energy difference between states within the hyperfine ground manifold of Li. Within the $F = 1/2$ state in particular, the frequency of an observed resonance is a reliable probe because the Breit-Rabi formula provides an exact analytical solution to the energy splitting and all relevant constants are known to high accuracy.

We perform these RF measurements using the RF antenna installed at the base of our vacuum chamber, connected to our RF source via a BNC feedthrough (see [199]). When searching for such RF resonances we perform a coarse search followed by a fine search. Both searches begin with Li atoms in the optical trap at a temperature of about 15 μK. Yb is also present in the trap. We program the magnetic field control electronics to hold at a fixed field for the duration of the pulse and use any previous calibration to roughly predict the RF resonance frequency. For the coarse search we apply an RF pulse of 50 ms in length which

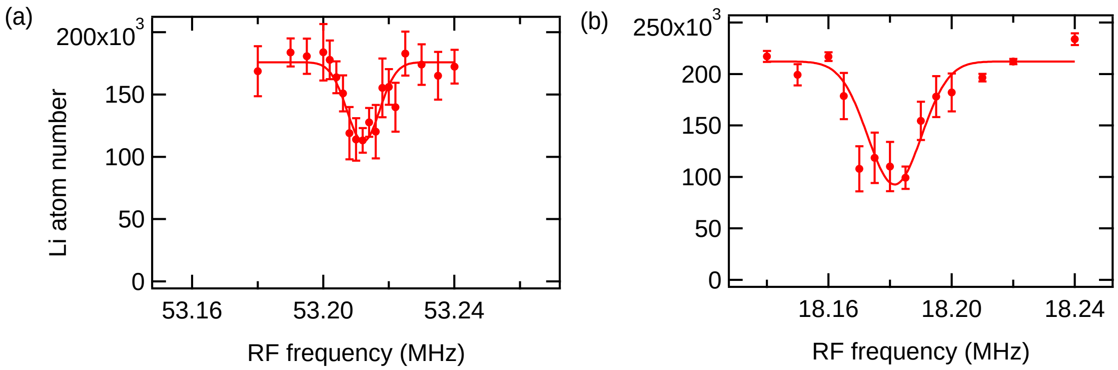

Figure 5.16: Sample data for the RF resonance between states 1 and 2. (a) taken at 77.52 G and (b) taken at 19.98 G.

sweeps the field in a single sawtooth over a frequency range of 50 or 100 kHz, centered on the predicted value. The resulting number of atoms in the trap is measured using a typical high-field absorption imaging process. We repeat this with different values of the frequency sweep center until we observe a loss from $|2\rangle$, the state in which we always begin. Within this loss feature, we perform the same procedure with a narrower frequency sweep: 5 to 10 kHz. Finally, we perform a fine scan by using a pure RF tone and apply a pulse of 25 ms, stepping the pulse through different values and recording the number remaining each time. A typical RF power for this final step is 200 mW. See Figure 5.16 for a representative sample of fine RF resonance scans.

This method is limited to use at low fields because the energy splitting between the two $F = {}^1\!/_2$ states becomes a weak function of field as the electronic and nuclear spins decouple from each other. This is quantified in Figure 5.17(b). Further evidence for the limitation at high field can be seen in Figure 5.16 where instability in the magnetic field is imprinted onto the RF resonance to a greater magnitude at lower fields in the form of a larger RF resonance width. In some cases the amount of data we collect in low field is not sufficient to average out long term drifts in the field resulting in RF resonances that have a flattened bottom in the average. In practice we find that at fields larger than about 100 G we need a level of accuracy on those resonance measurements which is not easily achieved on our apparatus. Beyond the issue of accuracy, this method is only useful up to about 150 G at which point a typical error on the RF resonance measurement of $\sim 1\,\mathrm{kHz}$ translates to a magnetic field precision beyond the precision at which we can presently measure the corresponding current (20 mG).

In the future it would be beneficial to extend the RF resonance calibration to higher fields by performing spectroscopy between the $F = 1/2$ and $F = 3/2$ states, such as between $|2\rangle$ and $|5\rangle$. This will require a change to the RF source typically used for this spectroscopy for which there are plans underway at the writing of this thesis.

comparison with known magnetic Feshbach resonances. There are three narrow Feshbach resonances ($< 150\,\mathrm{mG}$ width) between different combinations of the Li ground hyperfine states $|1\rangle$ and $|2\rangle$ which have been reported in multiple articles with high precision [200, 201]. We observed these three resonances using a trap-loss spectroscopy technique similar to that in Section 5.8 and used the reported values to calibrate our field against the literature. The only material difference between our method of trap-loss spectroscopy in the Li_2 calibration measurements and the YbLi MFR observations in Section 5.8 is the ordering of the magnetic field ramps used to reach the field targeted for each point in the spectroscopy. Because the Li_2 MFRs are much stronger than the YbLi MFRs, even crossing the resonant field in the course of a rapid ramp up to the target field can result in appreciable atom loss, resulting in asymmetric loss lineshapes. To solve this problem, we added extraneous ramps to offset fields about 20 G away from the target field and arranged these extraneous ramps such that the whole series of magnetic field ramps went over the resonant field exactly three times no matter if the target field was higher or lower than the resonant field. This depressed the apparent off-resonant atom number but did so uniformly.

"green blast resonances": spectroscopy of the Yb $^3P_1$ state. We perform spectroscopy on the relatively narrow $^1S_0 \rightarrow {}^3P_1$ transition in Yb. We probe this transition through

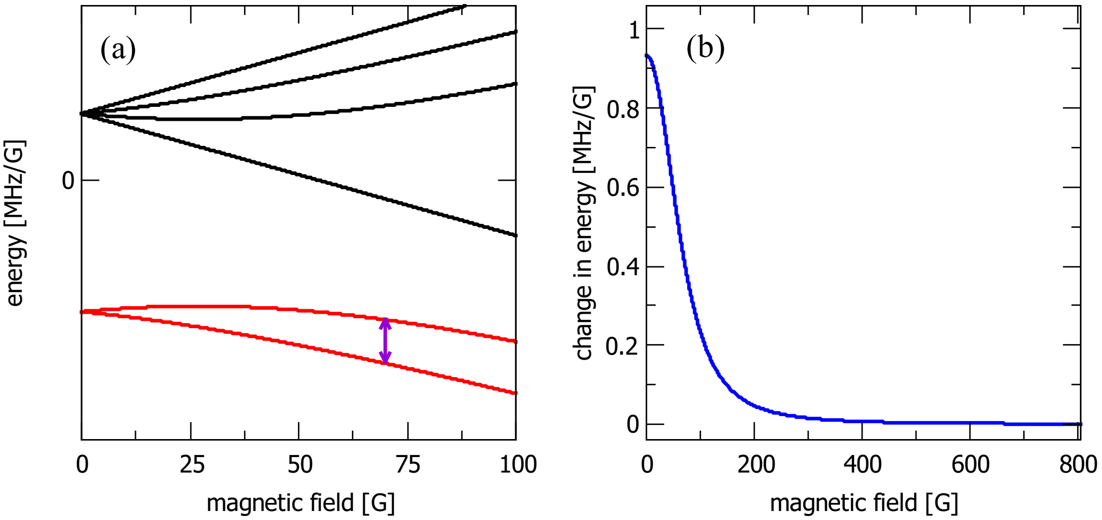

Figure 5.17: The energy splitting probed through RF spectroscopy used for field calibration. In (a) red lines indicate the energies of states 1 and 2 and the purple arrow provides a schematic example of the energy probed in one RF resonance measurement. See Figure 2.3 for more details on the state labelling. (b) plots the derivative of the energy difference between states 1 and 2.

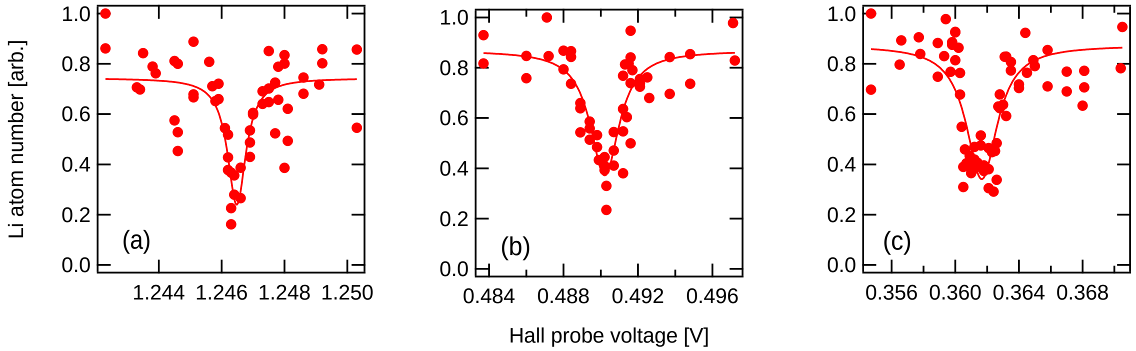

Figure 5.18: Observation of MFRs in Li_2 via trap-loss spectroscopy. These were done in a 5 W trap using 0.5 V of painting. An optimal holding time was chosen separately for each data set (ranging from 70 to 800 ms), depending on the strength of the resonance and the density of the atomic sample at the beginning of the spectroscopy phase. (a) a s-wave resonance between states 1 and 2 at about 543 G, (b) p-wave resonance between state 2 and state 2 at about 215 G, (c) p-wave resonance between states 1 and 1 at around 159 G.

a "blast resonance" for which we apply a fixed duration square pulse of light near the transition at 556 nm to atoms held in ODT and measure the fraction of atoms remaining in the ODT through absorption imaging. With the atoms held at a fixed bias field, we repeat the measurement multiple times, changing the blasting frequency to address multiple hyperfine state within the $^3P_1$ manifold. The splitting of the resonance into different hyperfine states can then be compared to the predicted splitting based on the magnetic moment of $^3P_1$ state (the shift of the $^1S_0$ ground state being $\sim$ 1000 times smaller is irrelevant for this measurement). This method is very similar to that used in Section 5.7 to determine the frequencies for optical pumping with green light.

We repeat this blast resonance spectroscopy at a variety of fields and track the change in the location of each resonance. Calibration of the magnetic field using these measurements should always use the splitting between states, rather than the shift of a single hyperfine state because the shift of a single state has been shown to deviate from the expected shift

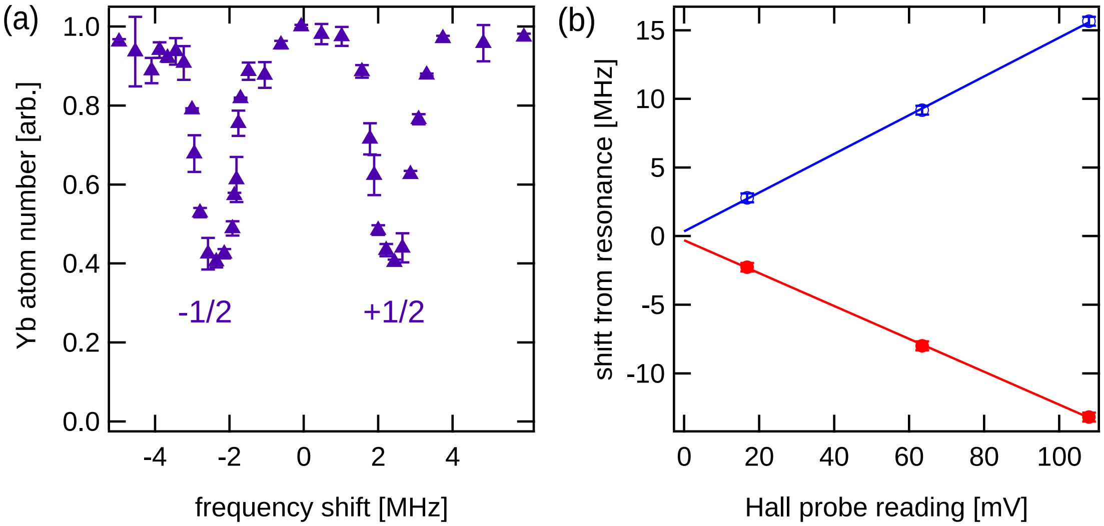

Figure 5.19: Spectroscopy of the Yb $^3P_1$ state for field calibration. (a) A sample "blast resonance" spanning the m_F' states $\pm 1/2$. This blast resonance was taken at 8.85 G. (b) The shift from the zero field resonance is plotted for $m_F' = +1/2$ (red) and $m_F' = -1/2$ at three different fields.

based on calculation of the Zeeman shift from the nuclear g-factor [90]. If using only the $m_F = \pm 1/2$ states for this spectroscopy, this method works up to 50 G, limited by the tuning range of the MOT AOM used to control the blast frequency. The method could be extended to higher fields through the installation of additional AOMs or other methods to reach greater detunings from the zero field resonance at which the MOT beams are typically tuned.

5.9.3 quantifying error on calibration

We use our calibration data from $|1\rangle - |2\rangle$ RF resonances and Li_2 MFRs to find best fit values for α and δB_0. We attribute the error in α principally to the limited precision of the Hall probe used in the calibration (and in our data collection for the YbLi MFR study). We attribute the error in B_0 principally to variations in the ambient magnetic field over time. The general consequences of our calibration model are

- all measurements carry an uncertainty of at least δB_0, the error on B_0 (20 mG in our current calibration)
- higher fields are associated with higher uncertainty, accumulated from the error in α (relative error of 2.3×10^{-4} in our current calibration).
- at high fields, the error on relative shifts between closely spaced resonances are still roughly equal to δB_0

The results of the calibration model are presented in Section 5.9.4. From the above consequences and the calibration results, we say that the absolute uncertainty on the field in the vicinity of each resonances is 149 mG for $|1\rangle$, 161 mG for $|2\rangle$, and 174 mG for $|3\rangle$. However, when determining the spacing between adjacent $m_{i,\mathrm{Yb}}$ states for a given Li state we consider the uncertainty to be 20 mG.

Finally, it should be noted that all of our calibration methods are sensitive only to the scalar field. Our assumption that $B = B_0 + \alpha V_{HP}$ is only valid if stray fields point in the same

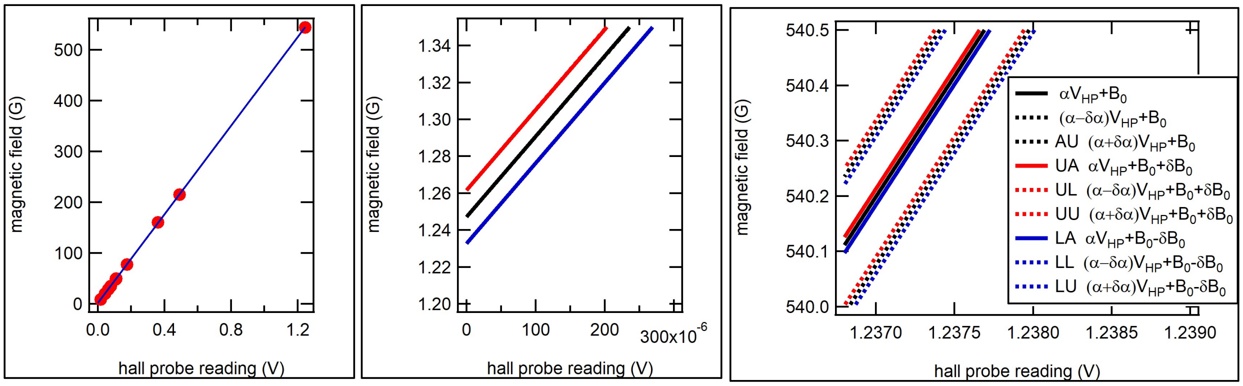

Figure 5.20: Calibration data and fit results. Red circles represent data points taken either through RF resonances between Li $|1\rangle$ and $|2\rangle$, measurements of known MFRs in Li between $|1\rangle$ and $|2\rangle$, or spectroscopy of the ${}^3P_1$ state of Yb. Multiple fit lines are shown. The best fit to the data is the solid black line. All other lines incorporate errors in the fit to demonstrate the affect such errors have on our certainty of the field. The two plots on the right demonstrate the effect of fit errors at low field (middle) and high field (right).

direction as the field produced by the coils. As a test on the robustness of our calibration, we assumed that a 2 G stray field was oriented perpendicular to the field produced by the Helmholtz coils. We refit a line to the calibration data and found that the values of α and B_0 changed by less that 0.01%.

5.9.4 calibration used for MFR study

We included results from three calibration methods - RF resonances, green blast resonances and comparison with Li$_2$ MFRs - to fit the data to the line $B = B_0 + \alpha V_{HP}$. The results of the fit are shown in Figure 5.20.

α [G/V]	error on α [G/V]	B_0 [G]	error on B_0 [G]
435.6924	0.1000	1.2471	0.0145

5.10 Temperature Dependence and MFR-induced Loss Model

The observations of MFRs in Section 5.8.2 relied on the enhancement of three-body loss from the trap near an MFR. In our work, both species are fermionic and spin polarized, meaning that two of the three scattering partners in such a process are identical fermions. Because the MFRs observed in this work are narrow compared to the residual kinetic energy at ultracold temperatures, we had a unique opportunity to study the effect of Fermi statistics on the temperature dependence of the three-body event rate coefficient $K(B, T)$. To study this, we collected trap-loss spectra for one MFR at a variety of different temperatures. The MFR chosen for this study was between Yb in the $m_{I,\mathrm{Yb}} = +{}^5\!/_2$ state and Li in the $|2\rangle$ state. To change the temperature of the atomic mixture, we controlled the final intensity of the ODT laser. In all cases, we performed forced evaporation on the mixture until it reached a temperature of $5.8\,\mu$K. To reach lower temperature, we continued the forced evaporation by lowering the ODT laser power further. To reach higher temperatures we "recompressed" the ODT by increasing the power, which reduced the volume of the gas and hence increased its temperature. As the temperature increased, the spectra became noticeably more asymmetric as seen in Figures 5.21(a)-(d). Though more subtle, the magnetic field at which the trap-loss is maximum also shifts to higher fields for higher temperatures.

Our theory collaborators constructed a model for the temperature dependence of $K(B, T)$ and used it as a fit to the trap-loss spectroscopy data in Figures 5.21(a)-(d) [202]. The agreement between the model and the data, combined with the model's explicit dependence on the particles' quantum statistics, confirms the expected p-wave threshold behavior near the resonance. A notable consequence of this model is that the maximum value of $K(B, T)$ is actually independent of temperature. This is in contrast to the Bose-Bose case for which the maximum value of $K(B, T)$ either decreases or increases with temperature depending on whether the threshold is s-wave or d-wave [186].

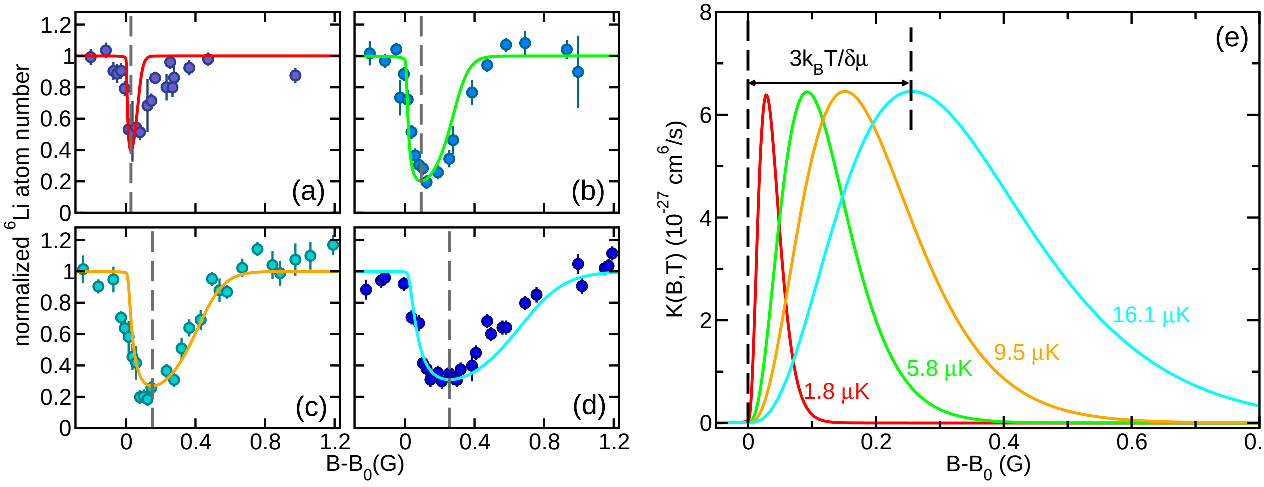

Figure 5.21: (a-d) trap-loss spectroscopy of the MFR between Yb in the $m_{i,\mathrm{Yb}} = +\frac{5}{2}$ state and Li in the $|2\rangle$ state, taken at different temperature. The measured temperature of the Li atoms was (a) 1.8 μK, (b) 5.8 μK, (c) 9.5 μK, and (d) 16.1 μK. Fitted theoretical line shapes are shown in solid lines. The field of maximum loss is marked in each plot with a dashed gray line. (e) the theoretical event rate coefficient as functions of $B - B_0$ for each temperature. The line colors correspond to those used in (a)-(d). Additional experimental detail for this figure can be found in [202].

Chapter 6

OUTLOOK

The work in this thesis has outlined in detail two possible paths for the coherent creation of YbLi molecules. While the two paths have respective advantages, both will require dynamical dressing that is adiabatic. We have determined that for YbLi, the adiabaticity requirements demand that the atoms be loaded pairwise into a 3D optical lattice. For molecule association with either strategy, the lattice serves two purposes. First, loading the atomic mixture into an optical lattice makes it easier to achieve adiabaticity by significantly reducing constraints on the dynamical timescale set by inelastic losses between molecules that are forming and un-associated atoms. Second, the boost in overlap density increases the coupling between atom and molecule, making the other technical constraints less demanding. Construction of the 3D optical lattice is underway at the time of this writing.

Pursuit of the StiRAP course has the advantage of being general: we could use it to make molecules composed of ^{6}Li plus any other easily cooled and trapped isotope of Yb, which would allow us to make fermionic molecules (^{174}Yb^{6}Li) or bosonic molecules (^{173}Yb^{6}Li) with the same method and equipment. In contrast, magneto-association requires the use of a fermionic isotope of Yb as only the fermionic isotopes have a nuclear spin and therefore strong MFR. For this reason, if we wish to make fermionic molecules, the isotope of Li will need to be changed to ^{7}Li, which requires time-consuming changes to the apparatus.

The lab is well prepared to attempt StiRAP again once loading atoms pairwise into the lattice is accomplished as we have already demonstrated the ability to create phase coherent pulses and to perform the necessary cleaning pulses between an associative StiRAP pulse and its dissociative reversal for the purposes of detection. Loading the atoms into a lattice where the density is much higher than in the ODT will allow us to achieve larger values

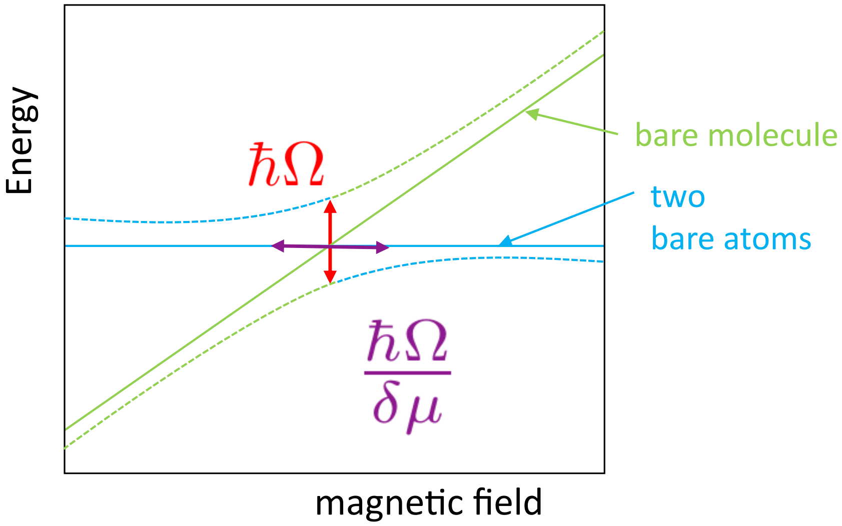

Figure 6.1: Atom-molecule coupling strength at a magnetic Feshbach resonance. The coupling strength sets the condition for adiabaticity in molecule formation sweeps. The size of the avoided crossing can be expressed in the same units as the magnetic field by dividing the coupling by the relative magnetic moment between the molecule and atom.

of Ω_{FB} without unrealistic increases in the FB laser intensity and will allow us to reduce the magnitudes of γ_g and γ_a. However, once these problems have been mitigated, further deleterious effects such as dynamic Stark shifts may need to be considered and possibly corrected for as in [135].

Because free-to-bound StiRAP has yet to be demonstrated in heteronuclear systems [135], we will first pursue the route which has been used successfully in the bi-alkali case by many groups and attempt magneto-association. While considerably narrower than the MFRs used for magneto-association in the past, the MFRs observed in this thesis may still be suitable for magneto-association. Recently, the method of magneto-association for atom pairs in a deep optical lattice was used to observe some evidence of molecule formation with a resonance only 8 μG wide [203]. However, additional technical upgrades will be required to control the magnetic field used to sweep across the MFR for magneto-association.

To understand the magnetic field stability that will be required to achieve efficient magneto-association, we quantify the atom-molecule coupling Ω (see Figure 6.1) in the following way [71, 204].

$$\hbar\Omega = \sqrt{\frac{\tilde{E_F}^{3/2} E_0^{1/2}}{3\pi^2}} \tag{6.1a}$$

$$\tilde{E_F} = \frac{6\pi^2 n^{2/3} \hbar^2}{m} \tag{6.1b}$$

$$E_0 = \frac{(\delta\mu\Delta)^2}{\hbar^2} m a_{bg}^2 \tag{6.1c}$$

where $\tilde{E_F}$ is the effective Fermi energy (applicable for both bosons and fermions) and E_0 is the energetic width of the MFR. $\delta\mu$ is the differential magnetic moment between the atomic and molecular states, m is the reduced mass, Δ is the bare resonance width, n is the atomic density and a_{bg} is the background s-wave scattering length.

In the case of YbLi, we have no experimental knowledge of Δ as the measurements made in this thesis were limited predominantly by thermal broadening but also by magnetic field instability. To perform these calculations, we rely on the theoretical width of the MFRs, $\Delta \approx 50\mu$G. For a_{bg}, we take the value measured in [114] and calculate the change from ^{174}Yb^{6}Li to ^{173}Yb^{6}Li to get $a_{bg} = 30.36\, a_0$ and we know that $\delta\mu = 2\mu_B$ and $m \approx 6$ a.m.u. This gives the following for the energetic resonance width.

$$\frac{E_0}{h} \approx 30\,\mu\text{Hz} \tag{6.2}$$

To calculate the effective Fermi energy, we calculate the on-site density for Yb in a lattice at 1070 nm noting from [204] that a good approximation of the coupling can be achieved using the more dense species for this calculation. We assume a typical lattice depth for Yb of $100\, E_r$ where E_r is the recoil energy $E_r = \dfrac{\hbar^2 k^2}{2m}$ with k being the wave vector of the lattice. We make the harmonic approximation to find the density: $n = \dfrac{\sqrt{6}}{2\pi^2} a_{\text{HO}}^{-3}$ with $a_{\text{HO}} = \dfrac{s^{-1/4}}{k}$

and $s = \dfrac{U}{E_r}$, the lattice depth in units of the photon-recoil energy. This gives the following for the effective Fermi energy.

$$\frac{\tilde{E_F}}{h} \approx 8.6\,\mathrm{MHz} \tag{6.3}$$

Putting the results for E_0 and $\tilde{E_F}$ into Equation 6.1a and using the appropriate value of $\delta\mu$ to convert this to magnetic field width we find the following.

$$\frac{\hbar\Omega}{\delta\mu} = 1.3\,\mathrm{mG} \tag{6.4}$$

Thus, in order to perform magneto-association of YbLi in a lattice, we will need to stabilize our magnetic field to the 1.3 mG level. To make this job easier, we will plan on using the MFR at the lowest field ≈ 600 G. This represents a stability of about 2 ppm. While this is challenging, it is not impossible as demonstrated in [205]. Development of the magnetic field stabilization electronics is also presently underway.

This thesis has explored two methods by which YbLi molecules could be coherently associated from atomic mixtures. The results presented here suggest good chances for the creation of these molecules after overcoming the challenges of pairwise lattice loading and magnetic field stabilization. Within striking distance of this goal, it is worth considering: what do we do if we succeed?

As mentioned in Section 2.1.1 collisions between trapped ultracold dimers remain poorly understood. Studies of YbLi are particularly well-suited to studying such collisions because unlike the other ultracold dimers studied in this context, its ground state magnetic moment may allow for control of these collisions through an intermolecular magnetic Feshbach resonance.

BIBLIOGRAPHY

[1] Cornell, E. A., Ensher, J. R. and Wieman, C. E. “Experiments in dilute atomic Bose-Einstein condensation.” *Proceedings of the International School of Physics Enrico Fermi*, 140, 15 (1998).

[2] Quèmèner, G. and Julienne, P. S. “Ultracold Molecules under Control!” *Chemical Reviews*, 112, 4949 (2012).

[3] Wolf, J., Deiß, M., Krükow, A., Tiemann, E., Ruzic, B. P., Wang, Y., D’Incao, J. P., Julienne, P. S. and Denschlag, J. H. “State-to-state chemistry for three-body recombination in an ultracold rubidium gas.” *Science*, 358, 6365, 921 (2017).

[4] Ye, X., Guo, M., González-Martínez, M. L., Quéméner, G. and Wang, D. “Collisions of ultracold ^{23}Na^{87}Rb molecules with controlled chemical reactivities.” *Science Advances*, 4, 1 (2018).

[5] Ospelkaus, S., Ni, K.-K., Wang, D., de Miranda, M. H. G., Neyenhuis, B., Quéméner, G., Julienne, P. S., Bohn, J. L., Jin, D. S. and Ye, J. “Quantum-State Controlled Chemical Reactions of Ultracold Potassium-Rubidium Molecules.” *Science*, 327, 5967, 853 (2010).

[6] Hu, M.-G., Liu, Y., Grimes, D. D., Lin, Y.-W., Gheorghe, A. H., Vexiau, R., Boulufa-Maafa, N., Dulieu, O. and Ni, K.-K. “Direct Observation of Ultracold Bimolecular Reactions.” *arXiv*, 1907.13628 (2019).

[7] Tomza, M. “Energetics and Control of Ultracold Isotope-Exchange Reactions between Heteronuclear Dimers in External Fields.” *Physical Review Letters*, 115, 063201 (2015).

[8] Kosicki, M. B., Żuchowski, P. S., González-Martínez, M. L. and Dulieu, O. “Product-state distribution after isotopic substitution in ultracold atom-molecule collisions.” *arXiv*, 1910.04263 (2019).

[9] Krems, R. “Cold controlled chemistry.” *Physical Chemistry Chemical Physics*, 10, 4079 (2008).

[10] Bohn, J. L., Rey, A. M. and Ye, J. “Cold molecules: Progress in quantum engineering of chemistry and quantum matter.” *Science*, 357, 6355, 1002 (2017).

[11] Park, J., Will, S. and Zwierlein, M. "Ultracold Dipolar Gas of Fermionic ^{23}Na^{40}K Molecules in their Absolute Ground State." *Physical Review Letters*, 114, 205302 (2015).

[12] Gregory, P. D., Frye, M. D., Blackmore, J. A., Bridge, E. M., Sawant, R., Hutson, J. M., Cornish, G., S. L. and Julienne, P. S. "Sticky collisions of ultracold RbCs." *Nature Communications*, 10, 3104 (2019).

[13] Mayle, M., Quéméner, G., Ruzic, B. P. and Bohn, J. L. "Scattering of ultracold molecules in the highly resonant regime." *Physical Review A*, 87, 012709 (2013).

[14] Croft, J. F. E. and Bohn, J. L. "Long-lived complexes and chaos in ultracold molecular collisions." *Physical Review A*, 89, 012714 (2014).

[15] Christianen, A., Zwierlein, M. W., Groenenboom, G. C. and Karman, T. "Photoinduced Two-Body Loss of Ultracold Molecules." *Physical Review Leters*, 123, 123402 (2019).

[16] Griesmaier, A., Werner, J., Hensler, S., Stuhler, J. and Pfau, T. "Bose-Einstein Condensation of Chromium." *Physical Review Letters*, 94, 160401 (2005).

[17] Baier, S., Mark, M. J., Petter, D., Aikawa, K., Chomaz, L., Cai, Z., Baranov, M., Zoller, P. and Ferlaino, F. "Extended Bose-Hubbard models with ultracold magnetic atoms." *Science*, 352, 6282, 201 (2016).

[18] Vogt, T., Viteau, M., Zhao, J., Chotia, A., Comparat, D. and Pillet, P. "Dipole Blockade at Förster Resonances in High Resolution Laser Excitation of Rydberg States of Cesium Atoms." *Physical Review Letters*, 97, 083003 (2006).

[19] Lahaye, T., Menotti, C., Santos, L., Lewenstein, M. and Pfau, T. "The physics of dipolar bosonic quantum gases." *Reports on Progress in Physics*, 72, 12, 126401 (2009).

[20] Barnett, R., Petrov, D., Lukin, M. and Demler, E. "Quantum Magnetism with Multicomponent Dipolar Molecules in an Optical Lattice." *Phyical Review Letters*, 96, 190401 (2006).

[21] Gorshkov, A. V., Manmana, S. R., Chen, G., Ye, J., Demler, E., Lukin, M. D. and Rey, A. M. "Tunable Superfluidity and Quantum Magnetism with Ultracold Polar Molecules." *Physical Review Letters*, 107, 115301 (2011).

[22] Kuns, K. A., Rey, A. M. and Gorshkov, A. V. "d-wave superfluidity in optical lattices of ultracold polar molecules." *Physical Review A*, 84, 063639 (2011).

[23] Yao, N. Y., Gorshkov, A. V., Laumann, C. R., Läuchli, A. M., Ye, J. and Lukin, M. D. "Realizing Fractional Chern Insulators in Dipolar Spin Systems." *Physical Review Letters*, 110, 185302 (2013).

[24] DeMille, D. "Quantum Computation with Trapped Polar Molecules." *Physical Review Letters*, 88, 067901 (2002).

[25] Soderberg, K.-A. B., Gemelke, N. and Chin, C. "Ultracold molecules: vehicles to scalable quantum information processing." *New Journal of Physics*, 11, 5, 055022 (2009).

[26] Park, J. W., Yan, Z. Z., Loh, H., Will, S. A. and Zwierlein, M. W. "Second-scale nuclear spin coherence time of ultracold ^{23}Na^{40}K molecules." *Science*, 357, 6349, 372 (2017).

[27] Kotochigova, S. and Tiesinga, E. "Controlling polar molecules in optical lattices." *Physical Review A*, 73, 041405 (2006).

[28] Yelin, S. F., Kirby, K. and Côté, R. "Schemes for robust quantum computation with polar molecules." *Physical Review A*, 74, 050301 (2006).

[29] Rabl, P., DeMille, D., Doyle, J. M., Lukin, M. D., Schoelkopf, R. J. and Zoller, P. "Hybrid Quantum Processors: Molecular Ensembles as Quantum Memory for Solid State Circuits." *Physical Review Letters*, 97, 033003 (2006).

[30] Andrè, A., DeMille, D., Doyle, J., Lukin, M. D., Maxwell, S. E., Rabl, P., Schoelopf, R. J. and Zoller, P. "A coherent all-elecrical interface between molecules and mesoscopic superconducting resonators." *Nature Physics*, 2, 636 (2006).

[31] Kaufman, A. M., Lester, B. J. and Regal, C. A. "Cooling a Single Atom in an Optical Tweezer to Its Quantum Ground State." *Physical Review X*, 2, 041014 (2012).

[32] Anderegg, L., Cheuk, L. W., Bao, Y., Burchesky, S., Ketterle, W., Ni, K.-K. and Doyle, J. M. "An optical tweezer array of ultracold molecules." *Science*, 365, 6458, 1156 (2019).

[33] Norcia, M. A., Young, A. W. and Kaufman, A. M. "Microscopic Control and Detection of Ultracold Strontium in Optical-Tweezer Arrays." *Physical Review X*, 8, 041054 (2018).

[34] Ni, K.-K., Rosenband, T. and Grimes, D. D. "Dipolar exchange quantum logic gate with polar molecules." *Chemical Science*, 9, 6830 (2018).

[35] Yu, P., Cheuk, L. W., Kozyryev, I. and Doyle, J. M. “A scalable quantum computing platform using symmetric-top molecules.” *New Journal of Physics*, 21, 9, 093049 (2019).

[36] Safronova, M. S., Budker, D., DeMille, D., Kimball, D. F. J., Derevianko, A. and Clark, C. W. “Search for new physics with atoms and molecules.” *Review of Modern Physics*, 90, 025008 (2018).

[37] Andreev, V., Ang, D. G., Doyle, J. M., Gabrielse, G., Haefner, J., Hutzler, N. R., Lasner, Z., Meisenhelder, C., O’Leary, B. R., Panda, C. D., West, A. D., West, E. P. and Wu, X. “Improved limit on the electric dipole moment of the electron.” *Nature*, 562, 355 (2018).

[38] Chin, C., Flambaum, V. V. and Kozlov, M. G. “Ultracold molecules: new probes on the variation of fundamental constants.” *New Journal of Physics*, 11, 5, 055048 (2009).

[39] DeMille, D., Sainis, S., Sage, J., Bergeman, T., Kotochigova, S. and Tiesinga, E. “Enhanced Sensitivity to Variation of m_e/m_p in Molecular Spectra.” *Physical Review Letters*, 100, 043202 (2008).

[40] Zelevinsky, T., Kotochigova, S. and Ye, J. “Precision Test of Mass-Ratio Variations with Lattice-Confined Ultracold Molecules.” *Physical Review Letters*, 100, 043201 (2008).

[41] Kotochigova, S., Zelevinsky, T. and Ye, J. “Prospects for application of ultracold Sr_2 molecules in precision measurements.” *Physical Review A*, 79, 012504 (2009).

[42] Kobayashi, J., Ogino, A. and Inouye, S. “Measurement of the variation of the electron-to-proton mass ration using ultracold molecules produced from laser-cooled atoms.” *Nature Communications*, 10, 3771 (2019).

[43] Flambaum, V. V., Stadnik, Y. V., Kozlov, M. G. and Petrov, A. N. “Enhanced effects of temporal variation of the fundamental constants in $^2\Pi_{1/2}$-term diatomic molecules: $^{207}Pb^{19}F$.” *Physical Review A*, 88, 052124 (2013).

[44] Salumbides, E. J., Koelemeij, J. C. J., Komasa, J., Pachucki, K., Eikema, K. S. E. and Ubachs, W. “Bounds on fifth forces from precision measurements on molecules.” *Physical Review D*, 87, 112008 (2013).

[45] Altuntaş, E., Ammon, J., Cahn, S. B. and DeMille, D. “Demonstration of a Sensitive Method to Measure Nuclear-Spin-Dependent Parity Violation.” *Physical Review Letters*, 120, 142501 (2018).

[46] Norrgard, E. B., Barker, D. S., Eckel, S., Fedchak, J. A., Klimov, N. N. and Scherschligt, J. “Nuclear-spin dependent parity violation in optically trapped polyatomic molecules.” *Communications Physics*, 2, 77 (2019).

[47] Metcalf, H. J. and van der Straten, P. Laser Cooling and Trapping. Springer-Verlag New York (1999).

[48] Di Rosa, M. D. “Laser-cooling molecules.” *The European Physical Journal D - Atomic, Molecular, Optical and Plasma Physics*, 31, 2, 395 (2004).

[49] McCarron, D. “Laser cooling and trapping molecules.” *Journal of Physics B: Atomic, Molecular and Optical Physics*, 51, 21, 212001 (2018).

[50] McCarron, D. J., Steinecker, M. H., Zhu, Y. and DeMille, D. “Magnetic Trapping of an Ultracold Gas of Polar Molecules.” *Physical Review Letters*, 121, 013202 (2018).

[51] Williams, H. J., Caldwell, L., Fitch, N. J., Truppe, S., Rodewald, J., Hinds, E. A., Sauer, B. E. and Tarbutt, M. R. “Magnetic Trapping and Coherent Control of Laser-Cooled Molecules.” *Physical Review Letters*, 120, 163201 (2018).

[52] Collopy, A. L., Ding, S., Wu, Y., Finneran, I. A., Anderegg, L., Augenbraun, B. L., Doyle, J. M. and Ye, J. “3D Magneto-Optical Trap of Yttrium Monoxide.” *Physical Review Letters*, 121, 213201 (2018).

[53] Collopy, A. L., Hummon, M. T., Yeo, M., Yan, B. and Ye, J. “Prospects for a narrow line MOT in YO.” *New Journal of Physics*, 17, 5, 055008 (2015).

[54] Railing, L., Shaw, J. and McCarron, D. “Progress towards laser-cooled CH molecules.” (2019). APS Division of Atomic, Molecular and Optical Physics APS Meeting.

[55] Kozyryev, I., Baum, L., Matsuda, K., Augenbraun, B. L., Anderegg, L., Sedlack, A. P. and Doyle, J. M. “Sisyphus Laser Cooling of a Polyatomic Molecule.” *Physical Review Letters*, 118, 173201 (2017).

[56] Kozyryev, I., Steimle, T. C., Yu, P., Nguyen, D.-T. and Doyle, J. M. “Determination of CaOH and CaOCH3 vibrational branching ratios for direct laser cooling and trapping.” *New Journal of Physics*, 21, 5, 052002 (2019).

[57] Moore, K., Lane, I. C., McNally, R. L. and Zelevinsky, T. “Assignment of excited-state bond lengths using branching-ratio measurements: The $B^2\Sigma^+$ state of BaH molecules.” *Physical Review A*, 100, 022506 (2019).

[58] Stuhl, B. K., Hummon, M. T., Yeo, M., Quèmèner, G., Bohn, J. L. and Ye, J. "evaporative cooling of the dipolar hydroxyl radical." *Nature*, 492, 396 (2012).

[59] Liu, Y., Vashishta, M., Djuricanin, P., Zhou, S., Zhong, W., Mittertreiner, T., Carty, D. and Momose, T. "Magnetic Trapping of Cold Methyl Radicals." *Physical Review Letters*, 118, 093201 (2017).

[60] Maxwell, S. E., Brahms, N., deCarvalho, R., Glenn, D. R., Helton, J. S., Nguyen, S. V., Patterson, D., Petricka, J., DeMille, D. and Doyle, J. M. "High-Flux Beam Source for Cold, Slow Atoms or Molecules." *Physical Review Letters*, 95, 173201 (2005).

[61] Hutzler, N. R., Lu, H.-I. and Doyle, J. M. "The Buffer Gas Beam: And Intense, Cold, Slow Source for Atoms and Molecules." *Chemical Reviews*, 112, 4803 (2012).

[62] van de Meerakker, S. Y. T., Bethlem, H. L., Vanhaecke, N. and Meijer, G. "Manipulation and Control of Molecular Beams." *Cemical Reviews*, 112, 4828 (2012).

[63] Cheuk, L. W., Anderegg, L., Augenbraun, B. L., Bao, Y., Burchesky, S., Ketterle, W. and Doyle, J. M. "Λ-Enhanced Imaging of Molecules in an Optical Trap." *Physical Review Letters*, 121, 083201 (2018).

[64] Hess, H. F. "Evaporative cooling of magnetically trapped and compressed spin-polarized hydrogen." *Physical Review B*, 34, 3476 (1986).

[65] Adams, C. S., Lee, H. J., Davidson, N., Kasevich, M. and Chu, S. "Evaporative Cooling in a Crossed Dipole Trap." *Physical Review Letters*, 74, 3577 (1995).

[66] Modugno, G., Ferrari, G., Roati, G., Brecha, R., Simoni, A. and Inguscio, M. "Bose-Einstein Condensation of Potassium Atoms by Sympathetic Cooling." *Science*, 294, 1320 (2001).

[67] Hu, J., Urvoy, A., Vendeiro, Z., Crépel, V., Chen, W. and Vuletić, V. "Creation of a Bose-condensed gas of 87Rb by laser cooling." *Science*, 358, 6366, 1078 (2017).

[68] Son, H., Park, J. J., Ketterle, W. and Jamison, A. O. "Observation of Collisional Cooling of Ultracold Molecules." (2019).

[69] Tscherbul, T. V., Kłos, J. and Buchachenko, A. A. "Ultracold spin-polarized mixtures of ${}^2\Sigma$ molecules with S-state atoms: Collisional stability and implications for sympathetic cooling." *Physical Review A*, 84, 040701 (2011).

[70] Lim, J., Frye, M. D., Hutson, J. M. and Tarbutt, M. R. “Modeling sympathetic cooling of molecules by ultracold atoms.” *Physical Review A*, 92, 053419 (2015).

[71] Köhler, T., Góral, K. and Julienne, P. S. “Production of cold molecules via magnetically tunable Feshbach resonances.” *Review of Modern Physics*, 78, 1311 (2006).

[72] De Marco, L., Valtolina, G., Matsuda, K., Tobias, W. G., Covey, J. P. and Ye, J. “A degenerate Fermi gas of polar molecules.” *Science*, 363, 6429, 853 (2019).

[73] Ospelkaus, S., Pe’er, A., Ni, K.-K., Zirbel, J. J., Neyenhuis, B., Kotochigova, S., Julienne, P. S., Ye, J. and Jin, D. S. “Efficient state transfer in an ultracold dense gas of heteronuclear molecules.” *Nature Physics*, 4, 622 (2008).

[74] Ni, K.-K., Ospelkaus, S., de Miranda, M. H. G., Peer, A., Neyenhuis, B., Zirbel, J. J., Kotochigova, S., Julienne, P. S., Jin, D. S. and Ye, J. “A High Phase-Space-Density Gas of Polar Molecules.” *Science*, 322, 231 (2008).

[75] Takekoshi, T., Reichsöllner, L., Schindewolf, A., Hutson, J., Le Sueur, C., Dulieu, O., Ferlaino, F., Grimm, R. and Nägerl, H.-C. “Ultracold dense samples of dipolar RbCs molecules in the rovibrational and hyperfine ground state.” *Physical Review Letters*, 113, 205301 (2014).

[76] Molony, P., Gregory, P., Ji, Z., Lu, B., Köppinger, M., Le Sueur, C., Blackley, C., Hutson, J. and Cornish, S. “Creation of Ultracold 87Rb133Cs Molecules in the Rovibrational Ground State.” *Physical Review Letters*, 113, 255301 (2014).

[77] Guo, M., Zhu, B., Lu, B., Ye, X., Wang, F., Vexiau, R., Bouloufa-Maafa, N., Quéméner, G., Dulieu, O. and Wang, D. “Creation of an Ultracold Gas of Ground-State Dipolar ^{23}Na^{87}Rb Molecules.” *Physical Review Letters*, 116, 205303 (2016).

[78] Rvachov, T. M., Son, H., Sommer, A. T., Ebadi, S., Park, J. J., Zwierlein, M. W., Ketterle, W. and Jamison, A. O. “Long-Lived Ultracold Molecules with Electric and Magnetic Dipole Moments.” *Physical Review Letters*, 119, 143001 (2017).

[79] Seeßelberg, F., Buchheim, N., Lu, Z.-K., Schneider, T., Luo, X.-Y., Tiemann, E., Bloch, I. and Gohle, C. “Modeling the adiabatic creation of ultracold polar ^{23}Na^{40}K molecules.” *Physical Review A*, 97, 013405 (2018).

[80] Stellmer, S., Pasquiou, B., Grimm, R. and Schreck, F. “Creation of Ultracold Sr_2 Molecules in the Electronic Ground State.” *Physical Review Letters*, 109, 115302 (2012).

[81] Voges, K. K., Gersema, P., Hartmann, T., Schulze, T. A., Zenesini, A. and Ospelkaus, S. “A pathway to ultracold bosonic ^{23}Na^{39}K ground state molecules.” (2019).

[82] Liu, L. R., Hood, J. D., Yu, Y., Zhang, J. T., Hutzler, N. R., Rosenband, T. and Ni, K.-K. “Building one molecule from a reservoir of two atoms.” *Science*, 360, 6391, 900 (2018).

[83] Barbé, V., Ciamei, A., Pasquiou, B., Reichsöllner, L., Schreck, F., Żuchowski, P. and Hutson, J. M. “Observation of Feshbach resonances between alkali and closed-shell atoms.” *Nature Physics*, 14, 881 (2018).

[84] Guttridge, A., Frye, M. D., Yang, B. C., Hutson, J. M. and Cornish, S. L. “Two-photon photoassociation spectroscopy of CsYb: Ground-state interaction potential and interspecies scattering lengths.” *Physical Review A*, 98, 022707 (2018).

[85] Deiglmayr, J., Grochola, A., Repp, M., Dulieu, O., Wester, R. and Weidemüller, M. “Permanent dipole moment of LiCs in the ground state.” *Physical Review A*, 82, 032503 (2010).

[86] “Commission on Isotopic Abundances and Atomic Weights: Ytterbium.” (2017).

[87] Sansonetti, J. E. and Martin, W. C. “Handbook of Basic Atomic Spectroscopic Data.” *Journal of Physical and Chemical Reference Data*, 34, 4, 1559 (2005).

[88] Kitagawa, M., Enomoto, K., Kasa, K., Takahashi, Y., Ciuryło, R., Naidon, P. and Julienne, P. S. “Two-color photoassociation spectroscopy of ytterbium atoms and the precise determinations of s-wave scattering lengths.” *Physical Review A*, 77, 012719 (2008).

[89] Das, D., Barthwal, S., Banerjee, A. and Natarajan, V. “Absolute frequency measurements in Yb with 0.08 ppb uncertainty: Isotope shifts and hyperfine structure in the $399-$nm $^1S_0 \rightarrow^1 P_1$ line.” *Physical Review A*, 72, 032506 (2005).

[90] Pandey, K., Singh, A. K., Kumar, P. V. K., Suryanarayana, M. V. and Natarajan, V. “Isotope shifts and hyperfine structure in the 555.8-nm $^1S_0 \rightarrow {}^3P_1$ line of Yb.” *Physical Review A*, 80, 022518 (2009).

[91] Foot, C. J. Atomic Physics. Oxford University Press (2005).

[92] Micheli, A., Brennen, G. K. and Zoller, P. “A Toolbox for Lattice-Spin Models with Polar Molecules.” *Nature Physics*, 2, 341 (2006).

[93] Herrera, F., Cao, Y., Kais, S. and Whaley, K. B. "Infrared-dressed entanglement of cold open-shell polar molecules for universal matchgate quantum computing." *New Journal of Physics*, 16, 7, 075001 (2014).

[94] Abrahamsson, E., Tscherbul, T. V. and Krems, R. V. "Inelastic collisions of cold polar molecules in nonparallel electric and magnetic fields." *The Journal of Chemical Physics*, 127, 4, 044302 (2007).

[95] Kotochigova, S., Petrov, A., Linnik, M., Klos, J. and Julienne, P. S. "Ab initio properties of Li-group-II molecules for ultracold matter studies." *Journal of Chemical Physics*, 135, 164108 (2011).

[96] Kotochigova, S. "private communication." Temple University.

[97] Hansen, A. H. "Interacting Quantum Gases of Lithium and Ytterbium." *PhD Thesis - University of Washington* (2011).

[98] Khramov, A. "Experiments in the Ultracold Lithium-Ytterbium." *PhD Thesis - University of Washington* (2013).

[99] Phillips, W. D. and Metcalf, H. "Laser Deceleration of an Atomic Beam." *Physical Review Letters*, 48, 596 (1982).

[100] Grimm, R., Weidemüller, M. and Ovchinnikov, Y. B. "Optical Dipole Traps for Neutral Atoms." volume 42 of *Advances In Atomic, Molecular, and Optical Physics*, 95 – 170. Academic Press (2000).

[101] Ivanov, V. V., Khramov, A., Hansen, A. H., Dowd, W. H., Münchow, F., Jamison, A. O. and Gupta, S. "Sympathetic Cooling in an Optically Trapped Mixture of Alkali and Spin-Singlet Atoms." *Physical Review Letters*, 106, 153201 (2011).

[102] Hansen, A. H., Khramov, A., Dowd, W. H., Jamison, A. O., Ivanov, V. V. and Gupta, S. "Quantum Degenerate Mixture of Ytterbium and Lithium Atoms." *Physical Review A*, 84, 011606(R) (2011).

[103] Roy, R., Green, A., Bowler, R. and Gupta, S. "Rapid cooling to quantum degeneracy in dynamically shaped atom traps." *Physical Review A*, 93, 043403 (2016).

[104] Demtröder, W. Molecular Physics. Wiley-VCH (2005).

[105] Sinanoğlu, O. Many-Electron Theory of Atoms, Molecules and Their Interactions. John Wiley & Sons, Ltd (2007).

[106] Cizek, J. and Paldus, J. “Coupled Cluster Approach.” *Physica Scripta*, 21, 3-4, 251 (1980).

[107] Zhang, P., Sadeghpour, H. R. and Dalgarno, A. “Structure and spectroscopy of ground and excited states of LiYb.” *Journal of Chemical Physics*, 133, 044306 (2010).

[108] Gopakumar, G., Abe, M., Das, B. P., Hada, M. and Hirao, K. “Relativistic calculations of ground and excited states of LiYb molecule for ultracold photoassociation spectroscopy studies.” *Journal of Chemical Physics*, 133, 124317 (2010).

[109] Kajita, M., Gopakumar, G., Abe, M. and Hada, M. “Elimination of the Stark shift from the vibrational transition frequency of optically trapped 174Yb6Li molecules.” *Physical Review A*, 84, 022507 (2011).

[110] Jones, K. M., Tiesinga, E., Lett, P. D. and Julienne, P. S. “Ultracold photoassociation spectroscopy: Long-range molecules and atomic scattering.” *Review of Modern Physics*, 78, 483 (2006).

[111] DeMille, D. “Diatomic molecules, a window onto fundamental physics.” *Physics Today*, 68, 127, 34 (2015).

[112] LeRoy, R. J. and Bernstein, R. B. “Dissociation Energy and Long-Range Potential of Diatomic Molecules from Vibrational Spacings of Higher Levels.” *The Journal of Chemical Physics*, 52, 8, 3869 (1970).

[113] Roy, R., Shrestha, R., Green, A., Gupta, S., Li, M., Kotochigova, S., Petrov, A. and Yuen, C. H. “Photoassociative production of ultracold heteronuclear YbLi* molecules.” *Physical Review A*, 94, 033413 (2016).

[114] Green, A., See Toh, J. H., Roy, R., Li, M., Kotochigova, S. and Gupta, S. “Two-photon photoassociation spectroscopy of the $^2\Sigma^+$ YbLi molecular ground state.” *Physical Review A*, 99, 063416 (2019).

[115] Wester, R., Kraft, S., Mudrich, M., Staudt, M., Lange, J., Vanhaecke, N., Dulieu, O. and Weidemüller, M. “Photoassociation inside an optical dipole trap: absolute rate coefficients and Franck–Condon factors.” *Applied Physics B*, 79, 8, 993 (2004).

[116] Prodan, I. D., Pichler, M., Junker, M., Hulet, R. G. and Bohn, J. L. “Intensity Dependence of Photoassociation in a Quantum Degenerate Atomic Gas.” *Physical Review Letters*, 91, 080402 (2003).

[117] Sakurai, J. J. Modern Quantum Mechanics. Addison-Wesley (1994).

[118] Gordon, R. G. "New Method for Constructing Wavefunctions for Bound States and Scattering." *The Journal of Chemical Physics*, 51, 1, 14 (1969).

[119] Hara, H., Takasu, Y., Yamaoka, Y., Doyle, J. and Y., T. "Quantum Degenerate Mixtures of Alkali and Alkaline-Earth-Like Atoms." *Physical Review Letters*, 106, 205304 (2011).

[120] Kampschulte, T. and Denschlag, J. H. "Cavity-controlled formation of ultracold molecules." *New Journal of Physics*, 20, 12, 123015 (2018).

[121] Reinaudi, G., Osborn, C. B., McDonald, M., Kotochigova, S. and Zelevinsky, T. "Optical Production of Stable Ultracold ^{88}Sr$_2$ Molecules." *Physical Review Letters*, 109, 115303 (2012).

[122] McDonald, M., McGuyer, B., Apfelbeck, F., Lee, C.-H., Majewska, I., Moszynski, R. and Zelevinsky, T. "Photodissociation of ultracold diatomic strontium molecules with quantum state control." *Nature*, 535, 122 (2016).

[123] Zabawa, P., Wakim, A., Haruza, M. and Bigelow, N. P. "Formation of ultracold $X\,^1\Sigma^+(v' = 0)$ NaCs molecules via coupled photoassociation channels." *Physical Review A*, 84, 061401 (2011).

[124] Banerjee, J., Rahmlow, D., Carollo, R., Bellos, M., Eyler, E. E., Gould, P. L. and Stwalley, W. C. "Direct photoassociative formation of ultracold KRb molecules in the lowest vibrational levels of the electronic ground state." *Physical Review A*, 86, 053428 (2012).

[125] Yan, M., DeSalvo, B. J., Huang, Y., Naidon, P. and Killian, T. C. "Rabi Oscillations between Atomic and Molecular Condensates Driven with Coherent One-Color Photoassociation." *Physical Review Letters*, 111, 150402 (2013).

[126] McGuyer, B. H., McDonald, M., Iwata, G. Z., Tarallo, M. G., Grier, A. T., Apfelbeck, F. and Zelevinsky, T. "High-precision spectroscopy of ultracold molecules in an optical lattice." *New Journal of Physics*, 17, 5, 055004 (2015).

[127] Kotochigova, S. "Prospects for Making Polar Molecules with Microwave Fields." *Physical Review Letters*, 99, 073003 (2007).

[128] Fox, M. Quantum Optics: An Introduction. Oxford University Press (2006).

[129] Bergmann, K., Theuer, H. and Shore, B. W. "Coherent population transfer among quantum states of atoms and molecules." *Review of Modern Physics*, 70, 1003 (1998).

[130] Vitanov, N. V., Rangelov, A. A., Shore, B. W. and Bergmann, K. “Stimulated Raman adiabatic passage in physics, chemistry, and beyond.” *Review of Modern Physics*, 89, 015006 (2017).

[131] Boller, K.-J., Imamoğlu, A. and Harris, S. E. “Observation of electromagnetically induced transparency.” *Physical Review Letters*, 66, 2593 (1991).

[132] Hau, L. V., Harris, S. E., Dutton, Z. and Behroozi, C. H. “Light speed reduction to 17 metres per second in an ultracold atomic gas.” *Nature*, 397, 594 (1999).

[133] Peng, D., Özdemir, S. K., Chen, W., Nori, F. and Yang, L. “What is and what is not electromagnetically induced transparency in whispering-gallery microcavities.” *Nature Communications*, 5, 5082 (2014).

[134] Donarini, A., Niklas, M., Schafberger, M., Paradiso, N., Strunk, C. and Grifoni, M. “Coherent population trapping by dark state formation in a carbon nanotube quantum dot.” *Nature Communications*, 10 (2019).

[135] Ciamei, A., Bayerle, A., Chen, C., Pasquiou, B. and Schreck, F. “Efficient production of long-lived ultracold Sr_2 molecules.” *Physical Review A*, 96, 013406 (2017).

[136] Lu, B. and Wang, D. “Note: A four-pass acousto-optic modulator system for laser cooling of sodium atoms.” *Rev. Sci. Instr.*, 88, 076105 (2017).

[137] Winkler, K., Thalhammer, G., Theis, M., Ritsch, H., Grimm, R. and Hecker Denschlag, J. “Atom-Molecule Dark States in a Bose-Einstein Condensate.” *Physical Review Letters*, 95, 063202 (2005).

[138] Kuklinski, J. R., Gaubatz, U., Hioe, F. T. and Bergmann, K. “Adiabatic population transfer in a three-level system driven by delayed laser pulses.” *Physical Review A*, 40, 6741 (1989).

[139] Danzl, J. G., Mark, M. J., Haller, E., Gustavsson, M., Bouloufa, N., Dulieu, O., Ritsch, H., Hart, R. and Nägerl, H.-C. “Precision molecular spectroscopy for ground state transfer of molecular quantum gases.” *Faraday Discuss.*, 142, 283 (2009).

[140] Cohen-Tannoudji, C. and Reynaud, S. “Simultaneous saturation of two atomic transitions sharing a common level.” *Journal of Physics B: Atomic and Molecular Physics*, 10, 12, 2311 (1977).

[141] Abi-Salloum, T. Y. “Electromagnetically induced transparency and Autler-Townes splitting: Two similar but distinct phenomena in two categories of three-level atomic systems.” *Physical Review A*, 81, 053836 (2010).

[142] Lu, X., Miao, X., Bai, J., Pei, L., Wang, M., Gao, Y., Wu, L.-A., Fu, P., Wang, R. and Zuo, Z. "Transition from Autler–Townes splitting to electromagnetically induced transparency based on the dynamics of decaying dressed states." *Journal of Physics B: Atomic, Molecular and Optical Physics*, 48, 5, 055003 (2015).

[143] Meystre, P. and Sargent, M. Elements of Quantum Optics. Springer (2007).

[144] Li, M. "private communication." (2019). Temple University.

[145] Weiner, J., Bagnato, V. S., Zilio, S. and Julienne, P. S. "Experiments and theory in cold and ultracold collisions." *Review of Modern Physics*, 71, 1 (1999).

[146] Mott, N. F. The Theory of Atomic Collisions. Oxford Clarendon Press (1965).

[147] Chin, C., Grimm, R., Julienne, P. and Tiesinga, E. "Feshbach resonances in ultracold gases." *Review of Modern Physics*, 82, 1225 (2010).

[148] Tiesinga, E., Verhaar, B. J. and Stoof, H. T. C. "Threshold and resonance phenomena in ultracold ground-state collisions." *Physical Review A*, 47, 4114 (1993).

[149] Berninger, M., Zenesini, A., Huang, B., Harm, W., Nägerl, H.-C., Ferlaino, F., Grimm, R., Julienne, P. S. and Hutson, J. M. "Universality of the Three-Body Parameter for Efimov States in Ultracold Cesium." *Physical Review Letters*, 107, 120401 (2011).

[150] Gross, N., Shotan, Z., Kokkelmans, S. and Khaykovich, L. "Observation of Universality in Ultracold ^{7}Li Three-Body Recombination." *Physical Review Letters*, 103, 163202 (2009).

[151] Pollack, S. E., Dries, D. and Hulet, R. G. "Universality in Three- and Four-Body Bound States of Ultracold Atoms." *Science*, 326, 5960, 1683 (2009).

[152] Kraemer, T., Mark, M., Waldburger, P., Danzl, J. G., Chin, C., Engeser, B., Lange, A., Pilch, K., Jaakkola, A., Nägerl, H. and Grimm, R. "Evidence for Efimov quantum states in an ultracold gas of caesium atoms." *Nature (London)*, 440, 315 (2006).

[153] D'Incao, J. P. "Few-body physics in resonantly interacting ultracold quantum gases." *Journal of Physics B: Atomic, Molecular and Optical Physics*, 51, 043001 (2018).

[154] Naidon, P. and Endo, S. "Efimov physics: a review." *Reports on Progress in Physics*, 80, 056001 (2017).

[155] Cirac, J. and Zoller, P. "Goals and opportunities in quantum simulation." *Nature Physics*, 8, 264 (2012).

[156] Bloch, I., Dalibard, J. and Nascimbne, S. "Quantum simulations with ultracold quantum gases." *Nature Physics*, 8, 267 (2012).

[157] Chen, Q., Stajic, J., Tan, S. and Levin, K. "BCS-BEC crossover: From high temperature superconductors to ultracold fermi superfluids." *Physics Reports*, 412.

[158] Greiner, M., Mandel, O., Esslinger, T., T., H. and Bloch, I. "Quantum phase transition from a superfluid to a Mott insulator in a gas of ultracold atoms." *Nature*, 415, 39 (2002).

[159] Tanzi, L., Roccuzzo, S. M., Lucioni, E., Fama, F., Fioretti, A., Gabbanini, C., Modugno, G., Recati, A. and Stringari, S. "Supersolid symmetry breaking from compressional oscillations in a dipolar quantum gas." *Nature*, 573, 7773 (2019).

[160] Böttcher, F., Schmidt, J.-N., Wenzel, M., Hertkorn, J., Guo, M., Langen, T. and Pfau, T. "Transient Supersolid Properties in an Array of Dipolar Quantum Droplets." *Physical Review X*, 9, 011051 (2019).

[161] Chomaz, L., Petter, D., Ilzhöfer, P., Natale, G., Trautmann, A., Politi, C., Durastante, G., van Bijnen, R. M. W., Patscheider, A., Sohmen, M., Mark, M. J. and Ferlaino, F. "Long-Lived and Transient Supersolid Behaviors in Dipolar Quantum Gases." *Physical Review X*, 9, 021012 (2019).

[162] Murthy, P. A., Boettcher, I., Bayha, L., Holzmann, M., Kedar, D., Neidig, M., Ries, M. G., Wenz, A. N., Zürn, G. and Jochim, S. "Observation of the Berezinskii-Kosterlitz-Thouless Phase Transition in an Ultracold Fermi Gas." *Physical Review Letters*, 115, 010401 (2015).

[163] Fischer, U. R. and Schützhold, R. "Quantum simulation of cosmic inflation in two-component Bose-Einstein condensates." *Physical Review A*, 70, 063615 (2004).

[164] Eckel, S., Kumar, A., Jacobson, T., Spielman, I. B. and Campbell, G. K. "A Rapidly Expanding Bose-Einstein Condensate: An Expanding Universe in the Lab." *Physical Review X*, 8, 021021 (2018).

[165] Tewari, S., Scarola, V. W., Senthil, T. and Sarma, S. D. "Emergence of Artificial Photons in an Optical Lattice." *Physical Review Letters*, 97, 200401 (2006).

[166] Gandolfi, S., Gezerlis, A. and Carlson, J. “Neutron Matter from Low to High Density.” *Annual Review of Nuclear and Particle Science*, 65, 1, 303 (2015).

[167] Zwierlein, M. W., Abo-Shaeer, J. R., Schirotzek, A., Schunck, C. H. and Ketterle, W. “Vortices and superfluidity in a strongly interacting Fermi gas.” *Nature*, 435, 7045, 1047 (2005).

[168] Cornish, S. L., Claussen, N. R., Roberts, J. L., Cornell, E. A. and Wieman, C. E. “Stable ^{85}Rb Bose-Einstein Condensates with Widely Tunable Interactions.” *Physical Review Letters*, 85, 1795 (2000).

[169] Weber, T., Herbig, J., Mark, M., Nägerl, H.-C. and Grimm, R. “Three-Body Recombination at Large Scattering Lengths in an Ultracold Atomic Gas.” *Physical Review Letters*, 91, 123201 (2003).

[170] Courteille, P., Freeland, R. S., Heinzen, D. J., van Abeelen, F. A. and Verhaar, B. J. “Observation of a Feshbach Resonance in Cold Atom Scattering.” *Physical Review Letters*, 41, 1532 (1978).

[171] Inouye, S., Andrews, M. R., Stenger, J., Miesner, H.-J., Stamper-Kurn, D. M. and Ketterle, W. “Observation of Feshbach resonances in a Bose-Einstein condensate.” *Nature*, 392, 151 (1998).

[172] Moerdijk, A. J., Verhaar, B. J. and Axelsson, A. “Resonances in ultracold collisions of ^{6}Li, ^{7}Li, and ^{23}Na.” *Physical Review A*, 51, 4852 (1995).

[173] Fatemi, F. K., Jones, K. M. and Lett, P. D. “Observation of Optically Induced Feshbach Resonances in Collisions of Cold Atoms.” *Physical Review Letters*, 85, 4462 (2000).

[174] Theis, M., Thalhammer, G., Winkler, K., Hellwig, M., Ruff, G., Grimm, R. and Denschlag, J. H. “Tuning the Scattering Length with an Optically Induced Feshbach Resonance.” *Physical Review Letters*, 93, 123001 (2004).

[175] Reschovsky, B. “Studies of Ultracold Strontium Gases.” *PhD Thesis - University of Maryland* (2017).

[176] Dzuba, V. A., Flambaum, V. V. and Schiller, S. “Testing physics beyond the standard model through additional clock transitions in neutral ytterbium.” *Physical Review A*, 98, 022501 (2018).

[177] Zhang, R., Cheng, Y., Zhai, H. and Zhang, P. “Orbital Feshbach Resonance in Alkali-Earth Atoms.” *Physical Review Letters*, 115, 135301 (2015).

[178] Höfer, M., Riegger, L., Scazza, F., Hofrichter, C., Fernandes, D. R., Parish, M. M., Levinsen, J., Bloch, I. and Fölling, S. "Observation of an Orbital Interaction-Induced Feshbach Resonance in ^{173}Yb." *Physical Review Letters*, 115, 265302 (2015).

[179] Kato, S., Sugawa, S., Shibata, K., Yamamoto, R. and Takahashi, Y. "Control of Resonant Interaction between Electronic Ground and Excited States." *Physical Review Letters*, 110, 173201 (2013).

[180] González-Martínez, M. L. and Hutson, J. M. "Magnetically tunable Feshbach resonances in Li + Yb(^3P_J)." *Physical Review A*, 88, 020701 (2013).

[181] Petrov, A., Makrides, C. and Kotochigova, S. "Magnetic control of ultra-cold ^{6}Li and ^{174}Yb($^3P_2$) atom mixtures with Feshbach resonances." *New Journal of Physics*, 17, 045010 (2015).

[182] Dowd, W., Roy, R., Shrestha, R., Petrov, A., Makrides, C., Kotochigova, S. and Gupta, S. "Magnetic field dependent interactions in an ultracold Li-Yb($^3P_2$) mixture." *New Journal of Physics*, 17, 055007 (2015).

[183] Chen, T., Zhang, C., Li, X., Qian, J. and Wang, Y. "Anisotropy induced Feshbach resonances in mixtures of ^{6}Li(^{2}S)+^{171}Yb(^{3}P$_2$." *New Journal of Physics*, 17, 103036 (2015).

[184] Petrov, A., Tiesinga, E. and Kotochigova, S. "Anisotropy-Induced Feshbach Resonances in a Quantum Dipolar Gas of Highly Magnetic Atoms." *Physical Review Letters*, 109, 103002 (2012).

[185] Baumann, K., Burdick, N. Q., Lu, M. and Lev, B. L. "Observation of low-field Fano-Feshbach resonances in ultracold gases of dysprosium." *Physical Review A*, 89, 020701 (2014).

[186] Maier, T., Ferrier-Barbut, I., Kadau, H., Schmitt, M., Wenzel, M., Wink, C., Pfau, T., Jachymski, K. and Julienne, P. S. "Broad universal Feshbach resonances in the chaotic spectrum of dysprosium atoms." *Physical Review A*, 92, 060702 (2015).

[187] Maier, T., Kadau, H., Schmitt, M., Wenzel, M., Ferrier-Barbut, I., Pfau, T., Frisch, A., Baier, S., Aikawa, K., Chomaz, L. et al. "Emergence of Chaotic Scattering in Ultracold Er and Dy." *Physical Review X*, 5, 041029 (2015).

[188] Frisch, A., Mark, M., Aikawa, K., Ferlaino, F., Bohn, J. L., Makrides, C., Petrov, A. and Kotochigova, S. "Quantum chaos in ultracold collisions of gas-phase erbium atoms." *Nature*, 507, 475 (2014).

[189] Ravensbergen, C., Soave, E., Corre, V., Kreyer, M., Huang, B., Kirilov, E. and Grimm, R. "Strongly Interacting Fermi-Fermi Mixture of ^{161}Dy and ^{40}K." *arXiv:1909.03424 [cond-mat.quant-gas]* (2019).

[190] Yang, H., Zhang, D.-C., Liu, L., Liu, Y.-X., Nan, J., Zhao, B. and Pan, J.-W. "Observation of magnetically tunable Feshbach resonances in ultracold ^{23}Na^{40}K + ^{40}K collisions." *Science*, 363, 6424, 261 (2019).

[191] Brue, D. A. and Hutson, J. M. "Magnetically Tunable Feshbach Resonances in Ultracold Li-Yb Mixtures." *Physical Review Letters*, 108, 043201 (2012).

[192] Brue, D. A. and Hutson, J. M. "Prospects of forming ultracold molecules in $^2\Sigma$ states by magnetoassociation of alkali-metal atoms with Yb." *Physical Review A*, 87, 052709 (2013).

[193] Yang, B. C., Frye, M. D., Guttridge, A., Aldegunde, J., Żuchowski, P. S., Cornish, S. L. and Hutson, J. M. "Magnetic Feshbach resonances in ultracold collisions between Cs and Yb atoms." *Physical Review A*, 100, 022704 (2019).

[194] Sleator, T., Pfau, T., Balykin, V., Carnal, O. and Mlynek, J. "Experimental demonstration of the optical Stern-Gerlach effect." *Physical Review Letters*, 68, 1996 (1992).

[195] Taie, S., Takasu, Y., Sugawa, S., Yamazaki, R., Tsujimoto, T., Murakami, R. and Takahashi, Y. "Realization of a SU(2) × SU(6) System of Fermions in a Cold Atomic Gas." *Physical Review Letters*, 105, 190401 (2010).

[196] Stellmer, S., Grimm, R. and Schreck, F. "Detection and manipulation of nuclear spin states in fermionic strontium." *Physical Review A*, 84, 043611 (2011).

[197] Roberts, J. L., Claussen, N. R., Cornish, S. L. and Wieman, C. E. "Magnetic Field Dependence of Ultracold Inelastic Collisions near a Feshbach Resonance." *Physical Review Letters*, 85, 728 (2000).

[198] Chin, C., Vuletić, V., Kerman, A. J., Chu, S., Tiesinga, E., Leo, P. J. and Williams, C. J. "Precision Feshbach spectroscopy of ultracold Cs_2." *Physical Review A*, 70, 032701 (2004).

[199] Dowd, W. H. "Interactions in the Ultracold Lithium - Ytterbium 3P2 System." *PhD Thesis - University of Washington* (2014).

[200] Zhang, J., van Kempen, E. G. M., Bourdel, T., Khaykovich, L., Cubizolles, J., Chevy, F., Teichmann, M., Tarruell, L., Kokkelmans, S. J. J. M. F. and Salomon, C. "*P*-wave Feshbach resonances of ultracold ^{6}Li." *Physical Review A*, 70, 030702 (2004).

[201] Schunck, C. H., Zwierlein, M. W., Stan, C. A., Raupach, S. M. F., Ketterle, W., Simoni, A., Tiesinga, E., Williams, C. J. and Julienne, P. S. "Feshbach resonances in fermionic ^{6}Li." *Physical Review A*, 71, 045601 (2005).

[202] Green, A., Li, H., See Toh, J. H., Tang, X., McCormick, K., Li, M., Kotochigova, S. and Gupta, S. "Feshbach resonances in p-wave three-body recombination within Fermi-Fermi mixtures of open-shell ^{6}Li and closed-shell ^{173}Yb atoms." *arXiv:1912.04874[physics.atom-ph]* (2019).

[203] Mark, M., Meinert, F., Lauber, K. and Nägerl, H. "Mott-Insulator-Aided Detection of Ultra-Narrow Feshbach Resonances." *SciPost Phys.*, 5, 055 (2018).

[204] Heo, M.-S., Wang, T. T., Christensen, C. A., Rvachov, T. M., Cotta, D. A., Choi, J.-H., Lee, Y.-R. and Ketterle, W. "Formation of ultracold fermionic NaLi Feshbach molecules." *Phys. Rev. A*, 86, 021602 (2012).

[205] Merkel, B., Thirumalai, K., Tarlton, J. E., Schäfer, V. M., Ballance, C. J., Harty, T. P. and Lucas, D. M. "Magnetic field stabilization system for atomic physics experiments." *Review of Scientific Instruments*, 90, 4, 044702 (2019).

[206] Hansen, A. H., Khramov, A., Dowd, W. H., Jamison, A. O., Plotkin-Swing, B., Roy, R. J. and Gupta, S. "Production of quantum degenerate mixtures of ytterbium and lithium with controllable interspecies overlap." *Physical Review A*, 87, 013615 (2013).

Appendix A

ADDITIONAL EXPERIMENTAL DETAIL FOR CHAPTER 5

A.1 Trapping ^{173}Yb

Although our lab has created quantum degenerate samples of ^{173}Yb [206] in the past, at the time of our attempt to observe YbLi MFRs we had not used that ability for about five years. For this reason we will briefly summarize the changes made to the apparatus to create ultracold ^{173}Yb atoms.

Since the oven that supplies the atomic beam to our main vacuum chamber contains an un-enriched sample of Yb for which the abundance of ^{173}Yb is quite high, we did not have to load any additional Yb into the oven. The only change that needed be made to successfully capture ^{173}Yb atoms in the MOT was to shift the frequency of the slowing and MOT beams to address the electronic transitions in ^{173}Yb instead of ^{174}Yb. Additionally, the imaging beam frequency needed to be shifted to be resonant with ^{173}Yb. For the green laser system this was simple because the spectroscopy and MOT AOMs are arranged such that if we lock the laser using the error signal derived from a particular isotope's signal in our saturated absorption spectroscopy setup, the MOT light will be near the proper detuning.

Locking the "blue" laser properly is somewhat more complicated because we utilize the spectroscopy signal from a different isotope which is shifted by a convenient span of energy to achieve the large detuning from resonance required for the Zeeman slower beam. Specifically, when trapping ^{174}Yb we lock the laser to the error signal derived from the ^{176}Yb spectroscopy peak. The imaging and spectroscopy AOMs are then used to bring the imaging light into resonance with ^{174}Yb. A description of how this is done is shown in Table A.1. When switching to ^{173}Yb we decided to lock the laser to ^{174}Yb as this would require relatively small changes to the imaging and spectroscopy AOMs to achieve resonance with the ^{173}Yb

Frequency Name	Relation	Frequency for ^{174}Yb [MHz]	Frequency for ^{173}Yb [MHz]
$f_{lockpoint}$	$f_{laser} + F_{SPECTR.}$	f_{176}	f_{174}
$f_{imaging}$	$f_{laser} + 4F_{IMAGING}$	$f_{176} + 525 \approx f_{174}$	$f_{174} + 583 \approx f_{173}$
f_{slower}	$f_{laser} + F_{SLOWER}$	$f_{174} - 957$	$f_{173} - 977$
$F_{SPECTR.}$	+2 order from f_{laser}	347	289
$F_{IMAGING}$	+4 order from f_{laser}	218	223
F_{SLOWER}	+1 order from f_{laser}	85	85

Table A.1: This table describes the frequency of the relevant blue laser beams used in the experiment, as well as the frequencies of the AOMs used. All values are referenced relative to the $^1S_0\,(F = 5/2) \rightarrow {}^1P_1\,(F' = 7/2)$ transition for ^{x}Yb, called f_x, and numerical frequencies are given in MHz. Uppercase letters are used to express RF frequencies and lower case letters express optical frequencies. The order used accounts for a double pass configuration, if used. Note that small discrepancies between the chosen AOM frequency and the expected isotope shifts can be accounted for by noting that we do not always lock to the exact center of the error signal. Also note that we have considered f_{laser} to be the light in the +1 order of the slower AOM, thus treating the slower beam as the +1 order of that.

transition for imaging and maintain a similar detuning from the ^{173}Yb resonance for the Zeeman slower. The relevant isotope shifts for this consideration are printed in Table A.2.

A.2 OSG Beam Alignment and Vertical Imaging Setup

After frustrating attempts to utilize the Yb Zeeman slower's magnetic field to provide the necessary quantization field for the OSG beam polarization, we chose to steer the OSG beam onto the atomic cloud along the vertical direction. With the beam aligned vertically, the quantization field could be provided by our principal Helmholtz coils, allowing us to ramp these coils up to higher fields after preparing the Yb spin without worrying about

Isotope	Isotope Shift [MHz]
^{176}Yb	-509.31
^{173}Yb ($F' = 7/2$)	+587.99

Table A.2: The isotope shift relative to ^{174}Yb. The targeted hyperfine level must be specified for ^{173}Yb due to its nonzero nuclear spin. Data from [89].

passing through a magnetic field zero. To get the OSG beam nearly aligned to the atoms, we "recycled" the vertical arm of our D1 gray molasses cooling setup, which had been previously used to perform sub-Doppler cooling on Li atoms after the MOT stage. The schematic of the optical layout for this is shown in Figure A.1(a). A PM fiber is used to launch the OSG beam onto the main optics table where it first passes through a 1:10 expanding circular telescope. An additional cylindrical telescope is used to make the resulting beam elliptical. The purpose of this is to prevent the cloud from sampling a large gradient of the optical potential in both directions as this can result in a final cloud configuration more like a "fan" shape or as we dubbed it a "wi-fi symbol" than an array of mostly circular clouds. The expanded beam is combined with the MOT beams via a polarizing beam cube, necessarily obtaining the opposite circular polarization as the MOT. The OSG beam follows the MOT path through two waveplates used to create the proper polarization for the MOT and is finally reflected upward into the chamber by a 45 degree mirror (see Figure A.1).

The spatial extent of our Yb cloud in the ODT being about 20 μm, and the OSG beam have a waist of about 100 μm (in the direction of interest) put demanding constraints on the relative positioning of the two. It would have required unlimited patience and some good luck to place the OSG beam at the right position relative to the cloud without determining their respective locations in a common imaging system. For this reason we set up an alternative imaging path for which the imaging beam came up from the bottom. The elements of this imaging system are drawn in Figure A.1(b). The imaging beam is launched onto the main table via a PM fiber and expanded with a spherical telescope. The beam is then combined with the vertical MOT beams using a long-wave-pass dichroic mirror. After passing through the chamber the light is collected by the “top-down imaging” lens, an f=100 mm lens (Thorlabs AC508-100-A) that was purchased with a 2” diameter but subsequently cut to about 1.4” in one dimension so as to be placed just above the vacuum chamber’s top-facing viewport while clearing the obstruction of the Helmholtz coil clamping system. The imaging beam exits the MOT path by way of a flipper mirror which is out of the way during the imaging step. A mirror on the vertical breadboard steers the imaging beam onto the secondary imaging breadboard where it is focused onto the camera either with magnification 3 or 8.

A.3 Alternative Pumping Scheme: “Blue Pumping”

Before implementing “green” optical pumping as described in Section 5.7.3, we originally set up an experimentally simpler but more limited scheme which addressed the ${}^1S_0 \rightarrow {}^1P_1$ transition at 399 nm, therefore called “blue” pumping in accordance with the lab tradition of calling the 399 nm light ‘blue.’ This scheme was capable of pumping the Yb sample into either the $m_F = -5/2$ or $m_F = +5/2$ states depending on the polarization used to address the transition, as show in Figure A.2.

This method was simple to implement. We roughly overlapped the optical pumping (OP) beam with the Yb slower beam using a polarizing beam cube and used small adjustments to to overlap the OP beam with the atoms trapped in the ODT. This method of combination meant that the OP beam and the slower beam would necessarily have opposite polarizations, and we were unable to easily change the polarization of the OP beam using a waveplate. Instead if we needed to pump into the other spin state we reversed the direction of the quantization axis by changing the field applied parallel to the beams. Specifically, we turned off the magnetic field provided by the Zeeman slower coils themselves and turned on the field used to cancel the Zeeman slower field at the center of the vacuum chamber (the Yb slower compensation coils).

We derived the blue OP beam from the slower beam. We inserted the AOM used for

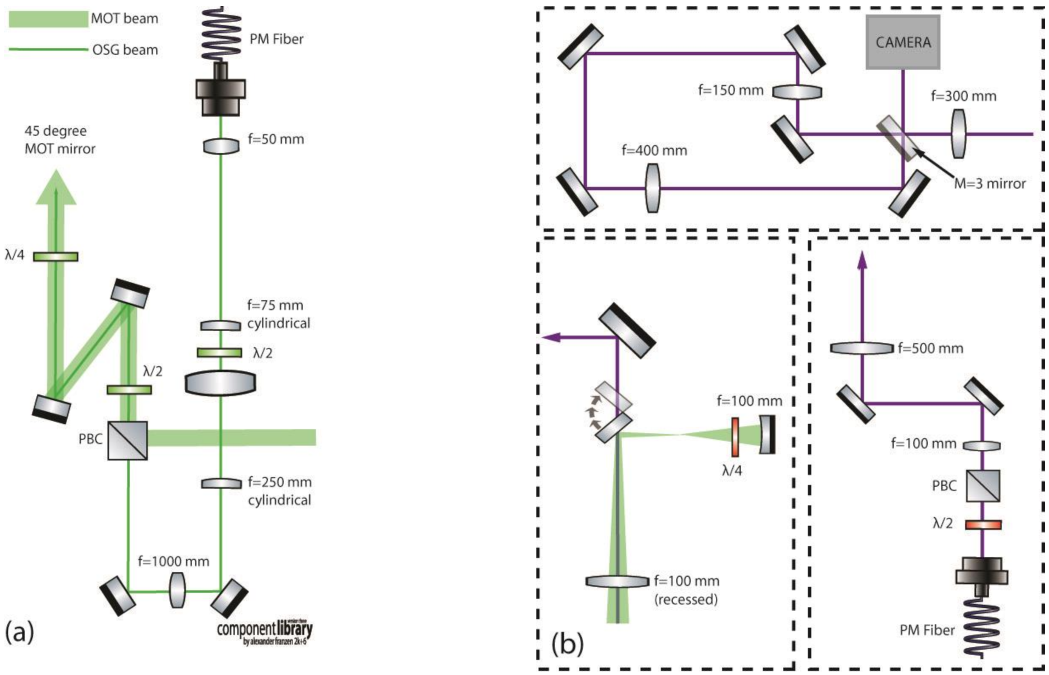

Figure A.1: A schematic representation of the optical paths added to the existing apparatus in order to perform OSG. (a) shows the combination of the OSG beam with the MOT beam, as seen looking down onto the optics table and (b) shows the three principal parts of the vertical imaging system: lower right - imaging beam launch into chamber (top-down view). Lower left - imaging beam after passing through chamber (side view). Upper - focusing and magnification optics (top-down view).

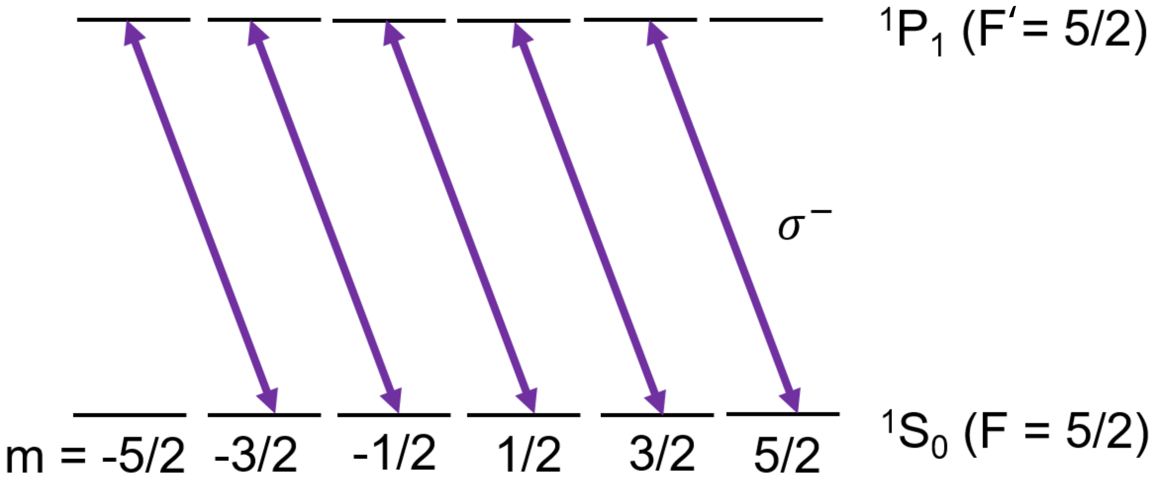

Figure A.2: A schematic of "blue pumping" with σ^- light. This would pump the population into $m_F = -5/2$.

the blue OP beam into the slower beam such that the zeroth order from this AOM still constituted the slower beam. The +1 order was picked off to form the optical pumping beam. This beam was coupled into a single mode fiber for subsequent combination with the slower beam further downstream. The blue OP AOM is centered at 80 MHz. In order for the blue OP beam to be dark to states $\pm 5/2$, it must be tuned to the $^1S_0\,(F = 5/2) \rightarrow {}^1P_1\,(F' = 5/2)$ transition. To state this more practically, we needed the blue OP beam to be 843.7 MHz lower in frequency than our blue imaging beam which is resonant with $^1S_0\,(F = 5/2) \rightarrow {}^1P_1\,(F' = 7/2)$ [89]. Table A.3 shows the changes that were made to the various blue laser beam AOMs to achieve the proper frequency in the OP beam.

Despite the ease of implementation, we found that the blue pumping was somewhat unreliable. Because the OP beam passed through a polarizing cube before it reached the atoms, polarization noise made it difficult to control the amount of intensity seen by the atoms. Since this technique was also limited in its capabilities and green pumping was easier than we thought to execute, the method of blue pumping has mostly been retired.

Frequency Name	Relation	Frequency Before Change [MHz]	After Change [MHz]
$f_{imaging}$	f_0		
f_{laser}	$f_0 - 4F_{IMAGING}$	$f_0 - 880$	$f_0 - 1000$
f_{slower}	$f_{laser} + F_{SLOWER}$	$f_0 - 795$	$f_0 - 915$
f_{OP}	$f_{slower} + F_{OP}$	N/A	$f_0 - 840$
$F_{SPECTR.}$	+2 order from f_{laser}	290	403
$F_{IMAGING}$	+4 order from f_{laser}	220	250
F_{SLOWER}	+1 order from f_{laser}	85	85
F_{OP}	+1 from f_{slower}	N/A	75

Table A.3: This table describes the frequency of the relevant blue laser beams used in the experiment, as well as the frequencies of the AOMs used. All values are referenced relative to the ${}^1S_0\,(F = {}^5\!/_2) \rightarrow {}^1P_1\,(F' = {}^7\!/_2)$ transition, called f_0, and numerical frequencies are given in MHz. Uppercase letters are used to express RF frequencies and lower case letters express optical frequencies. The order used accounts for a double pass configuration, if used. The frequencies before the addition of the optical pumping AOM are included to serve as a cross check.

A.4 Magnetic Field Control Electronics

Our bias (or "Feshbach") magnetic field used for the MFR studies in this chapter were created by running a current through a pair of water-cooled copper coils in Helmholtz configuration (see [97] for details). The power supply was a TDK Lambda Genysys 30-300. We used the optional isolated analog control module installed at the rear of the power supply to change the current supplied to the coils.

Prior to embarking on the MFR study, we had used a single analog output of our Cicero/Atticus-based control system to program the power supply's control module. However, the 2 mV precision of the Cicero analog outputs limited our magnetic field resolution to ≈ 800 mG, which would not be sufficient to observe MFRs which we were anticipating would appear to be about 100 mG wide from thermal broadening as seen in [83]. The simple solution to this problem was to dedicate two analog channels to controlling the current: a coarse voltage and a fine voltage. We decided for simplicity that the fine voltage would equal the Cicero ouptut voltage divided by 100, giving a precision of ≈ 8 mG. In the end, this was smaller than the 20 mG precision on our reading of the Hall probe used to measure the current and thus determine the field so the control of the field was not a limitation for the experiments.

We built a circuit that would divide one input named "Fesh fine" by 100 and add it to a second input named "Fesh coarse." This circuit is shown in Figure A.3. The circuit is colloquially referred to as the "addvider." The resulting circuit produced the following output voltage

$$V_{out} = 0.98279 * V_1 + 0.000963 * V_2$$

.

As expected, this was not the same as the ideal $V_{out} = V_1 + 100 * V_2$ but we were able to program Cicero to invert the equation to produce suitable values of V_1 and V_2 for a given target V_{out}. In fact, we programmed Cicero to invert this equation after applying the calibration to the magnetic field so that we need only put in as a variable the desired

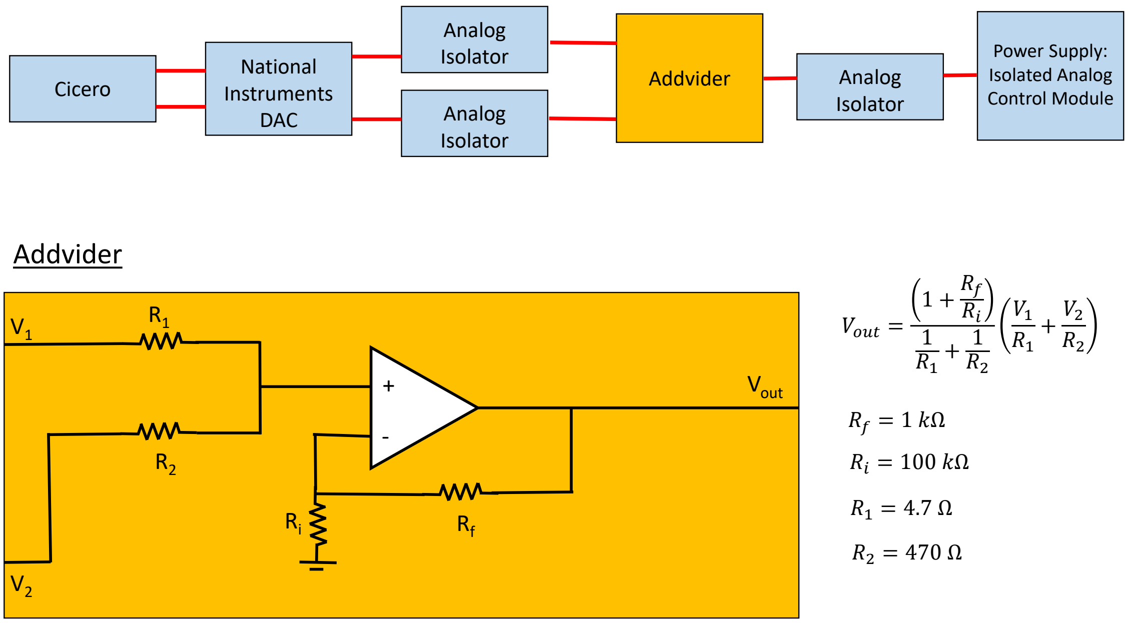

Figure A.3: A schematic of the control electronics used for the bias "Feshbach" coils. The "addvider circuit" is needed to increase the precision of our control scheme and was built in the lab and is housed in a NIM box.

magnetic field and Cicero would generate the proper values of V_1 (Fesh coarse) and V_2 (Fesh fine). This worked fairly well for everyday use but was limited by residual effects of the 8 mG precision which caused alternating under or over shoots of the targeted field. However, these errors occurred at known values of the field and could thus be avoided. In practice, we did not rely on the values programmed into Cicero as a true measure of the magnetic field but rather always recorded the reading on the Hall probe (F.W. Bell CLN-300) for each field of interest. We used a digital multimeter (BK precision 2831E) to measure the output of the Hall probe. With 4.5 digits of precision and a typical voltage of $\sim 1V$ at the highest, our measurement precision was 20 mG.